The Investigation and Analysis of Factors that Limit Penetration of Tubulars in Horizontal Oil Wells.

Ivor McCourt

A thesis submitted in partial fulfilment of the
Requirements of Napier University
for the degree of Doctor of Philosophy
June, 2003

Abstract

To carry out remedial work in the oil producing wells through the production tubing string, a method using a continuous length of steel tubing or coiled tubing is used, that allows quick access to the well. Coiled tubing can also be used for drilling and extending existing wells and shows significant cost savings over traditional joined drill pipe methods. As the coiled tubing is being pushed into a horizontal well it lies initially straight on the bottom part of the casing of the well. As penetration increases, the friction force arising from the contact of the tubing with the inner casing wall increases and the tubing buckles with low amplitude and long pitch length. As penetration increases further, the frictional force increases and buckling amplitude increases and the pitch length decreases. The tubing thus moves further up and round the inside of the casing. This process continues until the tubing reaches the top part of the casing and it moves from sinusoidal buckling into helical buckling. At this point the force required to push the tubing further rises dramatically, with subsequent locking of the tubing in the casing with no further penetration possible.

The work to date on this important industrial problem can be divided into two areas: (i) the theoretical approach backed by laboratory experiments in which the end of the containing tube is obstructed, so as to allow buckling to develop and (ii) full scale tests that meet with the practical problems but do not provide as much information and difficulties of scale can also extend the time required to complete satisfactory tests. The laboratory tests have demonstrated the buckling phenomenon but have not re-created the conditions existing in a well.

In this work a novel experimental apparatus is developed using tubular members of very low flexural rigidity and high value of friction between the tubular and a transparent containing cylinder. This allows limits on penetration of the tubulars to be observed in under 5 m of insertion. The experimental apparatus enables the simultaneous measurement of the insertion forces and the inserted length. A suitable control and data acquisition system has also been designed. Experimental results indicate clearly all important parameters which limit the penetration of the tubulars in horizontal containing cylinders.

A theoretical model of penetration has been developed, which is in excellent agreement with the experimental data. The model can be used to determine the importance of various design parameters on the maximum penetration of tubulars in horizontal wells. Finally, the model suggests how to maximise the penetration of coiled tubing in horizontal oil wells.

Declaration

I hereby declare that the work presented in this thesis was solely carried out by myself at Napier University, Edinburgh, except where due acknowledgement is made, and that it has not been submitted for any other degree.

Ivor McCourt (Candidate)

24/6/03

Date

Acknowledgements

This work would not have been possible without the continuing support and encouragement of my supervisors, Professor Jorge Kubie and Mr. Tom Truslove.

However this work would not have even started without the support of my wife Janet, to whom it is dedicated.

Table of Contents

List of Figures

Nomenclature

Only major symbols are defined in this section; minor symbols are defined in the text as appropriate.

A	Dimensionless constant	$\frac{M_T L}{EI}$
B	Dimensionless constant	$\frac{PL^2}{EI}$
C_1, C_2, C_3	Constants of integration	
D	Casing diameter	m
d	Tubing diameter	m
E	Modulus of elasticity	N/m^2
F_{CRN}	Insertion force for Nth buckled shape	N
μ	Friction coefficient	Dimensionless
g	Gravitational constant	m/s^2
I	Second moment of area	m^4
K	Dimensionless constant	$\frac{m_L g L^3}{EI}$
k^2	Buckling factor	$\frac{P}{EI}$
k_1	Constant end fixing factor	Dimensionless
L	Length of tubing	m
L_{BN}	Length of Nth buckled shape	m
L_{CR}	Transition length to helical buckling	m
L_N	Length of Nth buckled shape	m
L_{TOT}	Total length of buckled shapes	m
L_1, L_2	Length of buckled elements of tubing	m
ΔL_H	Change in length of tubular (helical buckling)	m
M	Bending moment	Nm
m	Mass	kg
m_L	Mass per unit length	kg/m

N	Number of buckled shape	Dimensionless
P	Axial force	N
P_{crh}	Critical helical buckling force	N
P_{crs}	Critical sinusoidal buckling force	N
P_{HEL}	Force along helix	N
P_{LAT}	Force at right angles to applied force	N
P_N	Total force (N buckled shapes) with reaction	N
P_{NORMAL}	Force normal to inner surface of tube	N
P_{NSIN}	Total force (N buckled shapes) with friction only	N
P_S	Force during sinusoidal buckling	N
P_y	Force at y	N
p	Pitch	m
R	Reaction force	N
r	Tubing to casing radial clearance	m
t	Tube wall thickness	m
α	Angle of helix	Radians
w	Weight of tubular per unit length	N/m
ρ	Density	kg/m^3

1. Introduction

1.1 Overview of Oil Deposits, Oil Well Drilling and Oil Production

Accumulations of oil and gas are found deep underground, typical depths for producing oil wells range from one thousand to four thousand metres. Locating oil and gas deposits involves the use of various seismic and geophysical methods followed by sophisticated computer analysis of the data to produce an accurate three-dimensional map detailing the extent and position of the reservoir. It is important to understand that the oil or gas in any oil field is in general not located in one large underground void. Oil and gas deposits are found distributed through porous rock formations and can vary dramatically in size, shape and vertical extent. The deposits in a particular field may come from a number of individual geological formations of different age and thickness and be separated from each other by considerable vertical distance, or from smaller pockets separated by large horizontal distances from the larger accumulations. A variety of geological formations in which oil deposits can be found are shown in figure 1.1.1.

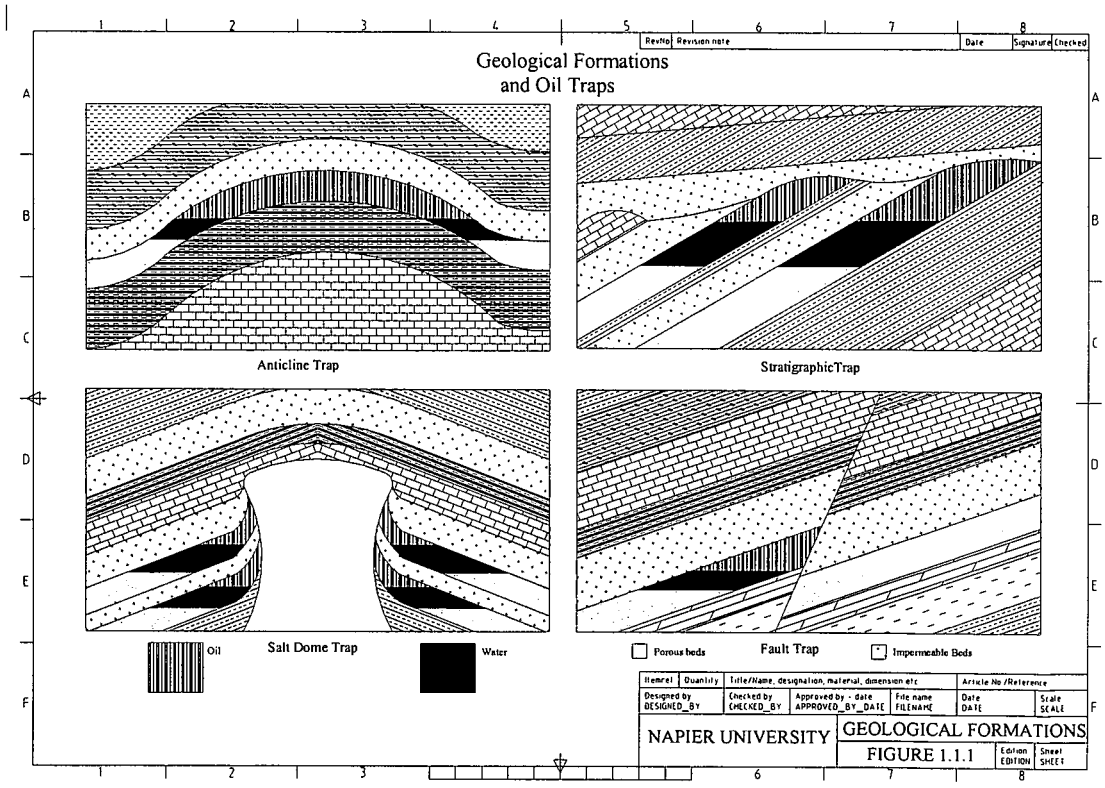

Figure 1.1.1 Geological formations showing oil traps.

To access these deposits involves drilling through the overlying strata using a tubular drill pipe with a drill bit or drill motor mounted on the lower end of the pipe. Most current wells are drilled using a non-rotating drill pipe, with the drill motor and drill bit mounted on the bottom end of the drill pipe. In the past rotating drill pipes were used with the drill bit attached to the bottom end of the drill pipe. However, non-rotating drill pipes with bottom mounted drill motors and bits make for easier steering of the drill, to ensure that the oil well reaches the target area in the particular reservoir, and to best drain the reserves that have been located by use of the methods described above.

The well is drilled in stages, using a number of different diameters, stepping down in diameter as the depth of the well increases. The diameter of the first casing from the surface to approximately one hundred metres depth is approximately seven hundred and fifty millimeters and the diameter of the casing that extends from the surface to the maximum depth of the well is approximately two hundred millimeters. At each stage of drilling the hole that is produced is lined with a steel well casing, that is fixed permanently in place by pumping cement into the annular space between the casing and the borehole. Oil well showing well casing and drill string is shown in figure 1.1.2.

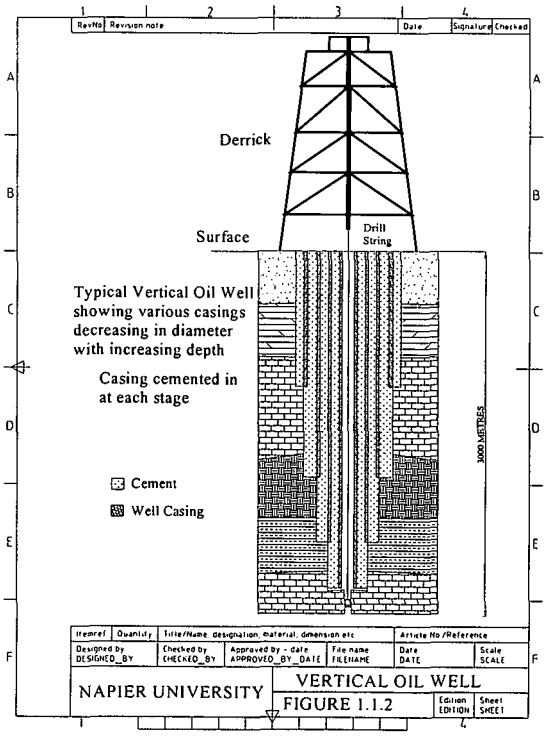

Figure 1.1.2 Vertical oil well showing different casing diameters.

After the casing has been installed in the well to its maximum depth/reach, packers are set which isolate the particular section or producing horizon where the oil or gas is located. The casing is perforated between these packers and production tubing is installed from the surface to pass through the top packer. This arrangement allows the well products to be conveyed from the producing formation through the perforations in the well casing to the surface via the production tubing string. It is possible to have several different production formations connected via separate production strings within the same well, figure 1.1.3 shows a typical arrangement.

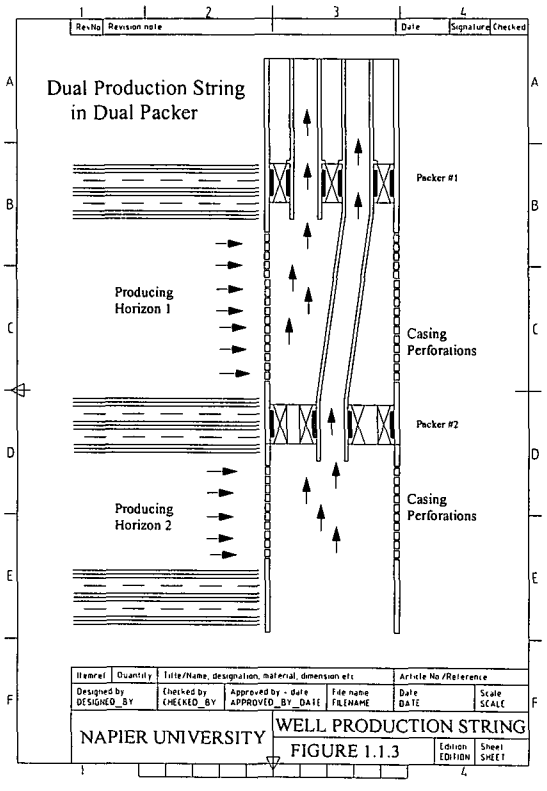

Figure 1.1.3 Well production strings from two different producing zones.

In addition to conveying the well products to the surface the production string can allow access to the producing well formation, if required, to carry out any work needed throughout the life of the well. All of the above tubulars including drill pipe, well casing, and production tubing are made up from sections of pipe ten to twenty metres in length that are screwed together as they are lowered into the well. This is a time consuming and costly operation.

To carry out remedial work in the well through the production tubing string, a method using a

continuous length of steel tubing or coiled tubing is used, that allows quick access to the well. Coiled tubing can also be used for drilling and extending existing wells and shows significant cost savings over traditional joined drill pipe methods. A typical diameter for the well at the producing depth is 200 mm, and a typical diameter for the production tubular is 100 mm. Taking account of the depth range for oil wells given above, length to diameter (L/d) ratios for drill pipe, well casing, production tubing and coiled tubing are very high and can be described as slender columns. Using the sizes given above the length/diameter ratios range from 10,000:1 to 40,000:1. In all of the above applications the tubulars are continuously, concentrically constrained along their length by being inside another tube or bore, this configuration ensures that tubulars buckle in a unique way.

As the tubulars have very high length/diameter ratios, first mode buckling cycle takes place at very low axial load. In a normal structural context, first mode buckling would be considered a failure and in virtually all cases where buckling of a column which is part of a structure occurs, the failure would be catastrophic. However because of the continuous concentric constraint, the tubulars buckle into a progressively higher number of cycles dependant on the axial load applied. The deflection of the tubular is initially a sinusoidal shape and eventually changes into a helical shape with increasing load. This phenomenon of continued controlled buckling after initial buckling has occurred is referred to as post-buckling behaviour (PBB). The loads seen in normal service must be controlled to ensure that the tubulars do not buckle to such an extent as to over-stress them. Understanding post-buckling behavior of tubulars is crucial to the oil exploration and production industry. This knowledge allows safe procedures to be developed for installation and use of tubulars in the field. As a consequence, this ensures that no potentially dangerous installations could be made, or damage to the tubulars will occur throughout the full range of loadings a well may see during its complete lifetime.

1.2 Vertical Oil Wells

In the case of vertical wells, installation of the casing or production tubing is relatively simple as gravity ensures that the tubular being lowered into the well hangs vertically down the well with little or no contact with the casing. This minimal contact ensures that very little friction force is generated that could oppose the motion of the tubular down the well. As a result the

tubular will easily reach the bottom of the well, and can locate in the packer as shown in figure 1.2.1.

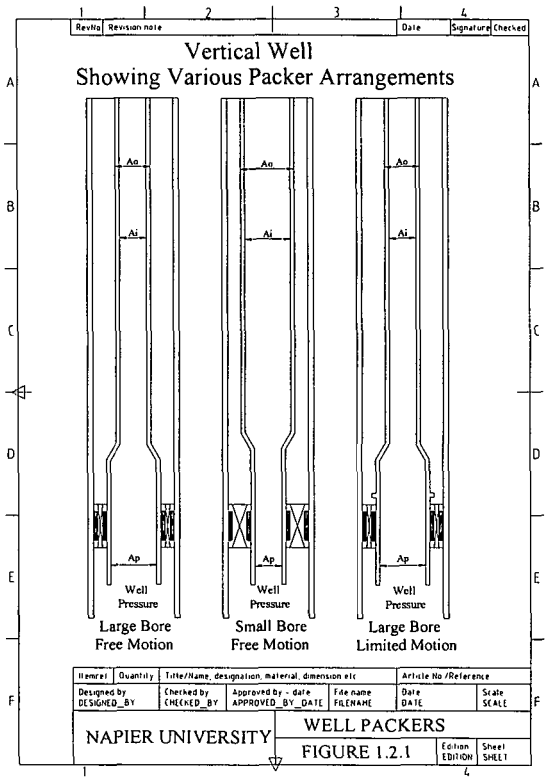

Figure 1.2.1 Well packers with various end restraints.

After installation, changes in temperature and/or pressure can, depending on the physical end restraint of the tubing string, lead to change in length and/or induce forces that could cause buckling and yielding of the tube. Any phenomenon which can cause severe loading of any tubulars in a producing oil well, with potential for failure of the same has to be understood to enable field operators to install tubulars safely, using procedures and rules developed from the understanding of this phenomenon.

1.3 Highly Inclined/Horizontal Oil Wells

Most wells drilled currently fall into this category, particularly those from fixed offshore platforms where the position for the platform is chosen to ensure that the largest possible amount of oil and gas can be drained from the different accumulations of oil and gas that

make up the oil field around the platform. Highly inclined/horizontal wells can reach out in a radius of several kilometres around an offshore platform. Horizontal sections in wells are also used to increase the area of the producing formation to the production tubing to increase flow rate, and are also used where the formation that contains the oil has high resistance to the flow of oil into the production tubing, again the area available for production is increased. A typical horizontal well is shown in figure 1.3.1.

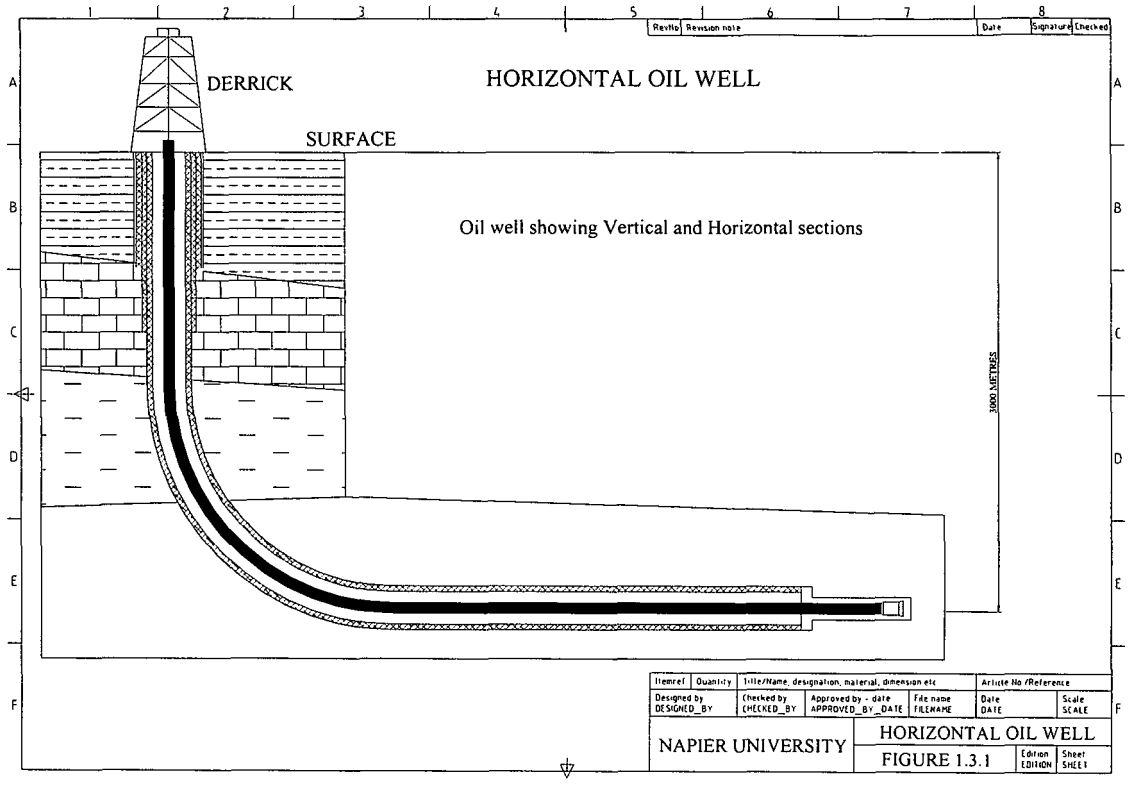

Figure 1.3.1 Horizontal oil well cross section.

In the case of highly inclined and more so in horizontal wells, gravity ensures that significant contact with the casing takes place and, as a result, substantial friction forces are generated which resist the motion of the tubular as is moves into the well.

The case that is being investigated in this work is that of horizontal wells. What actually happens in horizontal wells as the tubing is being pushed in, is that the tubular initially, is straight and lies in the bottom part of the casing. As penetration increases, the friction force arising from the contact of the tubing with the inner casing wall increases and the tubing buckles with low amplitude and long pitch length. As the *L/d* ratio is very high the force to

initiate the first buckling mode is very low. As penetration increases further, the frictional force increases, the buckling amplitude increases and pitch length decreases. That is, the tubing moves further up and round the inside of the casing. This process continues until the tubing reaches the top part of the casing and it moves from sinusoidal buckling into helical buckling. At this point the force required to push the tubing further rises dramatically, with subsequent locking of the tubing in the casing and no further penetration is possible. At the free end of the tubing the pitch is at a maximum and reduces progressively towards the insertion end as shown in figure 1.3.2.

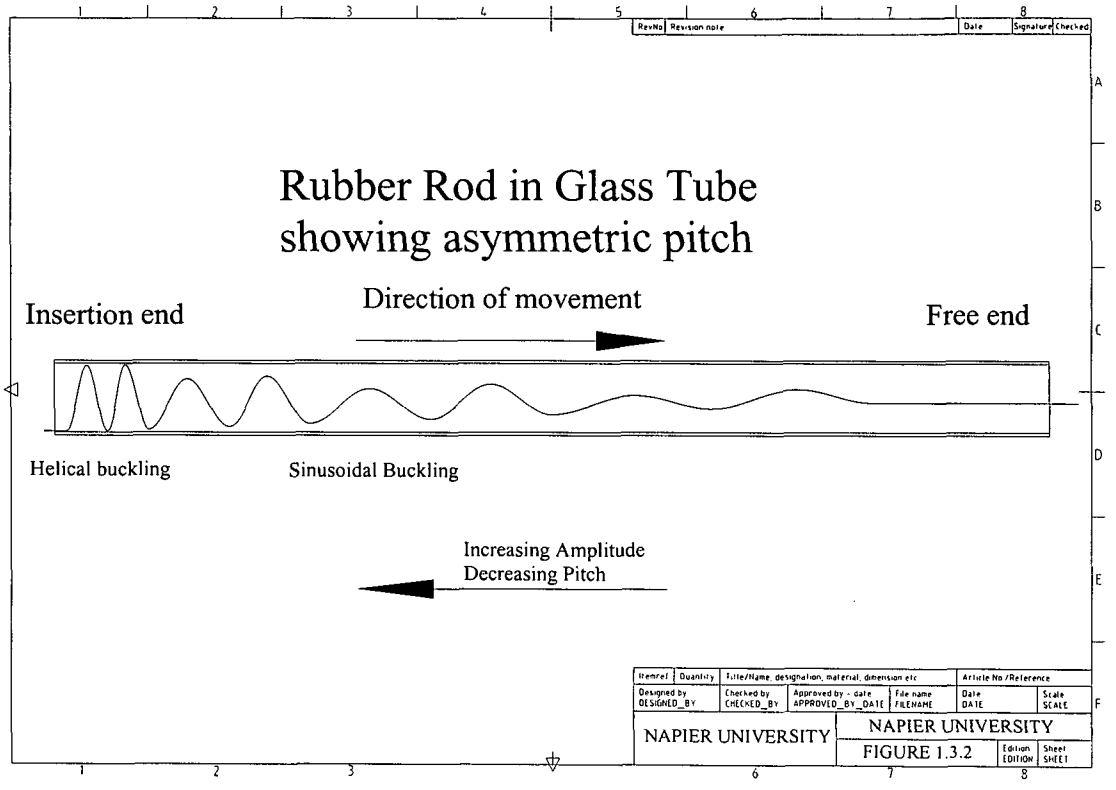

Figure 1.3.2 Buckling of constrained rod showing varying pitch.

Previous work has not simulated what happens in real wells, that is with the tube moving along the well inducing the forces to cause buckling. All of the studies with the exception of one full size system, but not full length, have used rods locked in tubes to simulate buckling.

In this study by careful choice of materials a test rig was built which modeled accurately over a range of casing and tubing diameter ratios (*D/d*), what happened in a real well, with helical buckling occurring within five metres.

2. Review of Published Literature

2.1 Overview of Relevant Factors

2.1.1 Introduction

The research work in this field has been driven by practical problems that the industry has encountered as the search and exploration for oil and gas has evolved. In the early stages of oilfield practice and until fairly recently, the simple procedure was to position the drill rig over the oil deposit and drill the well vertically into the reservoir (Rabia, 1985). As a consequence of this practice the problem of buckling in vertical tubing strings was the first to be addressed.

However with offshore platforms this simple approach is no longer possible and it became necessary to access oil and gas deposits which were not directly beneath the platform to enable the development of these resources to be economic (Rabia, 1985). This resulted in highly inclined and horizontal wells becoming normal practice in virtually all oil fields today. The unique problems that were encountered were addressed and are still being addressed as they occur through the papers of the Society of Petroleum Engineers. The published work reflects the development of the industry from vertical to horizontal wells.

The published work is primarily analytic in nature. Most of this work neglects the weight of the tubular and also neglects friction effects between the tubular and the constraining casing (Lubinski *et al*, 1962) and (Cheatham & Pattillo, 1984). A smaller body of work is based on experimental data, in all cases the effects of friction are minimised by lubricating the inner surface of the constraining cylinder.

Full scale modelling of oil wells would be prohibitively expensive and only one study which involved an horizontal section of casing on the surface, six hundred metres long with coiled tubing inside has been reported (Tailby *et al*, 1993).

To date the scale model experimental studies relating to inclined and horizontal wells have not reproduced the actual conditions occurring in the wells. This has been due in large part by

the use of metallic materials and locking the inner tubular against the ends of the transparent constraining casing (Hishada *et al*, 1996). In these scale studies the constraining casing was lubricated to minimise/eliminate friction effects. Loading of the inner rod causes it to buckle sinusoidally, which is followed by helical buckling as the load is increased (He & Killingstad, 1993). This reflects to some extent what happens in real wells but it is not completely accurate, particularly in horizontal wells (Chen *et al* 1990).

In horizontal wells inner tubular weight and friction are parameters, which have a major influence on the way in which the tubular buckles (Chen *et al* 1990).

2.1.2 Overview of buckling

The focus of this work is to investigate and analyse the behaviour of coiled tubing in horizontal well sections, however it is important to give a broad overview of the use of tubulars used in vertical, inclined and horizontal wells.

All the investigation work carried out in the preparation of this document has been with rods and tubes with round cross sections. The behaviour of columns or struts when loaded axially depends on the length to diameter (*L/d*) ratio. Columns with low *L/d* ratios fail when the stress in the column generated by the axial load reaches the yield point for the material. Long slender columns or those with high *L/d* ratios fail/buckle with an axial load, that is only a small fraction of that necessary to cause failure by yielding of a low *L/d* ratio column of equal cross-section. If a long slender column could be constructed which was perfectly symmetrical, the material properties identical across its section and the axial load applied through the centre of the cross section, this theoretical column should be able to support the same load as a short column of equal cross section (Den Hartog, 1977). This however is a hypothetical case as such a system would be highly unstable such that even an infinitesimally small disturbance would lead to buckling. However in practice sections are not symmetrical, material properties vary and the load is invariably not applied through the centre of the cross section. All of these imperfections have the combined effect that when a real column is loaded axially it bends/buckles laterally at a fairly low load. If a column with both ends fixed or with pinned connections buckles with an applied axial load (Gere & Timoshenko, 1961), the load at which

buckling occurs is referred to as the critical buckling load, P_{cr} and is defined by the equation 2.1.1.

$$P_{cr} = \frac{k_1 \pi^2 EI}{L^2} \tag{2.1.1}$$

where

k_1 is a constant which defines the end fixing conditions for the column.

E is the elastic modulus N/m^2

I is the second moment of area m^4

L is the length of the column m

In the design of structures, columns are always sized to ensure that the service loads are much smaller than the critical buckling load as buckling is normally considered as a failure mode.

2.1.3 Sinusoidal and helical buckling

In the case of oil wells the tubulars have very high length/diameter ratios and first buckling mode takes place at a very low axial load. In a normal structural context, this buckling would be considered a failure, however the tubing is continuously, concentrically constrained along its length by being inside the well casing or bore (Mitchell, 1986c). After the critical buckling load is reached and first mode buckling occurs, the deflection is limited by the radial clearance between the tubing and the casing (Cheatham & Pattillo, 1984). This continuous concentric constraint allows loads much greater than the critical buckling load to be applied and results in the tubing buckling into a progressively higher number of cycles as the axial load increases (Kwon, 1986).

The deflection of the tubing is initially into a sinusoidal shape and eventually changes into a helical shape with increasing load (Chen *et al*, 1990). The loads seen in normal service must be controlled to ensure that the tubulars do not buckle to such an extent as to overstress them, but this progressive buckling is not considered failure as in a structural sense (Mitchell, 1980). Tubulars in oil wells are a special case of buckling due to the continuous, concentric constraint.. Understanding the behaviour of tubulars which are continuously, concentrically,

constrained in vertical, inclined and horizontal sections of wells is crucial to the oil exploration and production industry to enable good safe practices to be developed for any well configuration encountered.

2.1.4 Buckling in vertical wells

In the case of vertical wells the tubing hangs vertically down the well with little or no contact with the casing (Lubinski *et al*, 1962), installation changes in temperature and/or pressure can, depending on the physical end restraint of the tubing string lead to change in length and/or induce forces that could cause buckling and yielding of the tube (Lubinski *et al,* 1962).

2.1.5 Buckling in inclined & horizontal wells

In the case of highly inclined and more so in horizontal wells, as installation of tubulars proceeds, gravity ensures that significant contact with the casing takes place (Hishada *et al*, 1996). As a result, substantial frictions forces are generated which resist the motion of the tubular as is moves into the well. In the horizontal section as the tubing is being pushed, the tubular is initially straight and lies in the bottom part of the casing. As penetration increases, the friction force arising from the contact of the tubing with the inner casing wall increases and the tubing buckles with low amplitude and long pitch length (Chen *et al*, 1990). As penetration increases further, the frictional force increases, buckling amplitude increases and pitch length decreases. i.e. the tubing moves further up and round the inside of the casing (He & Killingstad, 1993). This process continues until the tubing reaches the top part of the casing and it moves from sinusoidal buckling into helical buckling. At this point the force required to push the tubing further rises dramatically, with subsequent lock up and no further penetration is possible (Bhalla, 1996). At the free end of the tubing the pitch is at a maximum and reduces progressively towards the insertion end.

2.1.6 Limitations on penetration

With the onset of helical buckling the force required to push the tubing further into the well increases dramatically. In practical terms helical buckling limits the penetration into any oil well (Chen, *et al*, 1990).

2.2 Theoretical Review

The early papers on the subject concentrated on determining a value for the critical load for helical buckling. The earliest report on this problem appears in Love, (1927), where the value for the load is, when transposed to later terminology, equivalent to:

$$P_{crh}=\frac{4\pi^2 EI}{p^2} \tag{2.2.1}$$

Lubinski *et al*, (1962) carried out notable work; it appears as a standard text, which is referenced by many subsequent authors who have looked at the buckling phenomenon in oil wells. Lubinski *et al*, (1962) examined the problems associated with production tubing in a vertical well, with the tubing sealed in a packer at the producing horizon. Changes in temperature and pressure inside and outside the tubular combined with the type of restraint applied by the packer could cause significant changes in the length of the tubular and/or generate loads that could overstress and yield the tubular. The main reason for undertaking this study was at the request of field personnel looking for guidance when installing production tubing as changes in length produced by buckling were critical as incorrect allowances in initial length or tension in the tubing could result in the tubing coming out of the packer or overstressing the tubing. This work resulted in the following formulae for the critical buckling force for helical buckling P_{crh}.

$$P_{crh}=\frac{8\pi^2 EI}{p^2} \tag{2.2.2}$$

which gives the relationship between critical axial force and pitch distance, where p is the pitch between cycles.

The value for the critical load in helical buckling is examined in more detail by Cheatham & Pattillo, (1984), where the discrepancy between the two values is explored. They derive both values of the numerical constant using an energy balance approach and then a virtual work approach. Their conclusion is that the value 4 applies to the case when the helical buckling is unconstrained, but when the coiled tube is constrained to a fixed radius, the value obtained is 8. They also conclude that the 8 value would apply to insertion, but the 4 value would apply to extraction. In all these analyses, the tube is considered to be vertical, a slender rod and reacted by a stop at the foot of the casing to produce only helical buckling.

Mitchell, (1980) examined the buckling behaviour of a weightless rod in the vertical position using an equilibrium analysis. The analysis first considered plane buckling before moving to helical buckling. Because of the complexity of the equations, only a numerical solution was attempted. The packer was considered to be significant to the end moments and to the analysis. Mitchell, (1986b,c) extended his analysis to the case of an actual string where the weight of the string is included and also to the study of a tapered string. Conditions for the neutral point were developed.

Kwon, (1986) used the beam column equations to examine the problem of a vertical pipe with weight. Using a semi-analytical approach, such as a series solution approximation rather than a numerical solution, the variation in pitch with length of the string was deduced.

Mitchell, (1986a), introduced friction effects for two specific cases in a vertical column. The analysis started with the fourth order differential equation for the rod, but included contact forces. After making some approximations, solutions were obtained.

Dawson & Paslay, (1984) investigated the forces necessary to initiate buckling in an inclined casing and their results are summarized by the following equation.

$$P_{crs} = 2\sqrt{\frac{EIw\sin\theta}{r}} \qquad (2.2.3)$$

Chen *et al*, (1990), for the first time, addressed buckling of tubing and casing in frictionless, horizontal wells. They looked at the phenomenon of buckling initially being sinusoidal and

transitioning to helical buckling with increasing load. The value for the force to initiate sinusoidal buckling, was taken from Dawson & Pasley, (1984), as:

$$P_{crs} = 2\sqrt{\frac{EIw}{r}} \qquad (2.2.4)$$

while the helical initiation was expressed as :

$$P_{crh} = 2\sqrt{\frac{2EIw}{r}} \qquad (2.2.5)$$

which is related to the classical Lubinski equation. This paper presents experimental results, using an aluminium rod in a clear plastic tube lubricated by silicone oil, that confirm these figures, but does not extend the analysis to explain the increase of the force causing sinusoidal buckling to produce helical buckling.

He & Killingstad, (1993) specifically looked at problems associated with coiled tubing buckling in curved wells. They showed that well curvature substantially affects the force for helical buckling and as a consequence the maximum distance achieved in the well.

Hishida, *et al* (1996) used equations from earlier papers for sinusoidal and helical buckling. The rig used was able to view the buckling modes in a straight rod constrained inside an acrylic tube, one end of the rod pinned the other fixed, sliding. The forces required to produce the buckling were measured by a load cell system. Their analysis focused on the mode/force relationships, rather than force/pitch relationships. Although use of FEA is quoted to analyse the buckling, little detail is presented of the background theory and the procedure adopted. Friction forces were not considered in the analysis and the inside of the tube was fully lubricated to eliminate friction during the tests.

Qui, *et al.* (1998) examined buckling in a hole of constant curvature and the influence of prior deformations to the onset of helical buckling. Using the conservation of energy and virtual work approaches, they derive new equations for maximum axial forces to maintain stable sinusoidal configuration, taking into account the curvature of the hole and any prior curvature of the coiled tube.

2.3 Field Testing

A Joint Industry Research project to investigate Coiled Tubing Buckling in a horizontal well, Tallby *et al*, (1993), was carried out in Norway using full size components as used by oil industry contactors. The length of the casing, which was laid out on the surface, was six hundred metres. This work looked at the differences in applied force and transmitted force at the tool tip for a variety of cases. Residual bend of the tubing affects the force transmission and should be minimized. Tip loads are amplified by the tubing and will cause premature lock up, all causes should be minimised, in particular well profiles should have slow changes in orientation.

As always with full scale models of this size and complexity, it is very expensive to mount the investigation and the resulting data is restricted to the test set-up with no ability to explore alternative parameters such as casing and rod sizes.

2.4 Summary

The majority of the papers written have been concerned with the onset of helical buckling in vertical columns. From the classic equations, the work has developed to add more of the factors that would have to be considered in an oil well with the consequent increase in the complexity of the analysis. Only a few of the published papers deal with behaviour of tubulars in horizontal wells.

It can be concluded from the review of published literature, that no work has examined the development of self-induced sinusoidal buckling of a rod in a horizontal well with friction, such that the axial force will increase to initiate helical buckling. As the theoretical analysis of this is very complex, it may be beneficial to explore simplified models to be able to extract the maximum information from the analyses.

3 Aims of the Research

It is the aim of this study to investigate those factors which affect the penetration of tubulars into horizontal oil wells. Previous investigations have concentrated on the analysis of buckling, such as the nature of buckling, the buckled shape, the forces required and the parameters which affect buckling. As discussed above, the investigations have been generally carried out with the free end of the tubular member resting against an obstruction. Such an approach is unavoidable when modelling with standard materials, since the penetration lengths required to achieve locking with the free end unobstructed are considerable, and it is impractical to model them.

It is the primary purpose of this work to investigate this important problem when the free end of the tubular is unobstructed. Such an approach describes the actual conditions obtained in the field, and thus allows further insight to be gained. It is shown below that in order to decrease the lengths required to achieve full locking of the tubular the flexural rigidity of the tubular should be as low as possible and the friction between the tubular, and the well should be as high as possible. Several materials and shapes of the tubular have been investigated, and rubber formed into small diameter rods was finally chosen. In order to allow for visual observation of the behaviour of the rods, acrylic and glass cylinders were chosen to model the well. The locking can then be obtained with penetrations of under 5 m.

4. Experimental Apparatus

4.1 Overview

In this study the test apparatus was designed to reflect as accurately as possible what happens in a real well, with the test rig being not more than five metres in length. Hence, the main points addressed for the design of the test apparatus were: -

- Use of a rod material with a low elastic modulus required equipment for measuring the modulus.
- Use of a rod material with a high friction coefficient required equipment for measuring the friction coefficient in combination with the constraining cylinder.
- Transparent constraining cylinders used to allow viewing of buckling in real time.
- A feed mechanism to allow continuous accurate insertion and retraction of the rod at different feed rates.
- Handling arrangements for the rod to allow storage during and between tests.
- Continuous monitoring and recording of inserted length and force during insertion and retraction.
- Software to facilitate the storage of data in real time and permit display of raw data on Excel spread sheets for visualisation and analysis.

4.2 Apparatus and Instrumentation

4.2.1 Elastic modulus measurement

A simple load/extension test rig was built and is shown in figure 4.2.1. The test length for diameters of 3 mm, 4 mm and 5 mm was selected at one metre. This length was chosen as it was easy to measure the extensions generated by small masses, which were added incrementally until a suitable extension was obtained.

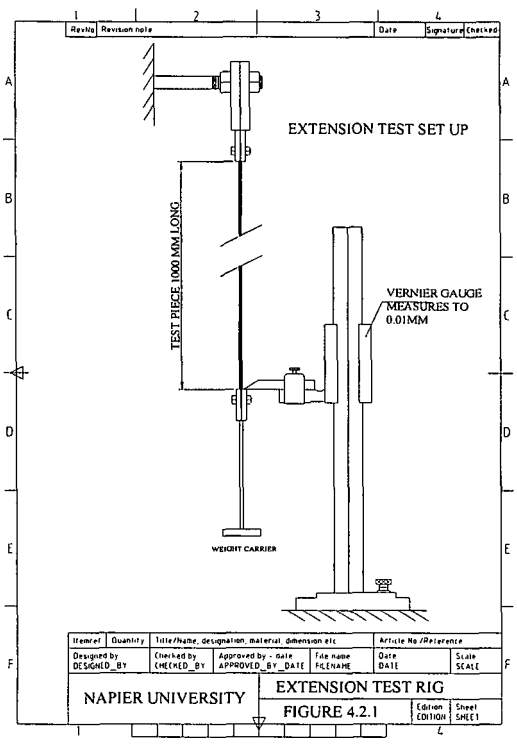

Figure 4.2.1 Extension test rig

4.2.2 Friction coefficient measurement

The friction coefficient between the elastomer material and the transparent glass constraining cylinder was obtained by use of an inclined plane test rig. The friction coefficient was also measured from the gradient of the graph of force versus distance for insertion and retraction.

4.2.3 Transparent constraining cylinder

To allow the buckling process to be observed as it takes place a transparent constraining cylinder must be used. The material used was glass as the initial use of acrylic tube cased problems due to the fact that a static electrical charge was developed during insertion of the test rod into the constraining cylinder. This caused in effect the friction to increase and buckling to occur in a shorter distance and also be non-repeatable; the use of glass eliminated these effects. A series of clamps was used to fix the range of cylinder diameters used in the tests to a base plate.

4.2.4 Rod feed mechanism

An electric stepper motor was chosen to drive the test rod via a grooved wheel running against a smooth idler pulley spring loaded against it to provide a friction drive. The electrical inputs to the stepper motor and the diameter of the feed rollers were used via software manipulation to give linear speed and position of the test rod. The stepper motor was capable of generating a holding torque at stall up to the maximum rating of the motor. This arrangement allowed the rod to be driven into the constraining cylinder at different speeds, until a pre-selected distance or force level was reached. A series of feed rollers machined to take the various sizes of rods used during the tests were made as shown in figure 4.2.2.

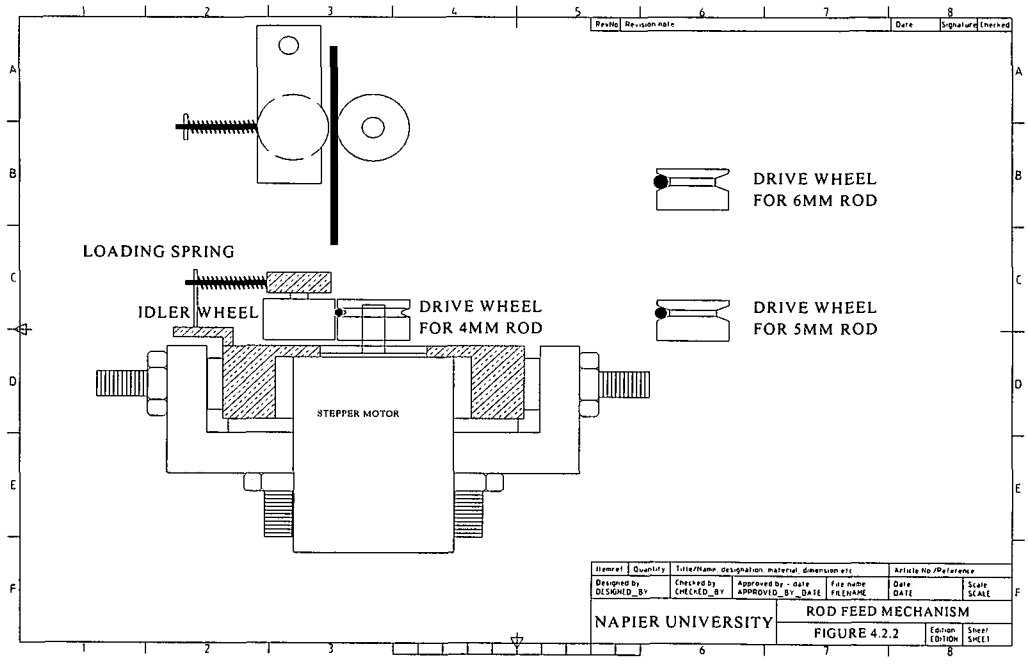

Figure 4.2.2 Rod feed mechanism

4.2.5 Linear force measurement mechanism

The insertion force was monitored by measuring the reaction applied to the rod feed mechanism via a load cell attached to the assembly. As this force was quite low, in the order of 2 N, it was imperative that the support/bearing arrangement had very low or zero friction,

to ensure that the forces measured and recorded, accurately reflected the forces being generated during insertion of the rod into the constraining cylinder.

To meet this requirement a decision was taken to use a pneumatic linear bearing arrangement to support the complete rod feed mechanism. This decision meant that a separate design and build exercise had to be undertaken to build this assembly from scratch as it was not possible to source this assembly from any manufacturer.

The basic construction is shown on figure 4.2.3 and also in photograph figure 4.2.4. It consists of a housing fitted with four horizontal pneumatic pads/bearings on which the aluminium plate mounting the rod feed mechanism floats and another four vertical pneumatic pads/bearings to locate the rod feed mechanism laterally. The aluminium plate and the rod feed mechanism float on the horizontal pads and also float between the vertical pads and is held from moving in the axial direction by the load cell.

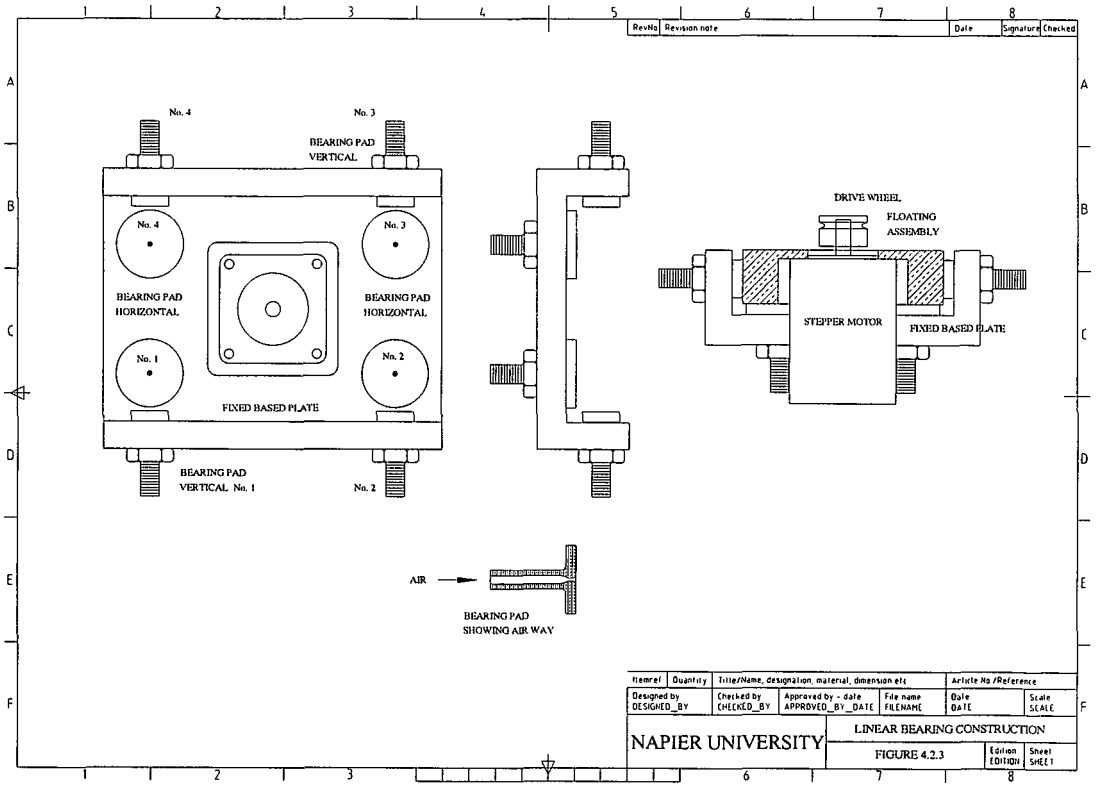

Figure 4.2.3 Linear pneumatic bearing construction

It is essential that the linear bearing assembly is level otherwise errors in the measured force level could be generated. The whole assembly is fixed to the end of the aluminium channel on which the transparent constraining cylinder is fixed, which is made absolutely level by means of jacking screws. After assembly the linear bearing arrangement was tested and it was found that the inherent friction in the system was less than 0.01 N.

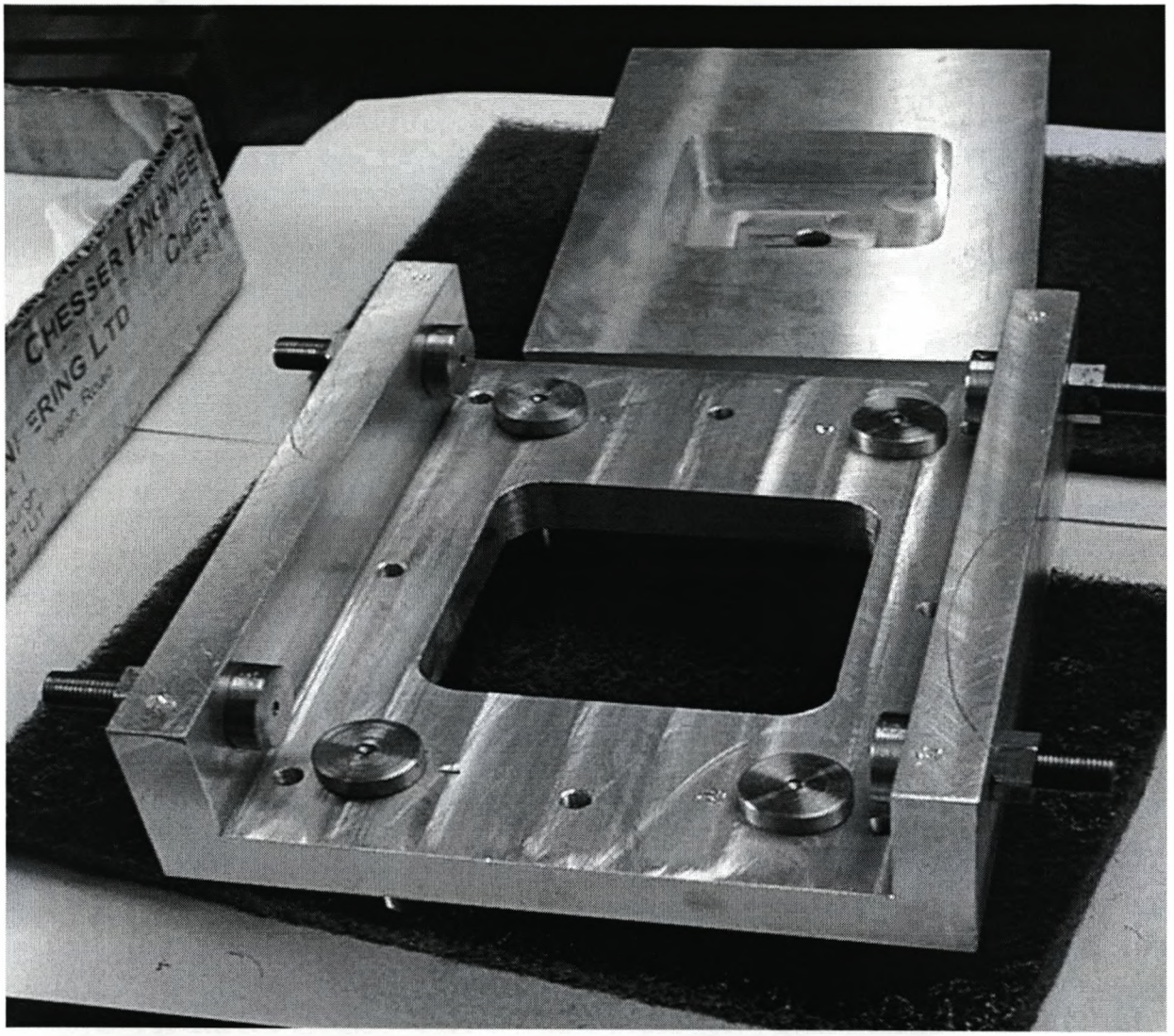

Figure 4.2.4 Linear pneumatic bearing

The design, manufacture and testing of the pneumatic bearing assembly took considerable time and effort as high precision was required in all of these areas. However without a very low friction bearing assembly it would have been very difficult to proceed with the investigation, as the results obtained would not have been reliable.

Photograph figure 4.2.5 shows the linear bearing complete with feed mechanism and load cell assembled on the test stand.

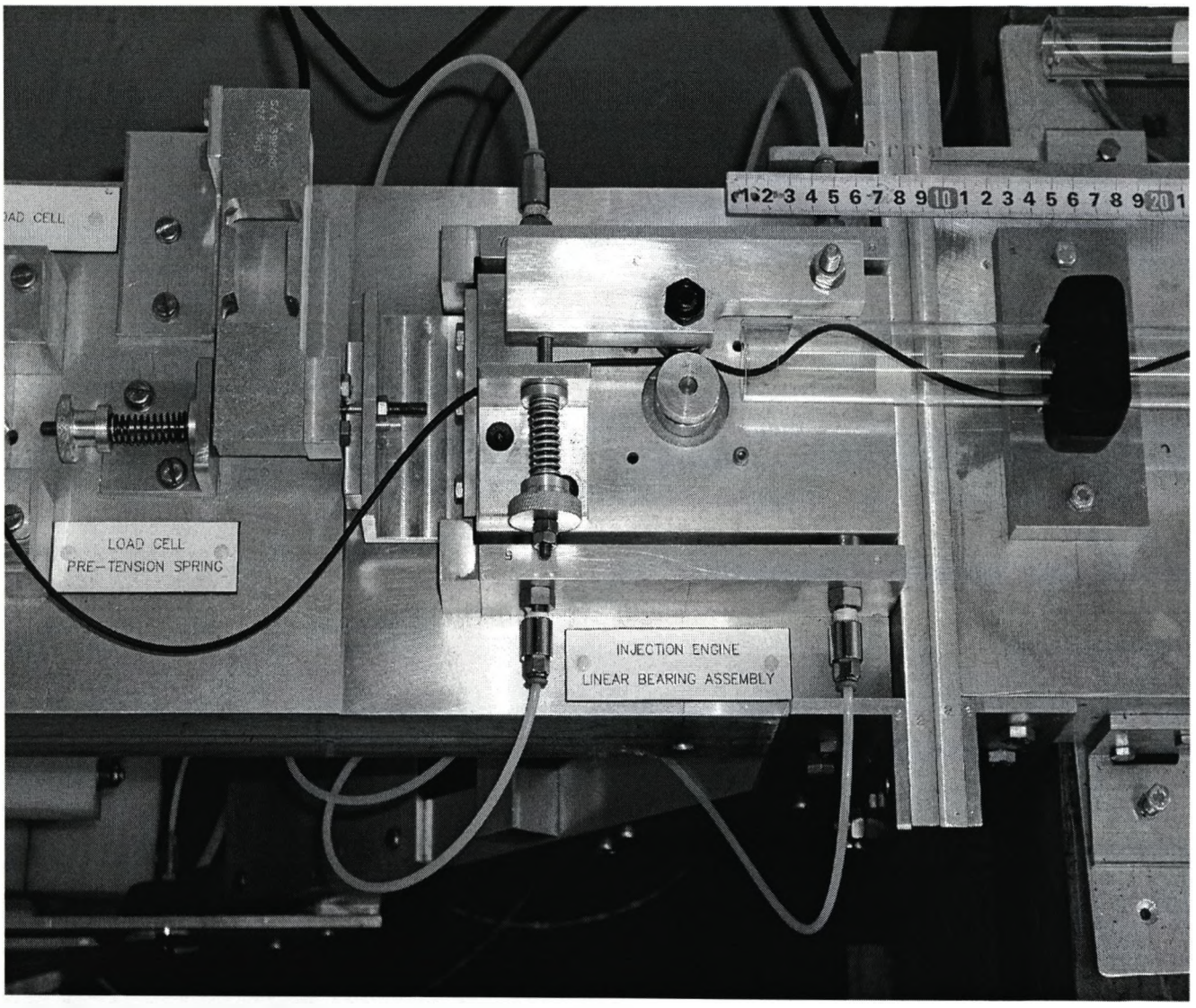

Figure 4.2.5 Linear bearing, feed mechanism and load cell assembled.

A schematic showing the pneumatic circuit and components which make up the system supplying air to this bearing assembly is shown on figure 4.2.6.

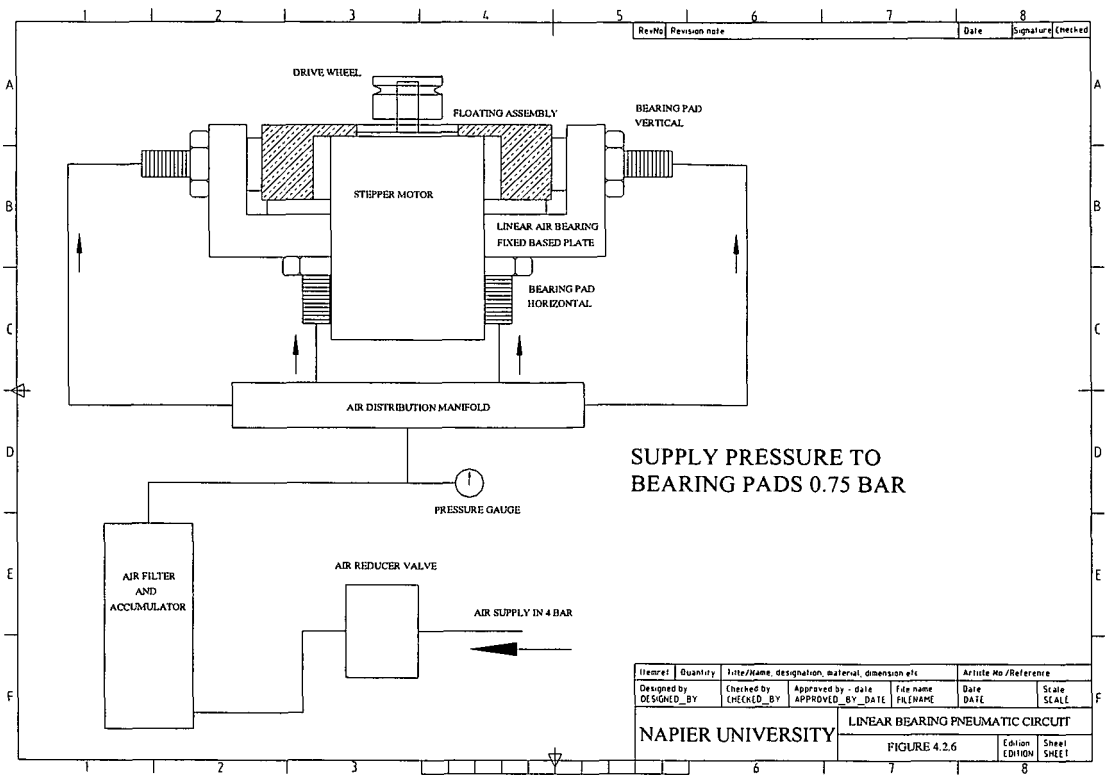

Figure 4.2.6 Linear bearing pneumatic circuit

4.2.6 Load cell

The unit chosen for the investigation was an electrical strain gauge type with a rating of 10 N. In the light of preliminary experimental work this rating was decreased to 2 N The load cell was a tension compression type, which allowed forces to be recorded during insertion of the rod into the constraining cylinder and withdrawal of the rod out of the constraining cylinder.

4.2.7 Rod storage device (rod under test)

The maximum length of rod to be inserted into the constraining cylinder is approximately 5 metres. It is essential that the rod material is stored in such a way as to be easily supplied into and out of the feed mechanism as required. A storage reel 350 mm in diameter, as shown in figure 4.2.7, was manufactured to meet this requirement.

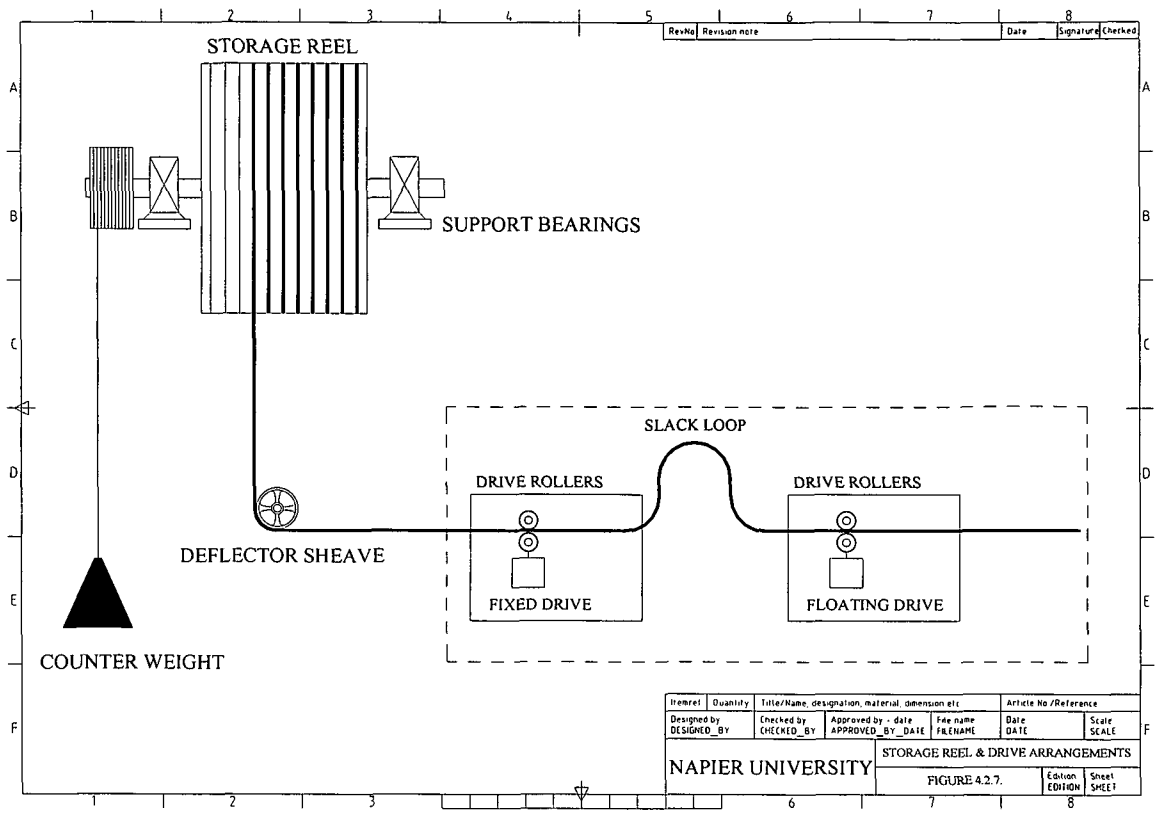

Figure 4.2.7 Storage reel and drive arrangement

To ensure that the rod feeds on to the reel consistently a spiral groove was machined to locate the rod. Also to ensure that the rod remained located in the groove a small back tension was applied by means of a dead weight acting on a smaller diameter attached to the central spindle. The diameter of this tensioning pulley was made 50 mm to ensure the deadweight only moved a fraction of the distance moved by the elastomer rod into the restraining cylinder. This ensured that the storage reel did not have to be mounted 5 metres off the floor.

Photograph figure 4.2.8 below also shows the storage reel and drive arrangements.

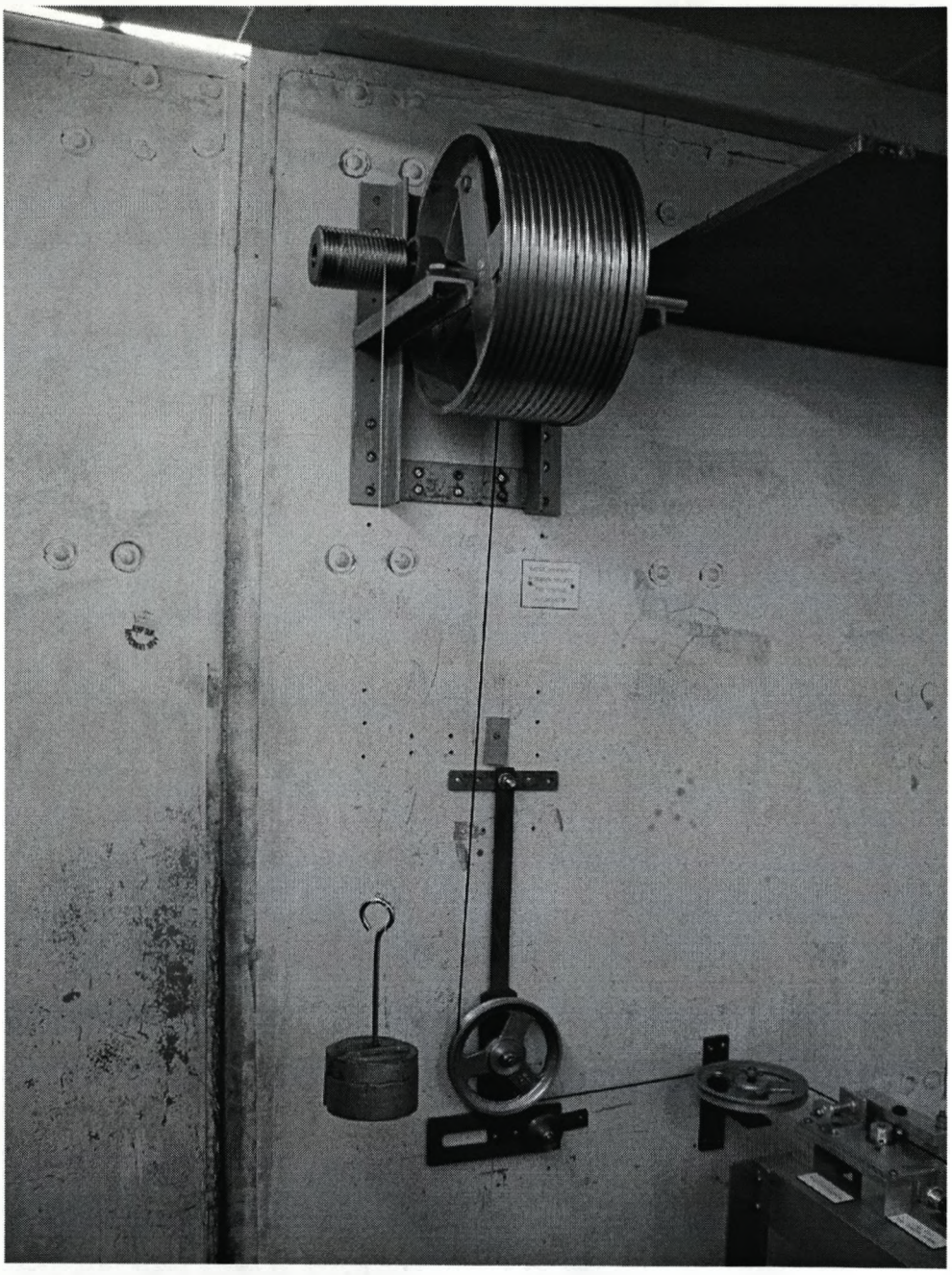

Figure 4.2.8 Storage reel arrangement

4.2.8 Rod storage device (rod stored between tests)

Only one length of rod could be stored on the storage device for the rod under test. To ensure that the other diameter rods were not damaged or marked in any way during the time between

tests they were stored on simple drums 500 mm in diameter. The rod was initially wound on to the drum and then tensioned with a dead weight.

4.2.9 Traction feed mechanism

As the back tension associated with the storage reel would have overloaded the load transducer, it was therefore necessary to provide a device between the storage reel and the feed mechanism to supply the rod with no tension into the feed mechanism. To this end another stepper motor, identical to the insertion stepper motor, with a grooved wheel running against a smooth idler pulley spring loaded against it to provide a friction drive was used, but in this case mounted directly to the base plate. This allowed the loads from the storage reel to be reacted by the additional feed mechanism and a loop of rod at zero tension to be formed and maintained between the feed mechanisms. Both stepper motors were driven at identical speeds to ensure that the zero tension loop was maintained throughout the duration of the test. This arrangement is also shown in figure 4.2.7.

The traction and feed drive arrangement are shown in a photograph, figure 4.2.9 below.

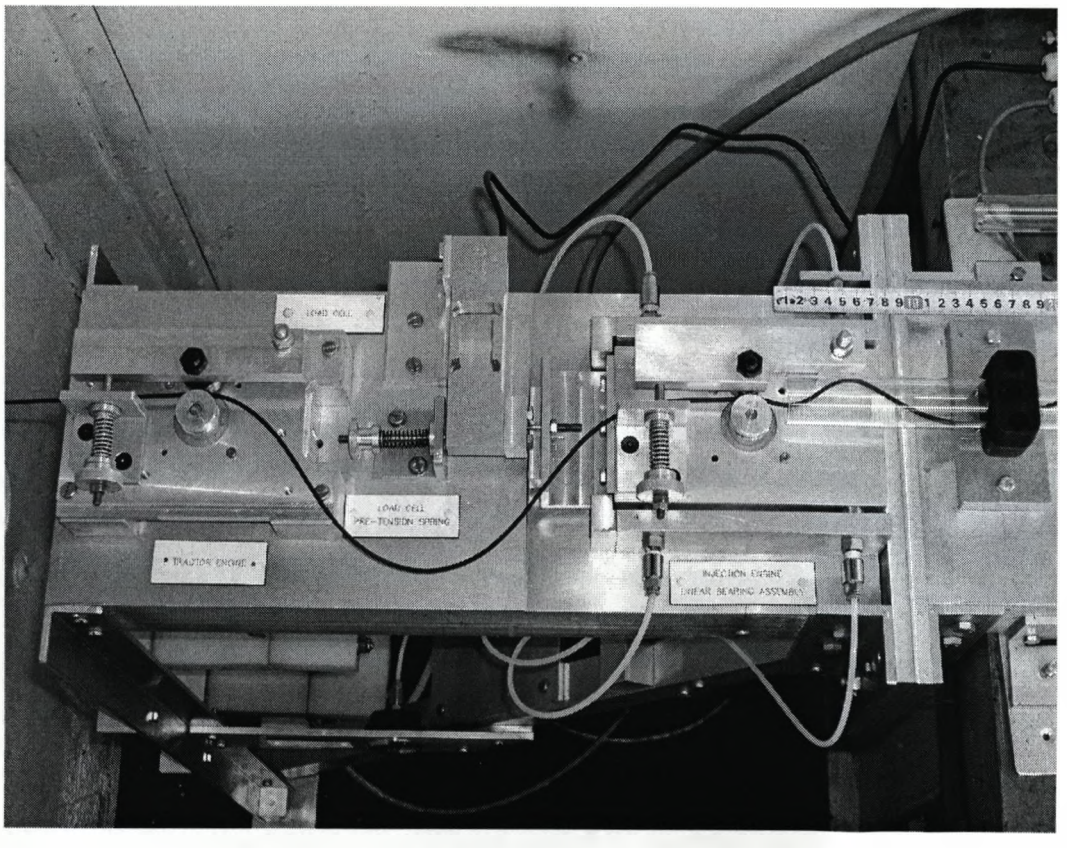

Figure 4.2.9 Traction and feed drive arrangement.

4.2.10 Electronic control cabinet

The functions to be controlled and recorded are as follows: -

- Insertion velocity of rod
- Inserted distance of rod
- Reaction force generated by insertion of rod
- Ambient temperature
- Force level at which insertion is stopped

Control of all the electrical and data logging functions was via a control panel assembly which was designed and manufactured for this project. The stepper motors were driven by special purpose electronic cards designed for the stepper motors chosen; one master and one slave to ensure speed matching.

To ensure consistent results the stepper motors are under the control of software via a programmable logic controller (PLC) mounted in the panel. A user machine interface LCD screen allows the input of insertion velocity; and the total inserted length or force level to stop the stepper motor. The reaction force generated, position and speed are monitored continuously. All of these parameters are downloaded in real time via additional software to a laptop computer via a serial link to the PLC as shown in figure 4.2.10. This stored data can be displayed on an Excel spreadsheet and various tools within Excel were used for analysis. The data acquisition and control software was designed and developed specifically for this project, and integrated by use of a SCADA software package.

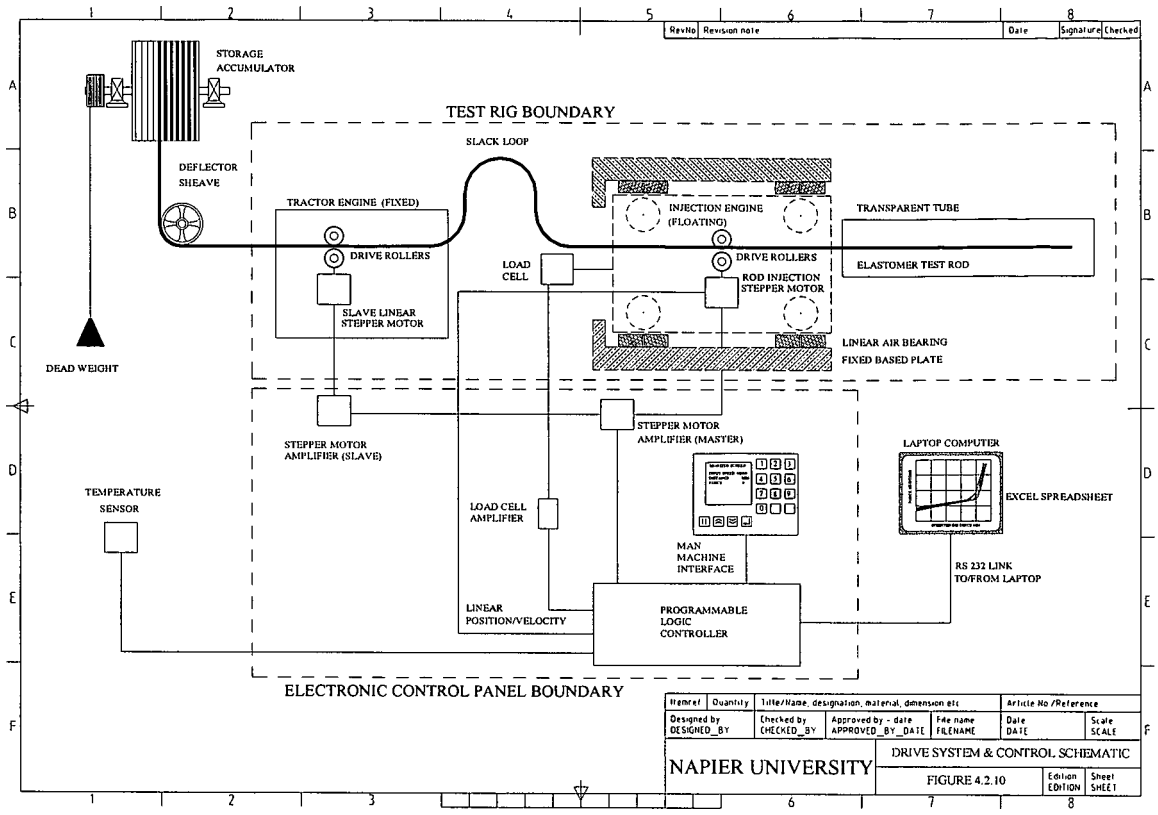

Figure 4.2.10 Drive system & control schematic.

Calibration for all of the parameters listed above was carried out using equipment which had been calibrated by a certified test house against National Standards, and covered stop watch, distance scales, test loads and thermometer.

5. Experimental Work

5.1 Preliminary Work

This section discusses the work carried out to determine the elastic modulus for the rod material and friction coefficient for the rod/glass tube materials chosen for the investigation.

5.1.1 Elastic modulus

In real oil wells the material used is alloy steel, which has a modulus of elasticity of approximately 210 GN/m^2. This material, combined with the friction coefficient for lubricated steel on steel of approximately 0.1, results in an inserted length in the order of 2000 m before helical buckling and lock up occur.

A test rig of this length would be completely impractical. To investigate this phenomena under controlled conditions in a laboratory, the length for helical buckling and lock up to occur must be less than approximately ten metres.

Since the modulus of elasticity and the frictional coefficient between the rod and the restraining tube play a dominant role in the buckling phenomena being investigated, a rod with a low modulus and high friction coefficient had to be used to model the system as realistically as possible.

A number of materials were selected for test, which, in addition to suitable material properties were also commercially available in a range of diameters and at relatively low cost. The materials with low elastic moduli were tested in a simple manner using a transparent cylinder, introducing the test rod material by a simple feed mechanism and observing the distance achieved before helical buckling occurred. This approach enabled a relatively high number of materials to be tested in a relatively short space of time. It also showed very clearly in a qualitative way the material with the best elastic modulus/friction coefficient combination for the proposed tests.

Materials tested included several types of elastomers, various grades of nylon and spirally wound steel plastic coated curtain rod.

The material finally selected for use on the scale rig was an elastomer, which was commercially available as solid rod in a range of diameters from 2 mm to 8mm and at low cost. The elastic modulus of elastomers is, however, not linear over a wide range and also shows a variation from tension to compression. However, over a range where the extension is less that about three percent, the stress/strain curve is linear, and the modulus has the same value in tension and compression (M.R.P.A., 1974).

Initial simple quantitative tests revealed that helical buckling occurred with compressive loads well below the three percent figure given above, which allowed the confident use of an elastomer type material in this study.

The manufacturers of this material were not able or unwilling to give catalogue data for the elastic modulus or friction coefficient. As a consequence of this it was necessary to build test equipment to measure these parameters.

A simple load/extension test rig was built as previously shown in figure 4.2.1. The test length for diameters of 3 mm, 4 mm, 5 mm and 6mm was selected at one metre. This length was chosen as it was easy to measure the extensions generated by 10 gram masses, which, were added incrementally until a maximum extension of three percent was obtained. This test was repeated over a temperature range of 10 to 23 degrees centigrade. Equipment used for measurements during the tests had been calibrated by a certified test house against National Standards, and covered dial gauge, test loads and thermometer. Data from the extension versus load tests were recorded on an Excel spread sheet. These values were plotted on a graph and linear regression techniques, which are included in the Excel spreadsheet package, were used to determine the modulus of elasticity.

5.1.2 Friction coefficient

The friction coefficient between the elastomer material and the transparent glass constraining cylinder was obtained by use of an inclined plane test rig.

The friction coefficient was measured by raising the glass tube containing a sample length of rubber until sliding was achieved. The coefficient was calculated from the tangent of the angle obtained during this test.

The friction coefficient resulting from the combination of the chosen elastomer and the glass tube ranged from approximately 0.5 to 1.0, which is approximately five times that of steel on steel.

This combination of low elastic modulus and high friction coefficient was considered sufficiently good to allow the design and construction of a test rig to be undertaken which would reflect accurately what happens in a real well but in a distance of less than five metres.

5.2. Experimental Technique

5.2.1 Method for obtaining penetration results

The object of this experimental work was to obtain data giving the relationship between the inserted distance and the insertion force as the rod was driven into the constraining cylinder until helical buckling had taken place and the rod locked up in the cylinder. The test equipment which handles the storage and feeding the rod into the tube has been described in the previous section.

During insertion of the rod into the tube distance and force were recorded continuously at 50 millisecond intervals, giving approximately 300 points for each test. The rod was inserted until the buckling of the rod was in a fully developed helical state and lock up had occurred. Determination of the level of force necessary to cause lock up to occur had been carried out

previously and this value was used via the control system to stop the insertion stepper motor and recording of data when this level of force was reached. This was to ensure that the test ran continuously from start at zero force until maximum force when lock up had occurred and the recorded data reflected accurately what was happening throughout the insertion test.

Tests were also carried out at a range of velocities from 50 mm/s to 120 mm/s but this had an insignificant effect on total distance achieved before lock up occurred with the elastomer/glass combination.

The tests were carried out using rods with diameters of 2, 3, 4, 5 and 6 mm in constraining glass tubes with internal diameters of 8.6, 13, 15, 19, 22.8, 28.6 and 33.4 mm. This enabled a full examination of the impact of rod stiffness and *L/d* ratio. These results are shown in Section 6.

Referring to the graphs of inserted distance against force it is clear that they consist of three basic parts; a linear section with a slightly positive gradient, a curved transitional section and a final exponential section. These parts of the graph reflect respectively sinusoidal, transition to helical and fully developed helical buckling.

The first part reflected the increase in frictional force as an increasing length, and hence mass of rod, was inserted into the glass tube. In this section the rod is lying on the bottom of the tube. As the inserted distance increases the rod starts to buckle sinusoidally with low amplitude and large pitch distances. With increasing amplitude the rod moves round and up the inner surface of the transparent cylinder.

The second curved section is where the rod is transitioning from sinusoidal to helical buckling and the force increases at a higher and non-linear rate compared with the first section.

The third and final section is where the rod has gone completely into helical buckling and lock-up has occurred with the force level rising exponentially.

5.2.2 Friction coefficient cross check

The data recording procedures were modified to record the position and force as the rod was driven into the glass tube and also to record the same as the rod was pulled out of the tube. Pulling or retracting the rod out would ensure that the rod was straight and lying in the bottom of the tube and as a consequence the friction coefficient would be measured accurately. This confirmed that the friction coefficient for insertion in the sinusoidal zone and for retraction was the same in both cases.

5.2.3 Insertion-retraction data display

A large amount of data is recorded on each rod-tube combination and 10 sets of data are recorded for each combination. To enable the data to be clearly viewed the insertion and retraction graphs were plotted on separate sheets.

6. Experimental Results

6.1 Elastic Modulus

The data obtained from the extension tests are plotted as a graph of elastic modulus against temperature as shown below in figure 6.1.1. The modulus of elasticity is about four orders of magnitude lower that that of steel.

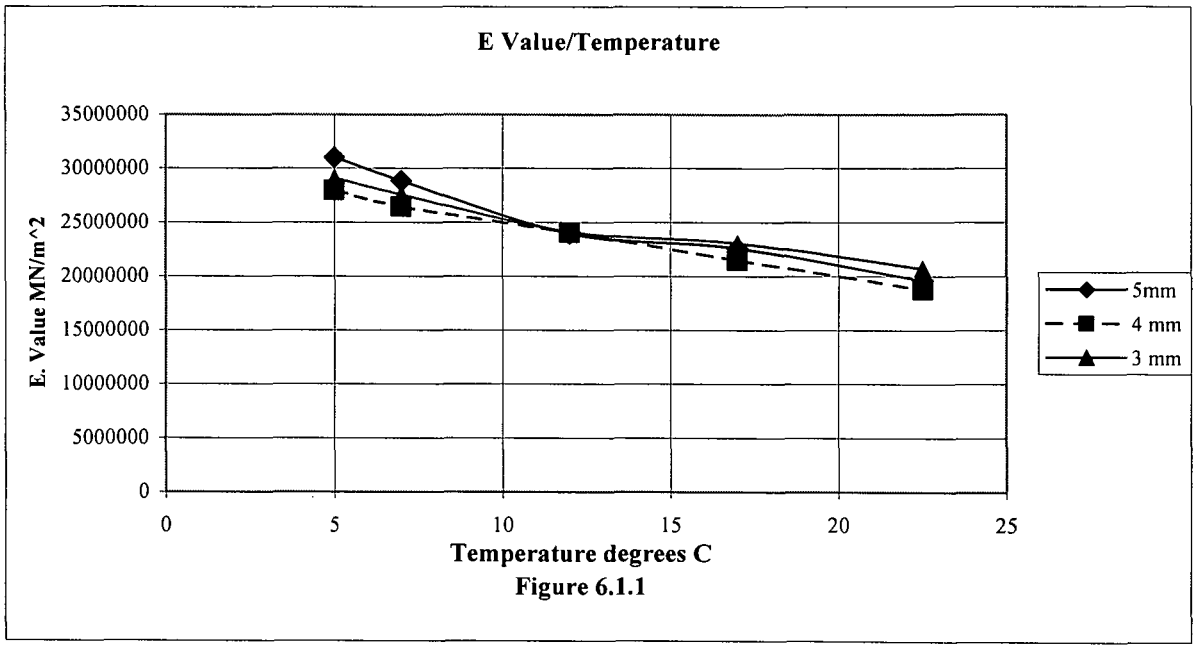

Figure 6.1.1

Figure 6.1.1 Elastic modulus versus temperature

From the graph, it can be seen that over the working temperature range of 13 to 18 ^{o}C, an average value for the elastic modulus of 23 MN/m^2 can be assumed.

6.2 Friction Coefficient

The friction coefficient between the elastomer material and the transparent glass constraining cylinder was obtained by use of inclined plane test rig. The friction coefficient resulting from the combination of the chosen elastomer and the glass tube was determined.

It should be noted that the method employed determined the value of the static friction coefficient, whereas during the insertion experiments the dynamic values of the friction coefficient should be used. Because of this it was decided that the values of the dynamic friction coefficient would be determined during the insertion tests (section 6.6.1).

6.3 Qualitative Observations

The combination of low elastic modulus and high friction coefficient chosen was considered sufficiently good to allow the design and construction of a test rig to be undertaken with a high degree of confidence that the data produced would reflect accurately what happens in a real well but in a distance of less than five metres.

All experimental results for the insertion of the rod into the tube demonstrate similar qualitative trends, shown in Figure 6.3.1, which was obtained during the preliminary tests, using $d = 3$ mm and an acrylic tube with $D = 14$ mm.

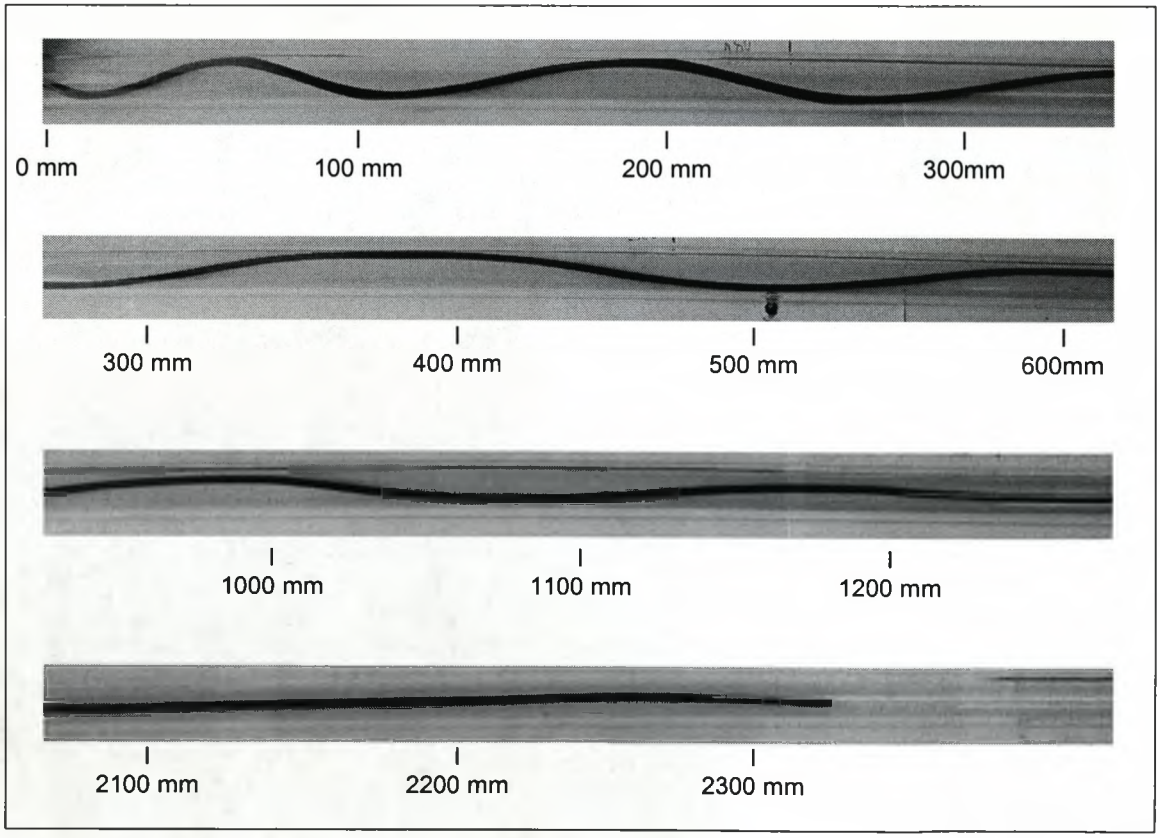

Figure 6.3.1 Deformation trends in plan view.

The rod initially enters the tube in a straight line. After a certain rod length is inserted, the rod following the initial straight section starts deforming. The initial deformations appear sinusoidal with the amplitude considerably smaller than the radius of the tube. With further insertion the length of the sinusoidal cycles decreases and the amplitude increases. As the amplitude increases the deformed rod starts to move progressively up the walls of the tube. This continues until a situation obtains when helical deformations (result of helical buckling) suddenly appear. Hence the shape of the rod being inserted into the tube consists of three regions: the initial, apparently straight section, the subsequent section with sinusoidal deformation and the final section with helical deformation. The region with the fully developed helical deformations is relatively small, and is confined to about the last 10% to 20% of the inserted rod. It should be pointed out that the force required to insert the rod increases considerably when helical deformations are present. The insertion is terminated (and lock up occurs) when the force required for further insertion is greater than the force developed by the insertion mechanism.

Figure 6.3.1 shows clearly the development of sinusoidal buckling within the tube and the relevant inserted distances. Since the measurement of the buckled shapes was not a primary objective of this work, only a small number of these experiments were performed and estimates made on the number of deformations. These are summarised in the table given in figure 6.3.2.

rod diameter d [mm]	tube diameter D [mm]	maximum inserted length [mm]	number of sinusoidal cycles	number of helical cycles
3	15	1600	~10	~2
3	22.8	1000	~7	~2
3	33.4	950	~5	~1

Figure 6.3.2 Table giving description of rod deformation.

6.4 Insertion Tests

The objective of an insertion test was to establish the load/insertion relationship for a particular diameter of rod and tube. With the range of rod diameters (4) and tube diameters (7) available, this allowed a comprehensive picture to be determined.

The experimental results for the insertion tests are presented as graphs of the required insertion force against the inserted length. Each graph shows a large number of experimental runs, and, typically, about 10 runs were taken for each D/d configuration.

The results for $D = 8.6$ mm are presented for $d = 3$ mm in figure 6.4.1. The ambient temperature during these series of experiments was 13 °C. Results are not presented for any other rod diameters in this case. The reason is that the total insertion lengths were too high for the experimental apparatus used in the present experiments. The results for $D = 13$ mm are presented for $d = 3$ mm and $d = 6$ mm in figures 6.4.2 and 6.4.3 respectively. The results for $D = 15$ mm are presented for $d = 3$ mm, $d = 4$ mm, $d = 5$ mm and $d = 6$ mm in figures 6.4.4, 6.4.5, 6.4.6 and 6.4.7 respectively. The results for $D = 19$ mm are presented for $d = 3$ mm, $d = 4$ mm, $d = 5$ mm and $d = 6$ mm in figures 6.4.8, 6.4.9, 6.4.10 and 6.4.11 respectively. The results for $D = 22.8$ mm are presented for $d = 3$ mm, $d = 5$ mm and $d = 6$ mm in figures 6.4.12, 6.4.13 and 6.4.14 respectively. The results for $D = 28.6$ mm are presented for $d = 3$ mm and $d = 6$ mm in figures 6.4.15 and 6.4.16 respectively. The results for $D = 33.4$ mm are presented for $d = 3$ mm, $d = 5$ mm and $d = 6$ mm in figures 6.4.17, 6.4.18 and 6.4.19 respectively.

Typical experimental data are extracted from figures 6.4.1 to 6.4.19 and presented in two different ways: (i) for constant diameter of the containing cylinder D and (ii) for constant diameter of the rod d.

Figure 6.4.20 shows the variation of the insertion force with the inserted length for $D = 13$ mm and two different diameters of the rod: $d = 3$ mm and $d = 6$ mm. figure 6.4.21 shows the variation of the insertion force with the inserted length for $D = 19$ mm and four different diameters of the rod: $d = 3$ mm, $d = 4$ mm, $d = 5$ mm and $d = 6$ mm. figure 6.4.22 shows the variation of the insertion force with the inserted length for $D = 28.6$ mm and two different

diameters of the rod: $d = 3$ mm and $d = 6$ mm. Finally, figure 6.4.23 shows the variation of the insertion force with the inserted length for $D = 33.4$ mm and two different diameters of the rod: $d = 5$ mm and $d = 6$ mm.

Figure 6.4.24 shows the variation of the insertion force with the inserted length for $d = 3$ mm and five different diameters of the containing cylinder: $D = 33.4$ mm, $D = 28.6$ mm, $D = 19$ mm, $D = 13$ mm and $D = 8.6$ mm. figure 6.4.25 shows the variation of the insertion force with the inserted length for $d = 6$ mm and four different diameters of the containing cylinder: $D = 33.4$ mm, $D = 28.6$ mm, $D = 19$ mm and $D = 13$ mm.

All but two figures show consistent trends, as discussed later. Two sets of data in Figure 6.4.16 diverge from the remaining eight sets. The reason is most probably surface contamination which increases significantly the friction coefficient. This is probably also the reason why Figure 6.4.24 shows that the maximum penetration is smaller for the bigger diameter rod.

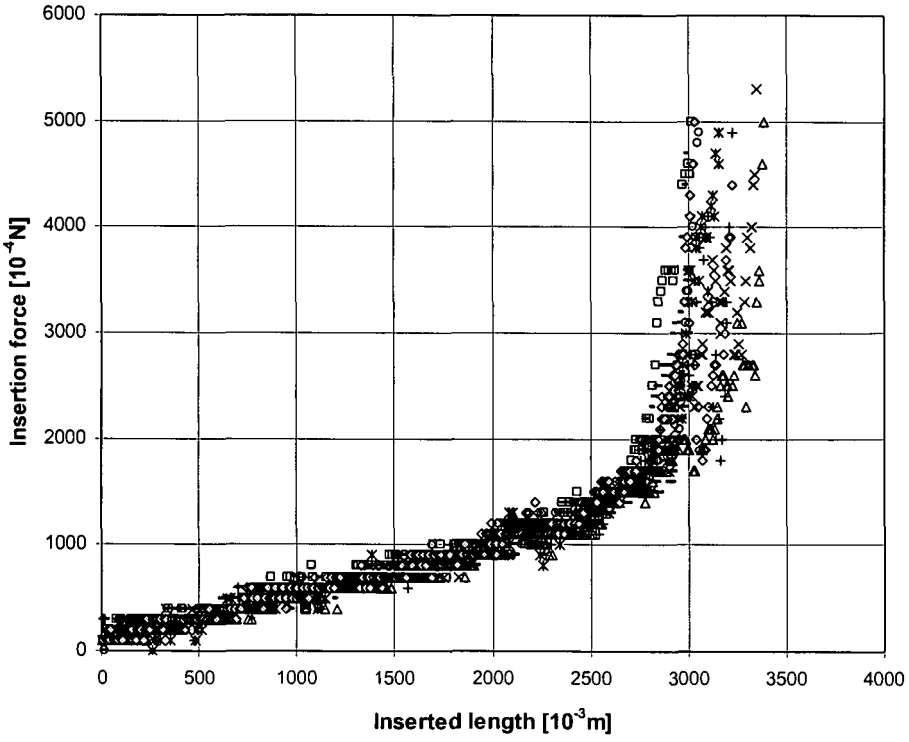

Figure 6.4.1 Plot of the insertion force versus the inserted length for $d = 3$ mm, $D = 8.6$ mm ($T = 13$ ^{o}C).

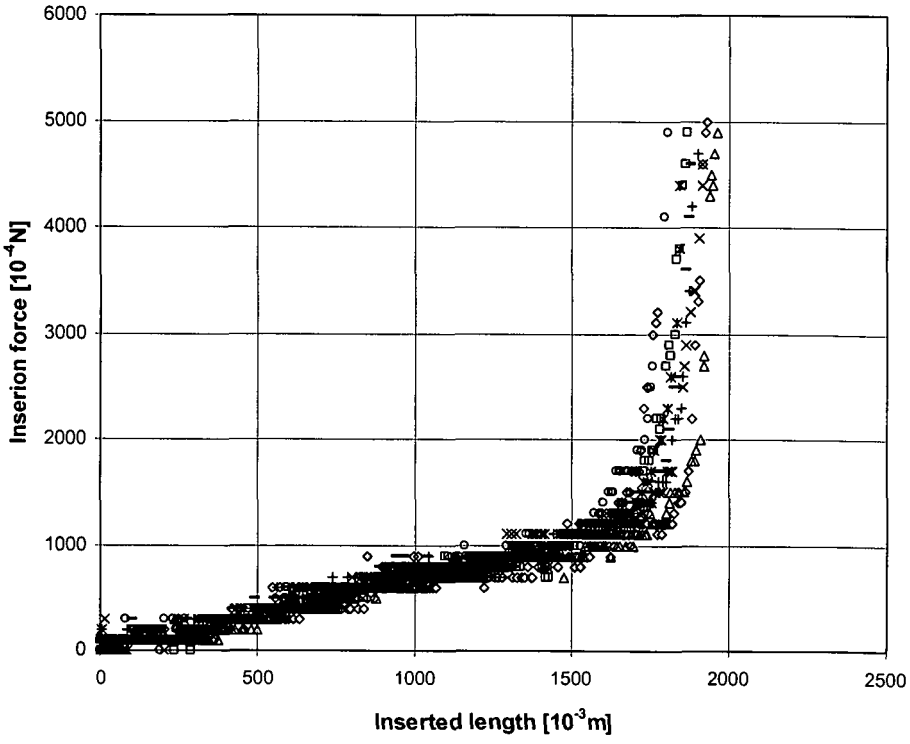

Figure 6.4.2 A plot of the insertion force versus the inserted length for $d = 3$ mm, $D = 13$ mm ($T = 13$ C).

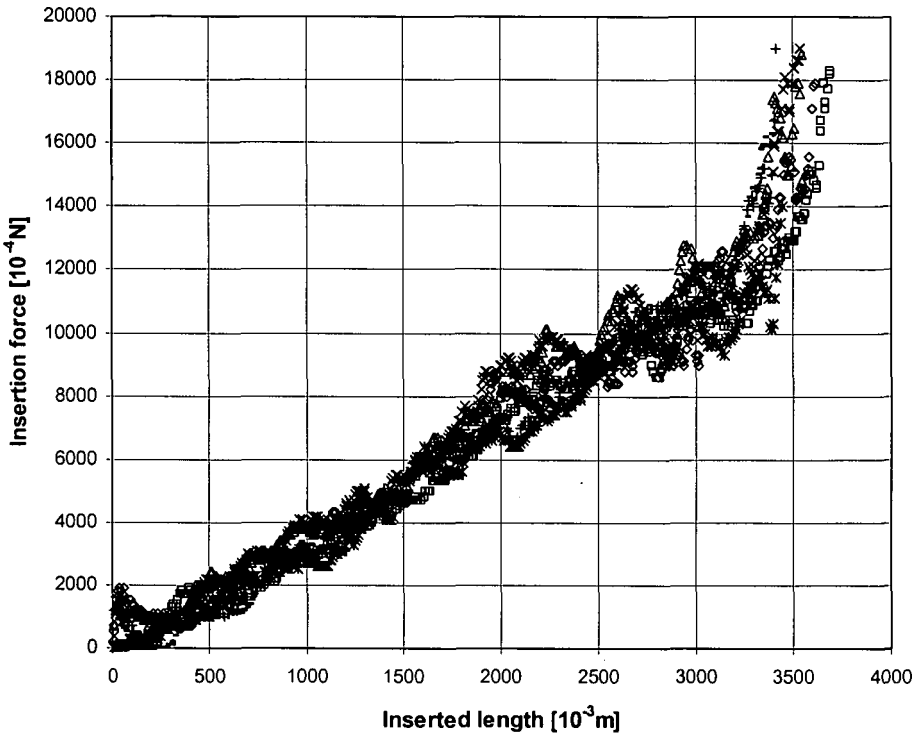

Figure 6.4.3 Plot of the insertion force versus the inserted length for $d = 6$ mm, $D = 13$ mm ($T = 18$ C).

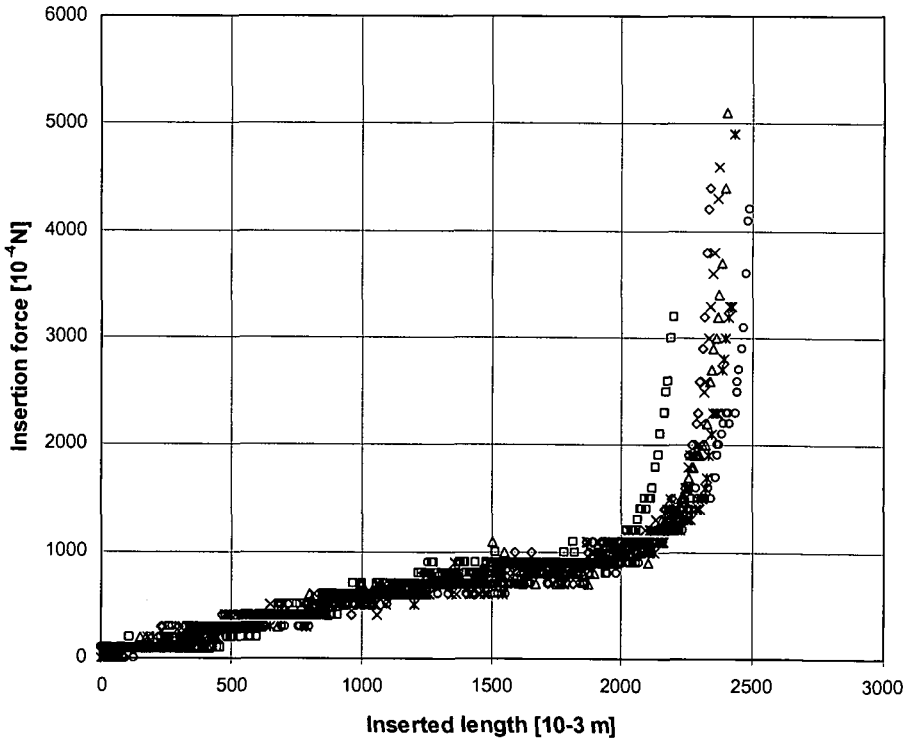

Figure 6.4.4 Plot of the insertion force versus the inserted length for $d = 3$ mm, $D = 15$ mm ($T = 18$ C).

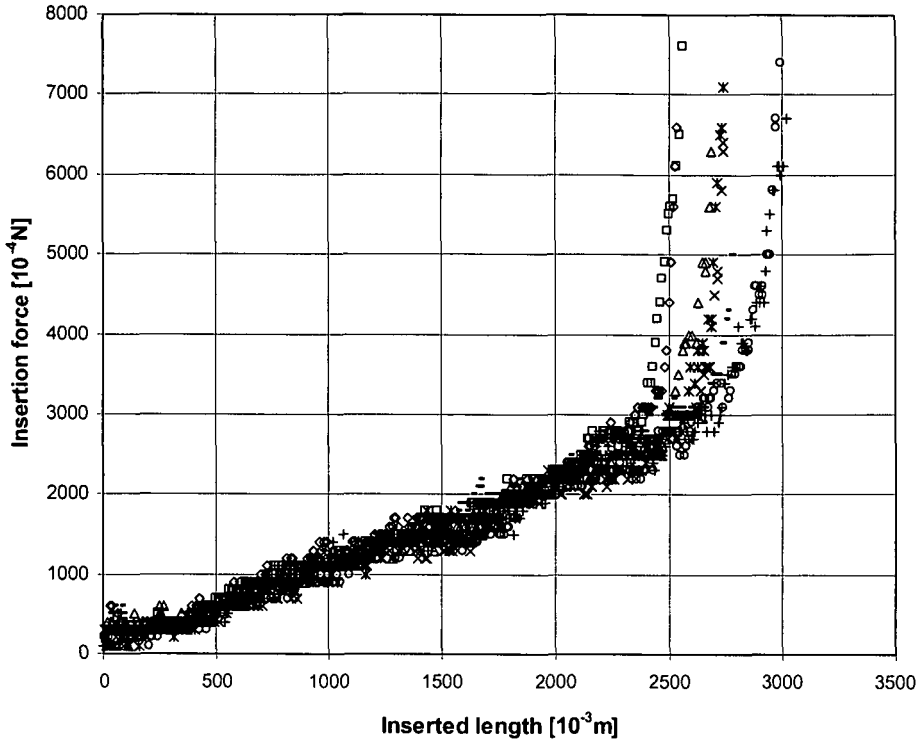

Figure 6.4.5 Plot of the insertion force versus the inserted length for $d = 4$ mm, $D = 15$ mm ($T = 18$ C).

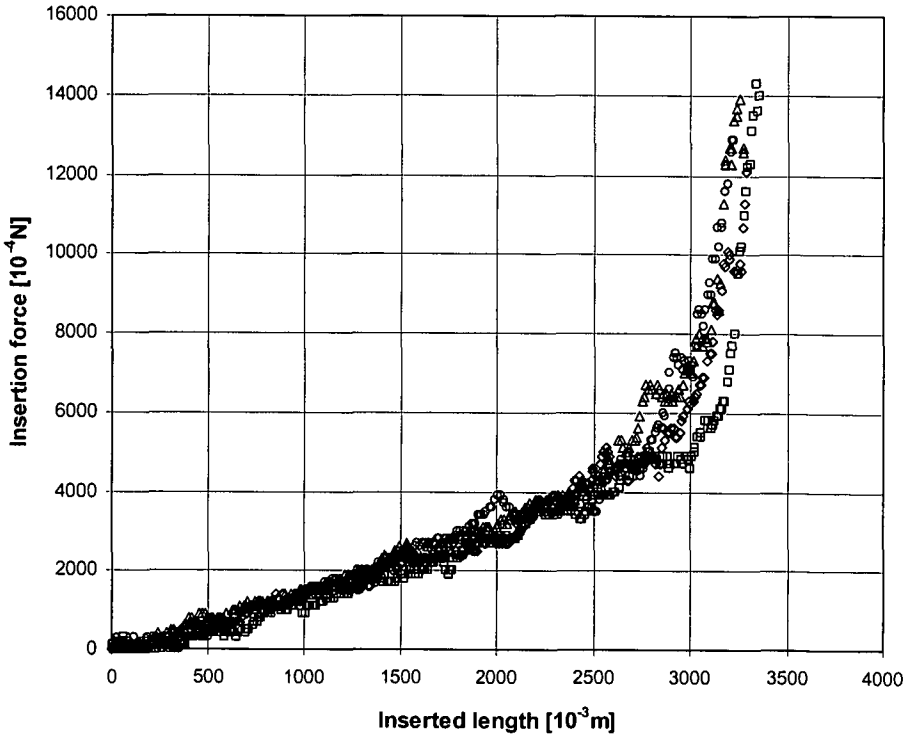

Figure 6.4.6 Plot of the insertion force versus the inserted length for $d = 5$ mm, $D = 15$ mm ($T = 18$ C).

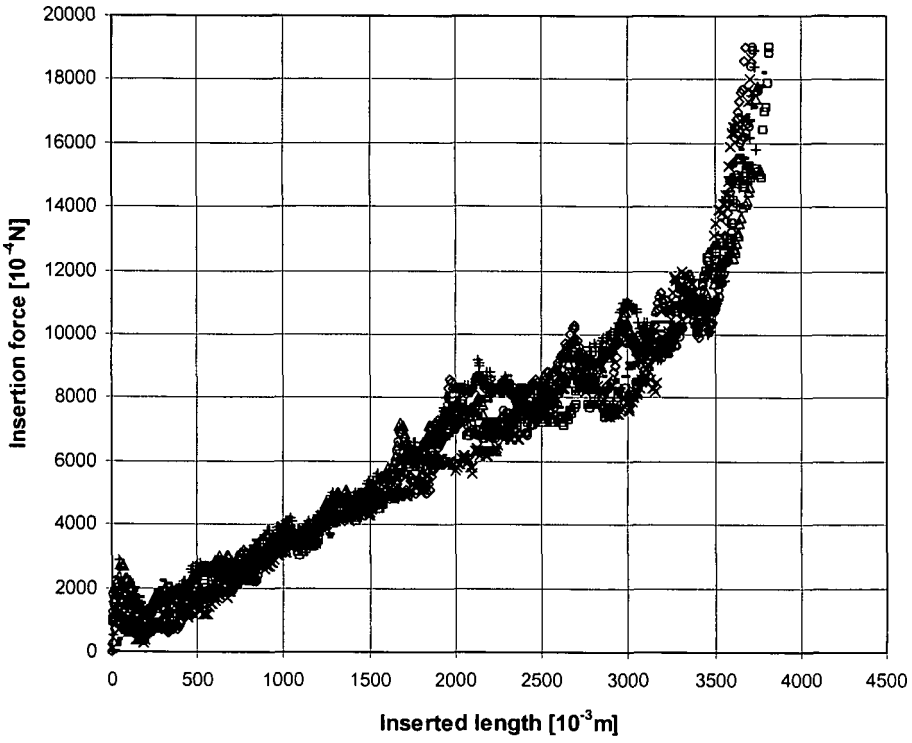

Figure 6.4.7 Plot of the insertion force versus the inserted length for $d = 6$ mm, $D = 15$ mm ($T = 17$ C).

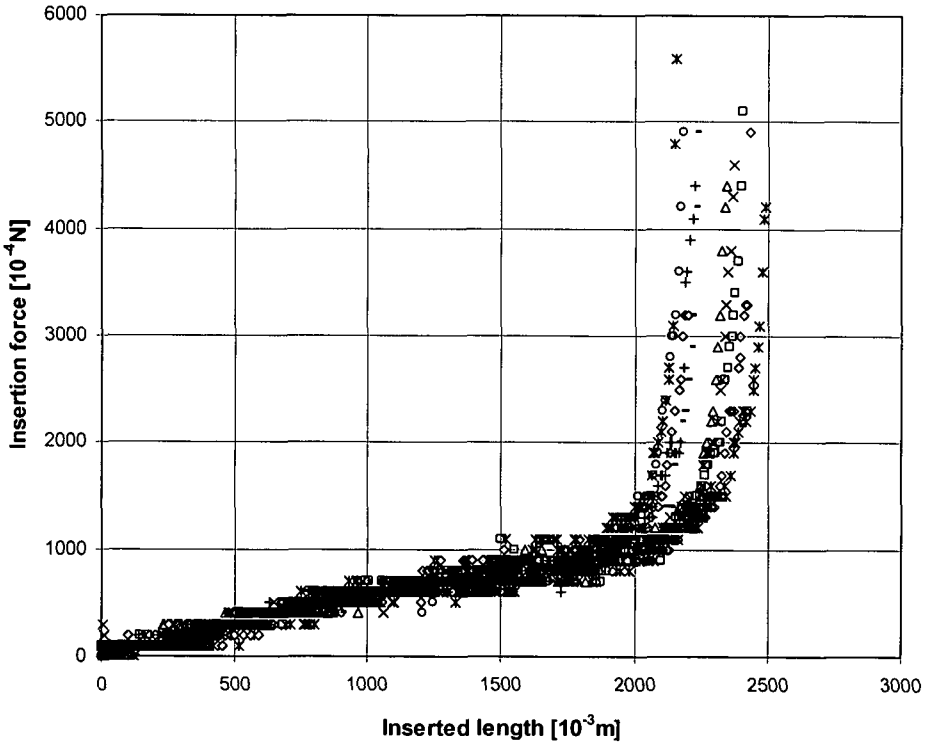

Figure 6.4.8 Plot of the insertion force versus the inserted length for $d = 3$ mm, $D = 19$ mm ($T = 12$ C).

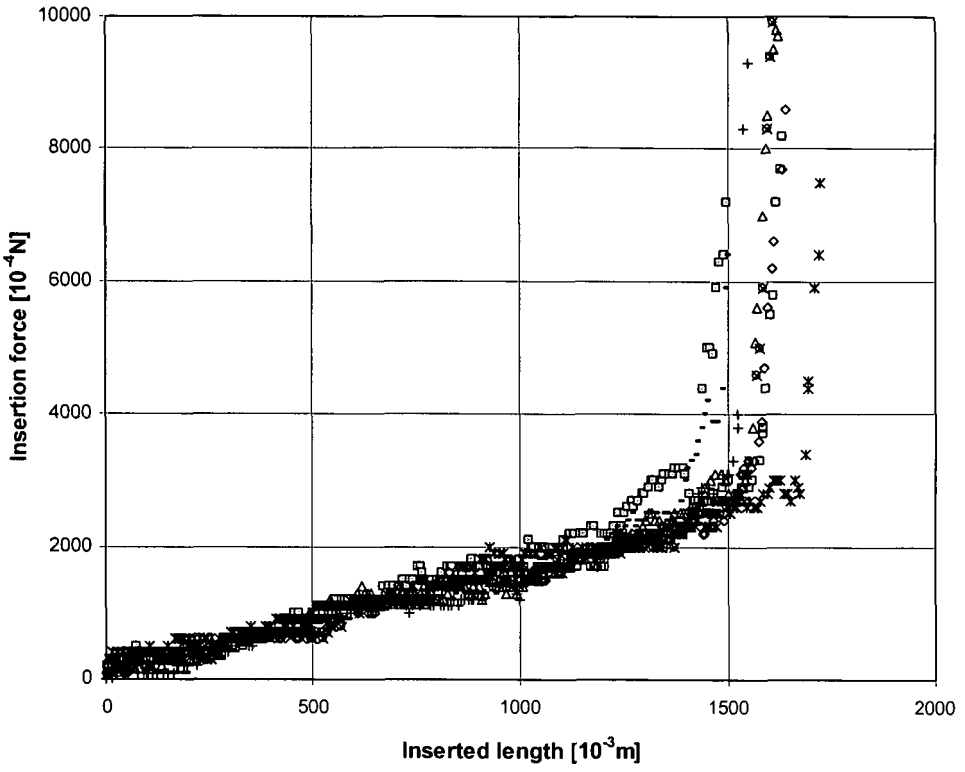

Figure 6.4.9 Plot of the insertion force versus the inserted length for $d = 4$ mm, $D = 19$ mm ($T = 14$ C).

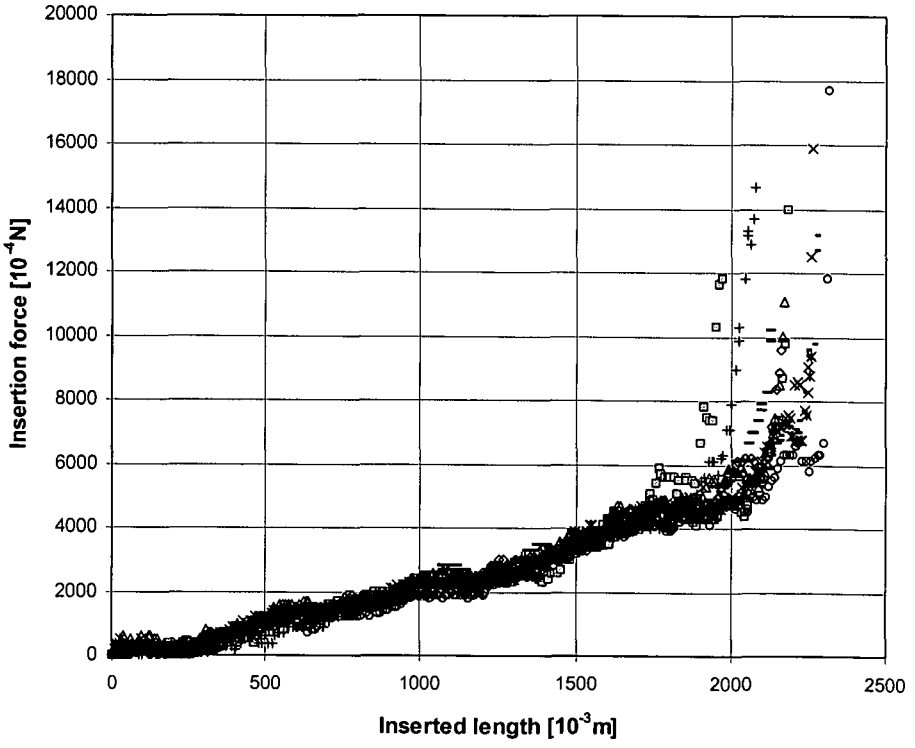

Figure 6.4.10 Plot of the insertion force versus the inserted length for $d = 5$ mm, $D = 19$ mm ($T = 18$ C).

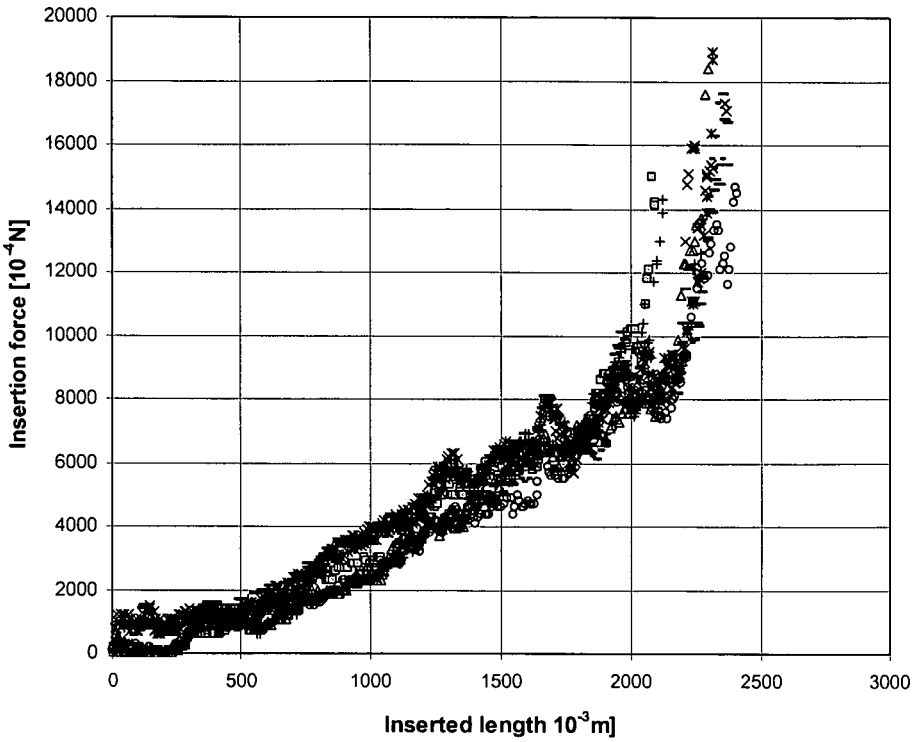

Figure 6.4.11 Plot of the insertion force versus the inserted length for $d = 6$ mm, $D = 19$ mm ($T = 18$ C).

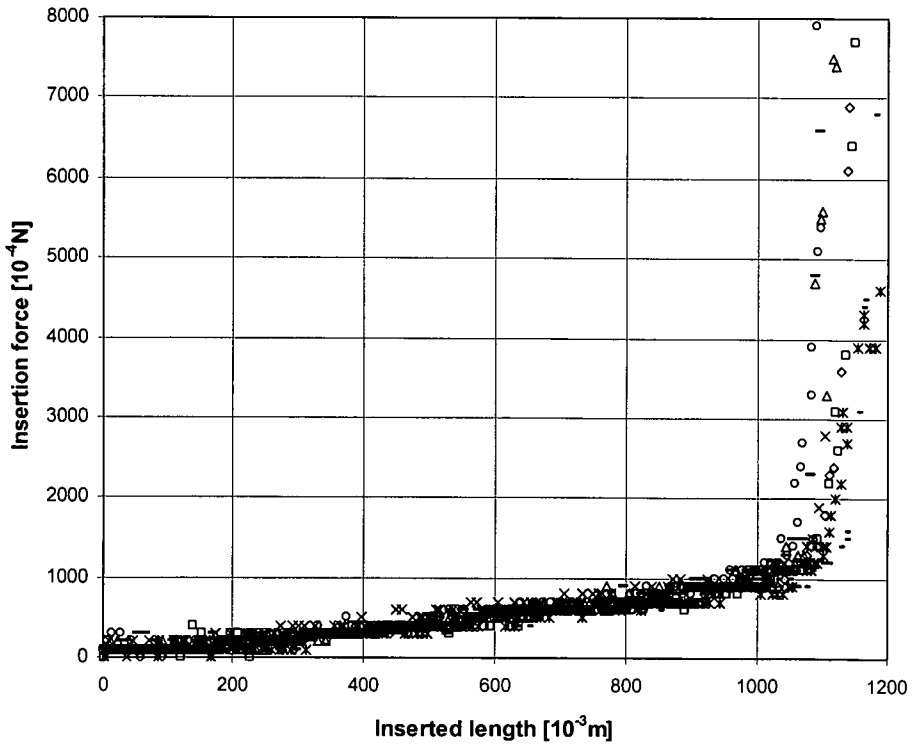

Figure 6.4.12 Plot of the insertion force versus the inserted length for $d = 3$ mm, $D = 22.8$ mm ($T = 13$ C).

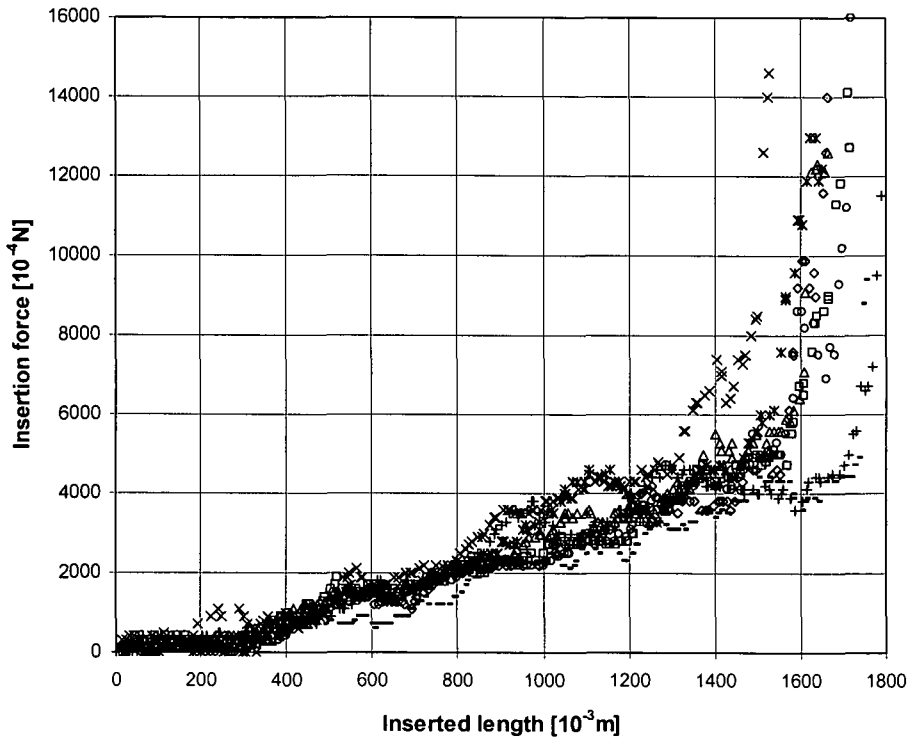

Figure 6.4.13 Plot of the insertion force versus the inserted length for $d = 5$ mm, $D = 22.8$ mm ($T = 18$ C).

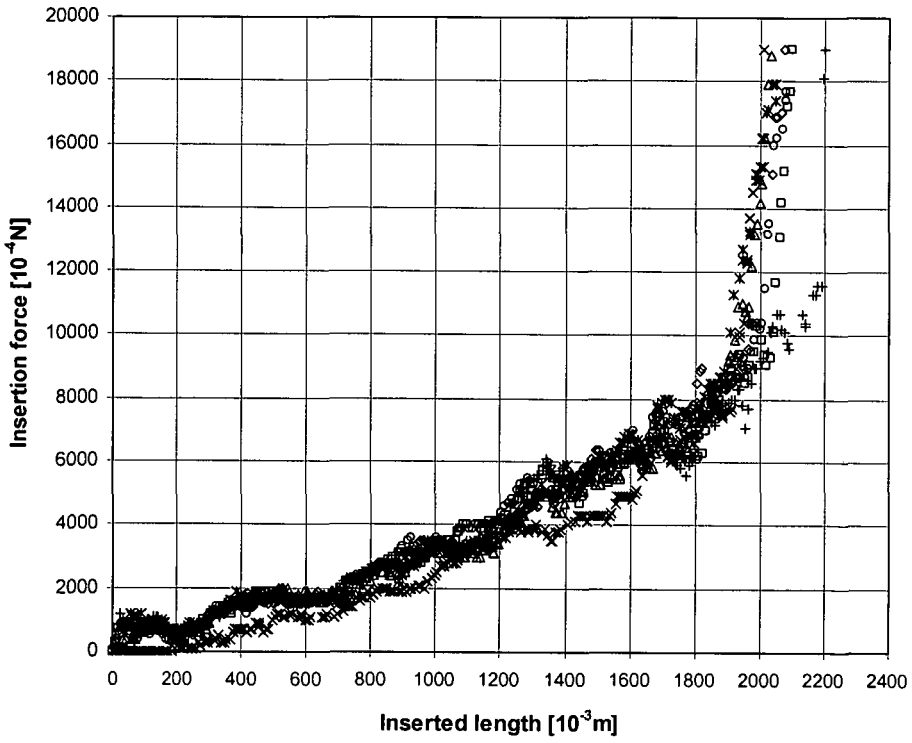

Figure 6.4.14 Plot of the insertion force versus the inserted length for $d = 6$ mm, $D = 22.8$ mm ($T = 19$ C).

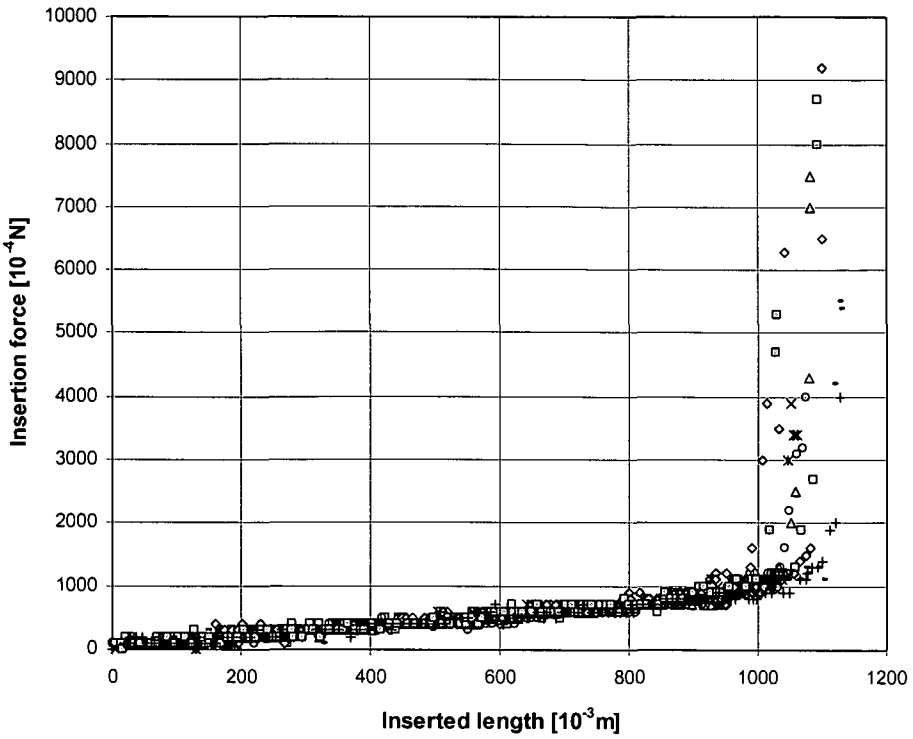

Figure 6.4.15 Plot of the insertion force versus the inserted length for $d = 3$ mm, $D = 28.6$ mm ($T = 13$ C).

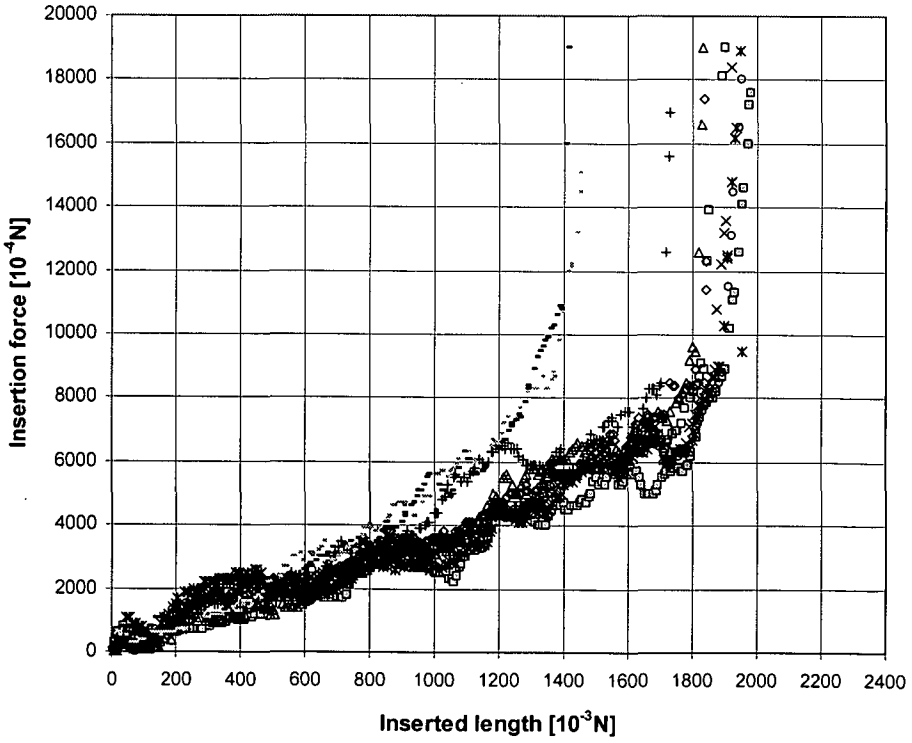

Figure 6.4.16 Plot of the insertion force versus the inserted length for $d = 6$ mm, $D = 28.6$ mm ($T = 20$ C).

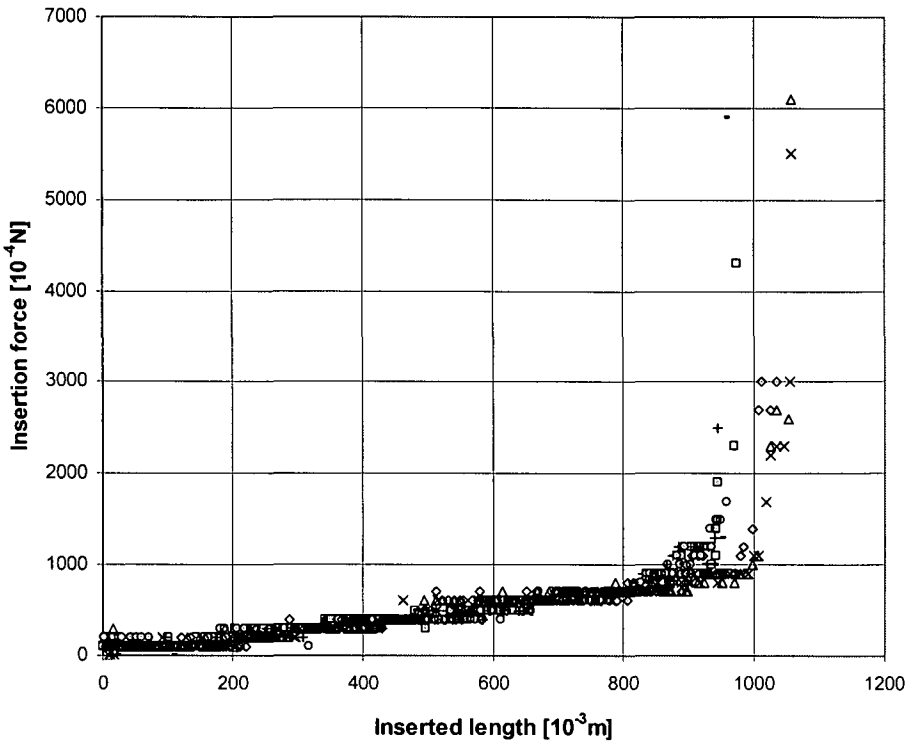

Figure 6.4.17 Plot of the insertion force versus the inserted length for $d = 3$ mm, $D = 33.4$ mm ($T = 14$ C).

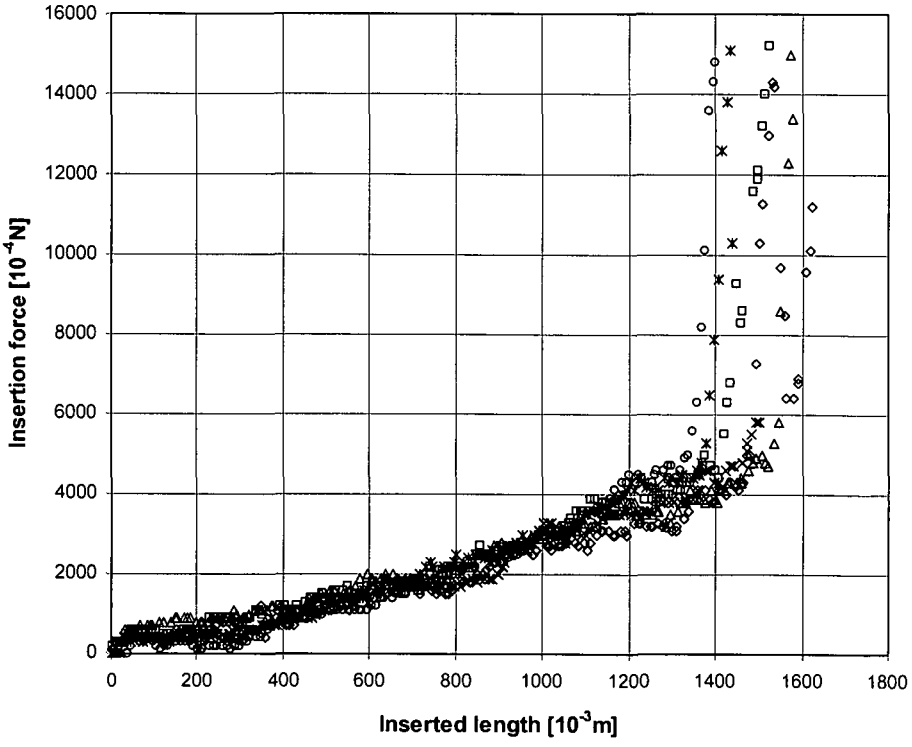

Figure 6.4.18 Plot of the insertion force versus the inserted length for $d = 5$ mm, $D = 33.4$ mm ($T = 17$ C).

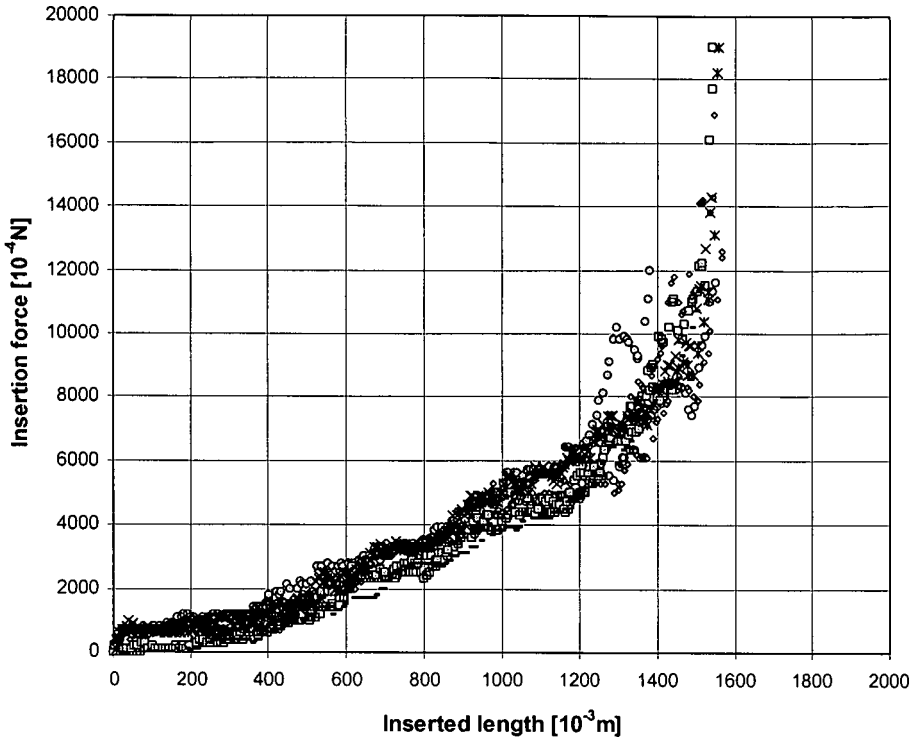

Figure 6.4.19 Plot of the insertion force versus the inserted length for $d = 6$ mm, $D = 33.4$ mm ($T = 20$ C).

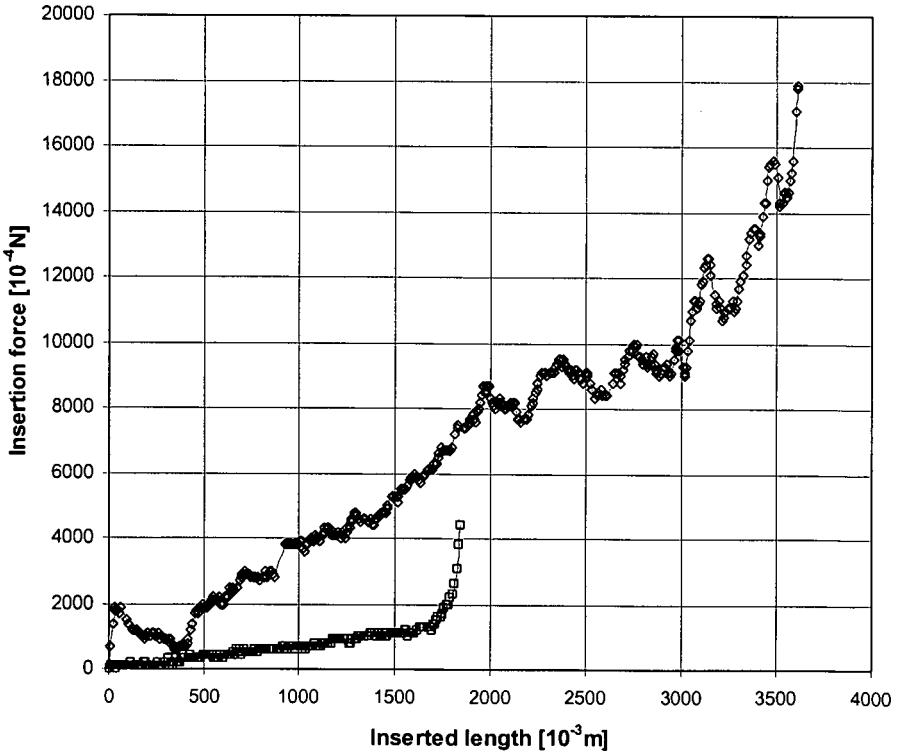

Figure 6.4.20 Plot of the insertion force versus the inserted length for $D = 13$ mm and $d = 3$ mm (□) and $d = 6$ mm (◇).

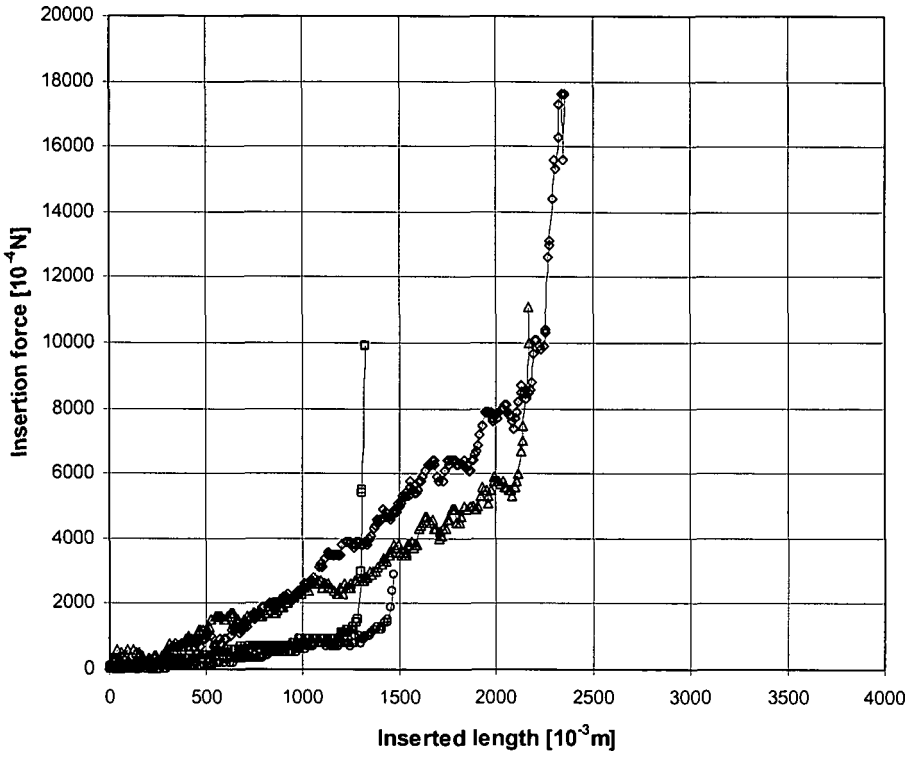

Figure 6.4.21 Plot of the insertion force versus the inserted length for D = 19 mm and d = 3 mm (□), d = 4 mm (○), d = 5 mm (Δ) and d = 6 mm (◇).

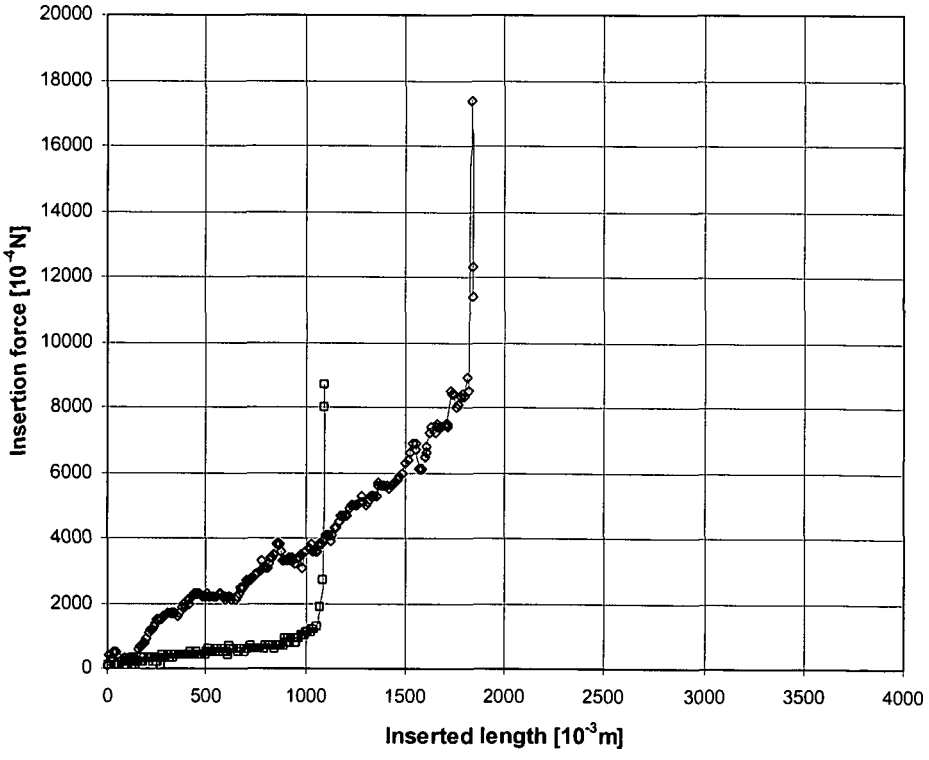

Figure 6.4.22 Plot of the insertion force versus the inserted length for D = 28.6 mm and d = 3 mm (□) and d = 6 mm (◇).

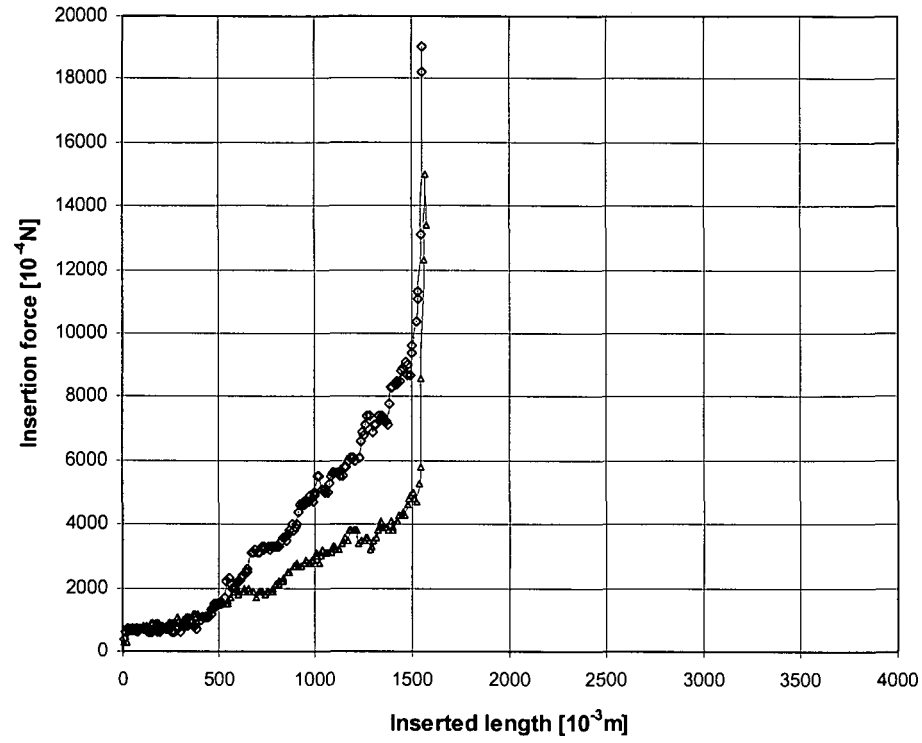

Figure 6.4.23 Plot of the insertion force versus the inserted length for $D = 33.4$ mm and $d = 5$ mm (◇) and $d = 6$ mm (Δ).

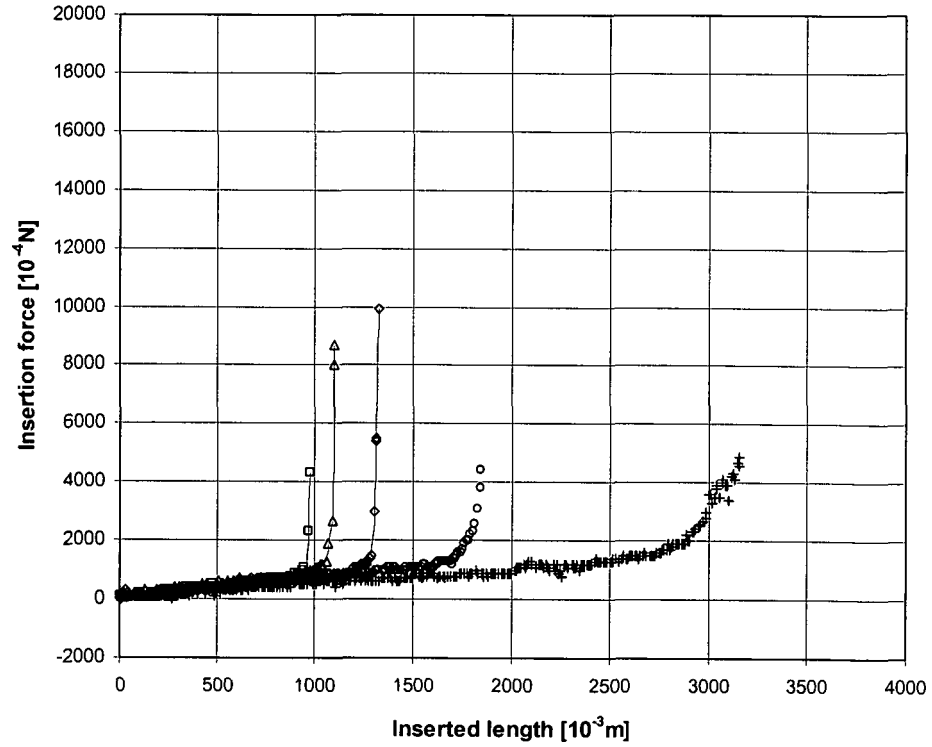

Figure 6.4.24 Plot of the insertion force versus the inserted length for $d = 3$ mm and $D = 33.4$ mm (□), $D = 28.6$ mm (Δ), $D = 19$ mm (◇), $D = 13$ mm (○) and $D = 8.6$ mm (+).

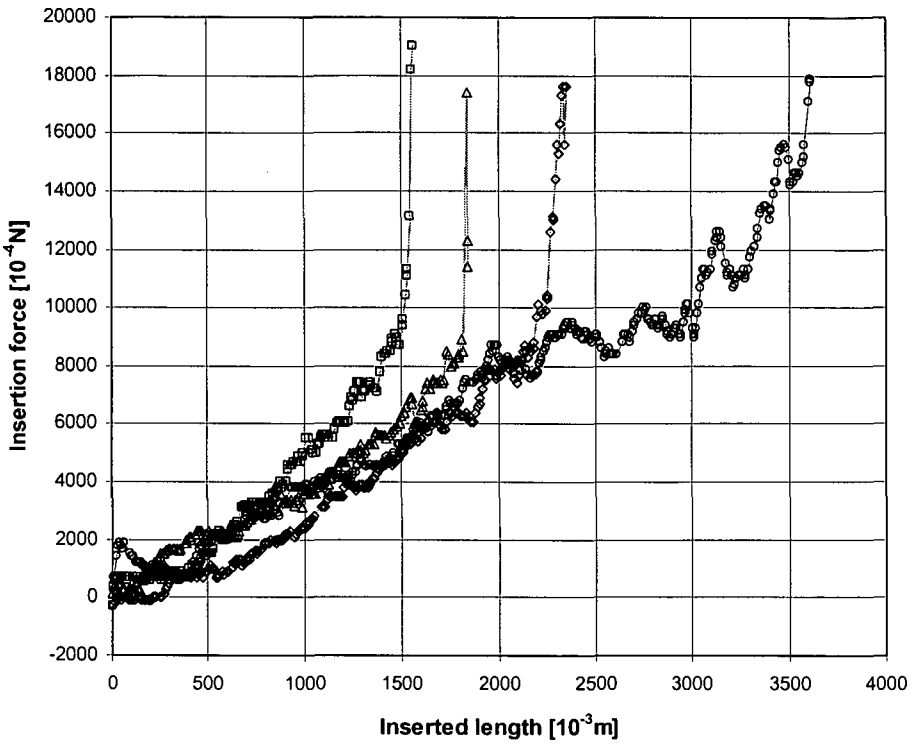

Figure 6.4.25 Plot of the insertion force versus the inserted length for d = 6 mm and D = 33.4 mm (□), D = 28.6 mm (Δ), D = 19 mm (◇) and D = 13 mm (○).

6.5 Summary of Experimental Work

All experimental results for the insertion of the rod into the constraining tubing demonstrate similar qualitative behaviour. The shape of the rod being inserted into the tube consists of three regions: the initial, apparently straight section, the subsequent section with sinusoidal deformations and the final section with helical deformations. The region with the fully developed helical deformations is relatively small, and is confined to about the last 10% to 20% of the inserted rod.

All the graphs for the variation of the insertion force with the inserted length indicate a clear trend. The insertion force initially increases linearly with the inserted length. This continues until a critical length is reached, at which the insertion force increases very rapidly. Even though all figures demonstrate some scatter and uncertainty, the critical length is reasonably well defined for all combinations of the rod and the containing cylinder diameter investigated in this work.

The graphs also indicate that for a constant diameter of the containing cylinder the critical insertion length increases with the diameter of the rod, and that for a constant diameter of the rod the critical insertion length decreases with the diameter of the containing cylinder.

6.6 Experimental Errors and Error Analysis

6.6.1 Experimental errors

The sources of errors in the experimental set-up can be identified as mechanical or electrical and errors arising from use of polymers. The mechanical and electrical errors arise from: (i) rod diameter, (ii) tube inside diameter, (iii) measurement of inserted length and (iv) force measurement. The errors associated with the use of the polymer are found from: (i) reaction between rod and tube, (ii) determination of modulus of elasticity, (iii) measurement of friction and (iv) ambient conditions.

The rod diameter was supplied from the manufacturer with a stated tolerance of ±0.1 mm, and the tolerances quoted were deemed to be satisfactory. Similarly, the tolerances of the tube inside diameter, as specified by the manufacturer, were also deemed satisfactory. Initially polymer tubes were used, but these were replaced because of the interaction between the polymer rod and tube.

Several aspects of the measurement of the inserted length are considered, since there are two approaches to the measurement of the inserted length. The first approach is to measure the axial inserted length of the rod directly by measuring the length of the inserted rod from the insertion point to the end of the rod at lock-up. This measurement is a purely mechanical measurement with an accuracy of ±1 mm. The second approach is to compare the digital output from the stepper motor with the actual inserted length achieved and incorporating the appropriate calibration factor in the software.

The end force is measured ultimately by a force transducer mounted at the insertion point. The accuracy of the force reading for the 10 N transducer is quoted by the manufacturer as ±0.1% of full scale. Inaccuracies will also arise from the efficacy with which the rod reacts

onto the transducer. Careful design of the air bearing system ensures that reaction friction forces are minimised, but it has been estimated that a friction force of considerably less than 0.01 N will exist. This leaves the force measurement accuracy of about ±0.1% of full scale, which is considered acceptable.

Early experiments showed that the axial insertion lengths were very variable and changed dependent on the insertion velocity. Further analysis identified that the cause of this was that both the rod and tube were polymers and the action of insertion at some velocity resulted in static electrical forces that effectively increased the friction factor. Changing the tubes material to glass solved this problem.

The determination of the modulus of elasticity was carefully considered. The first concern was that while normal methods of determining the Modulus relied on a tensile set-up, the coiled tube buckling problem was basically with the coiled tube in compression. While this would not present a problem for a steel coiled tube, it did need consideration when working with a polymer that might not have a linear load/extension relationship. A major factor in the determination of the E value was the amount of extension and compression. For tension strain of up to 3%, the stress/strain curve is linear and the modulus can be assumed to have the same value in tension and compression (M.R.P.A., 1974). Since it is estimated that the strain at the critical load for helical buckling (Lubinski, 1962) is about 1%, the linear behaviour can be assumed and the modulus of elasticity in tension can also be used in compression. The measurement of the modulus of elasticity was done by measuring the extension of a 1 m length of rod under masses. The masses were checked against a calibrated weighing device and the measurements made using instrumentation accurate to ±0.1 g. Tests were done at a measured temperature that corresponded to subsequent load tests.

Three methods were adopted for the measurement of friction: (i) inclined plane, (ii) measurement of the slope of the load/insertion line and (iii) measurement of the slope on the load/extraction line. The inclined plane was unwieldy to use and did not produce consistent results. The insertion line enabled spurious readings to be absorbed leaving a definite trend with good conformance, as did the extraction results. The errors on the insertion line arose from the extra friction effects brought about by the reactions between the rod and tube during insertion. Using the extraction line removed these problem so was thought to produce a more

representative value. The accuracy of the results obtained reflected the accuracy of the load cell and the length measurement.

Throughout the experimental phase, it was very clear that temperature played a very important role in the values obtained, specifically the values of E and the coefficient of friction. For this reason, the tests were done in a close temperature window so that the tests were comparable and able to be extrapolated. A second, perhaps a more important problem arose from the presence of dust and other contaminants in the tube. Again, experimental cleaning procedures ensured these were minimised.

6.6.2 Error analysis

Section 6.6.1 has outlined the errors that could arise during the experimental phase of the work. When the errors being considered were the result of measurements or the physical sizes of the components, then the errors would be small, being in the range 3-5%. However, the largest sources of errors were the operating temperature during testing and surface contamination, as wide swings produced significant variations in the values obtained. The values of the physical parameters varied between nominally identical tests, but remained within the prescribed tolerance.

7. Analytical Work

7.1 Scoping Model

The scoping model was developed during the early stages of the experimental work with the major purpose of identifying those parameters which needed to be studied experimentally.

The scoping model is highly simplified, neglecting helical buckling and introducing a simulated wall reaction force. Several assumptions used in the development of the scoping model are now known not to hold, nevertheless, the dimensionless groups derived from the model have been subsequently confirmed as significant by the full analysis developed later.

The scoping model, which has been already published (see Appendix A), is given for completeness, and briefly described below.

The major assumption in the development of the model is that only plane sinusoidal buckling is considered, with the helical buckling neglected. The major reasons for these simplifications are that: (i) the sinusoidal buckling always precedes the helical buckling (ii) the sinusoidal plane buckling is much better understood and can be incorporated more readily into the analytical model, and (iii) the purpose of the scoping analysis is to determine those factors which influence the penetration and to provide broad estimates of the penetration lengths.

The critical buckling force for sinusoidal buckling is given generally as

$$F_{CR} = \frac{k_1 EI}{L_B^2} \qquad (7.1.1)$$

where the buckling parameter k_1 is discussed later. The plan view of the first buckling form is indicated in figure 7.1.1.

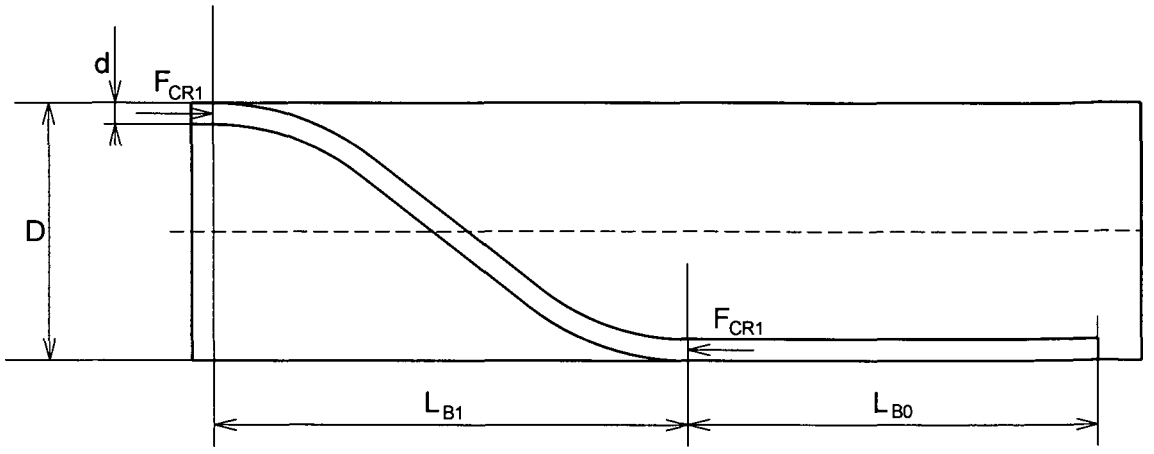

Figure 7.1.1 Diagram of the first buckling form.

It should be noted that even though the figure indicates that the first deformation of the rod is comparable to the diameter of the tube, the first few deformations are generally much smaller than the diameter. It is assumed in the model that the total friction force F_{CRI} between the rod and the wall of the tube over the length L_{B0} provides the critical force required to buckle the length of the rod L_{BI}. The friction force required to push a column L_{B0} long is given as

$$F_{CR1} = m_L L_{B0} g \mu \tag{7.1.2}$$

Equation (7.1.1) with F_{CRI} and L_{BI} and equation (7.1.2) can be combined and re-arranged in dimensionless forms as

$$\frac{\frac{F_{CR1}}{kEI}}{D^2} = \frac{L_{B0}}{D}\frac{m_L g \mu D^3}{kEI} \tag{7.1.3}$$

$$\frac{L_{B1}}{D} = \left(\frac{kEI}{m_l g \mu D^3}\frac{D}{L_{B0}}\right)^{1/2} \tag{7.1.4}$$

The buckling parameter depends on the boundary conditions. Because of the subsequent buckling shape, the back boundary condition of the first buckling shape can be considered as built-in. However, the front boundary condition is more difficult to specify. It is not free, since the initial straight section provides some restraining influence. Additionally, it is also not built in, since the front can move relatively freely. It seems that the most appropriate

front boundary condition for the first buckling shape is pinned. This implies that for the first buckling shape the buckling parameter is $k_1 = 2\pi^2$. It should be further noted that for the subsequent buckling shapes the boundary conditions at both ends can be considered as built-in. Since, as discussed later and as shown in figure 7.1.4, the analysis progresses in half-cycle intervals, the buckling parameter for all subsequent buckling shapes is $k_1 = \pi^2$.

As the amplitude of the sinusoidal buckling shape increases additional forces normal to the wall will be generated. These will occur after a certain transitional period, which is not necessarily known. For simplicity, such a situation is shown in figure 7.1.2 for the first buckling shape.

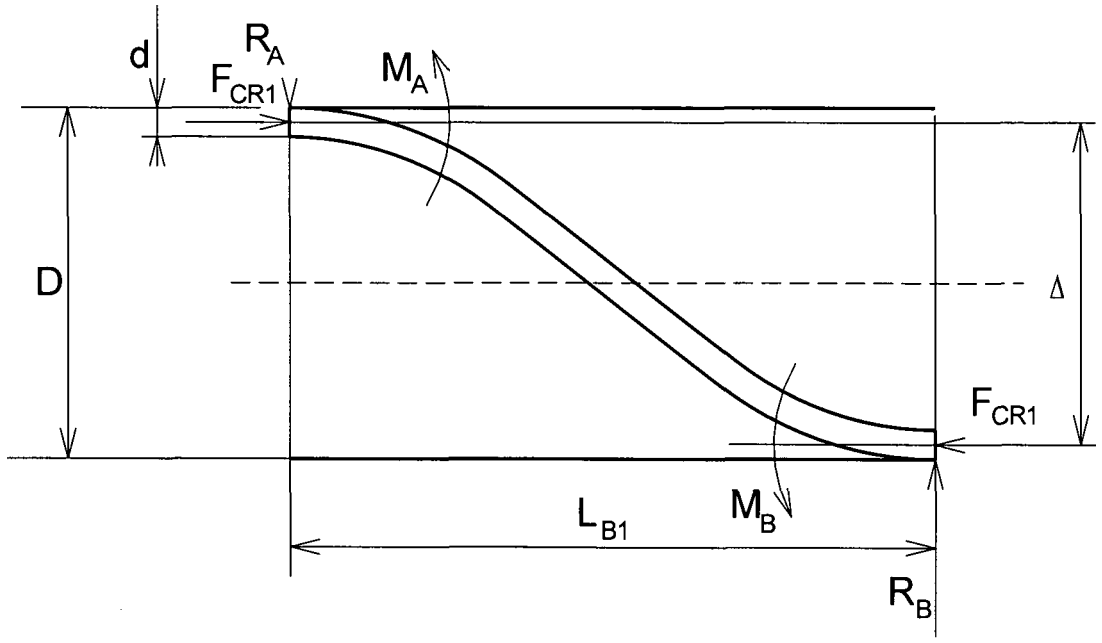

Figure 7.1.2 Diagram of the reaction forces.

It is assumed that a reaction force will develop between the rod and the wall of the containing cylinder. This reaction force is given by

$$R_A = R_B = R_1 \tag{7.1.5}$$

$$R_1 = F_{CR1}\frac{\Delta}{L_{B1}} \tag{7.1.6}$$

where

$$\frac{\Delta}{D} = 1 - \frac{d}{D} \tag{7.1.7}$$

It should be noted that this cannot obtain for the first buckling shape because it cannot support the moment M_B on element L_{B1}. However, the subsequent elements L_{B2}, L_{B3}, ... L_{BN} can support these moments. These reaction forces can only be considered when there is strong contact between the penetrating rod and the walls of the tube. However, since the normal forces are very small for the initial buckling shapes when the cycles are relatively long, the error introduced by considering these forces for all buckling shapes can be neglected.

Furthermore, additional frictional forces due to the mass of the tubular of length L_{B1}, as well as the reactions, must be added as the column continues to move.

Figure 7.1.3 shows that the resultant force F_{CR2} as

$$F_{CR2} = F_{CR1} + 2\mu R_1 + \mu W_{L_{B1}} \tag{7.1.8}$$

where the second term is the friction due to the two normal forces and the third term is the friction due to the weight of the column length L_{B1}. This can be further re-arranged as

$$\frac{F_{CR2}}{F_{CR1}} = 1 + 2\mu\left(1 - \frac{d}{D}\right)\frac{D}{L_{B1}} + \frac{\mu}{k}\frac{m_L g d^3}{EI}\left(\frac{D}{d}\right)^3\left(\frac{L_{B1}}{D}\right)^3 \tag{7.1.9}$$

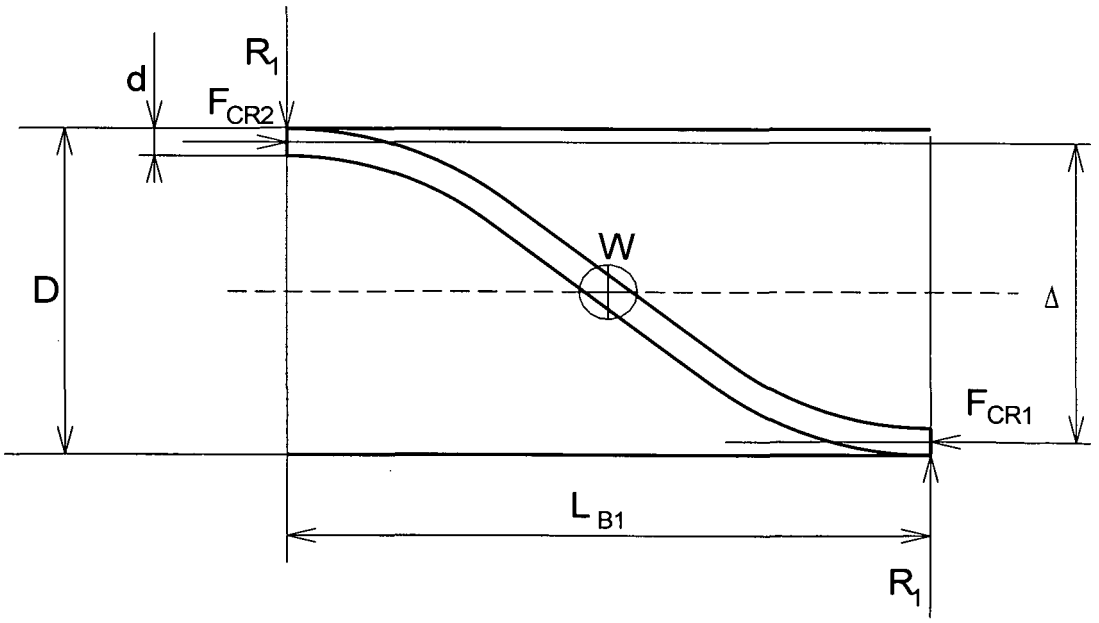

Figure 7.1.3 Force diagram on the first buckled element.

Figure 7.1.4 shows the next buckled shape, whose length can be expressed as

$$\frac{L_{B2}}{D} = \frac{L_{B1}}{D}\left(\frac{F_{CR2}}{F_{CR1}}\right)^{-1/2} \tag{7.1.10}$$

and where F_{CR2}/F_{CR1} is given by equation (7.1.9).

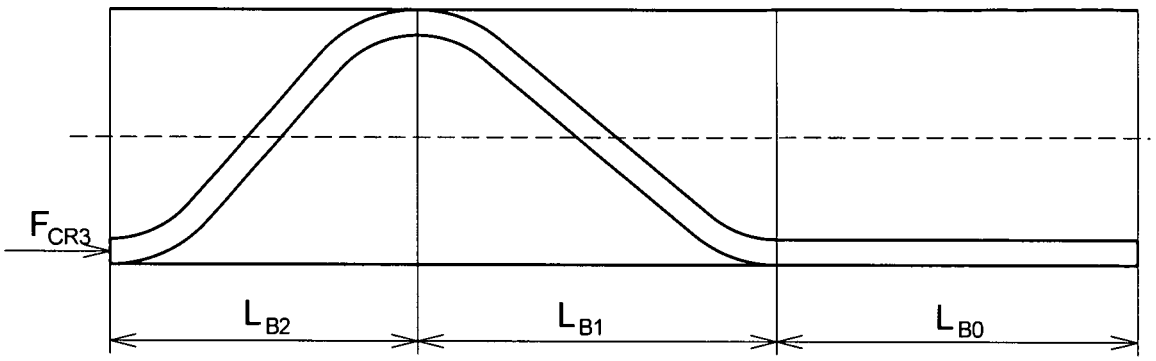

Figure 7.1.4 Diagram of the first two buckling forms.

The axial force F_{CR3} and the length L_{B3} can then be similarly calculated as

$$\frac{F_{CR3}}{F_{CR2}} = 1 + 2\mu\left(1 - \frac{d}{D}\right)\frac{D}{L_{B2}} + \frac{\mu}{k}\frac{m_L g d^3}{EI}\left(\frac{D}{d}\right)^3\left(\frac{L_{B2}}{D}\right)^3 \tag{7.1.11}$$

$$\frac{L_{B3}}{D} = \frac{L_{B2}}{D}\left(\frac{F_{CR3}}{F_{CR2}}\right)^{-1/2} \tag{7.1.12}$$

The above approach can be continued and all subsequent forces and lengths calculated. The total force acting on the tubular can then be obtained as

$$F = \frac{F_{CRN}}{F_{CR(N-1)}} \bullet\bullet\bullet \frac{F_{CR3}}{F_{CR2}}\frac{F_{CR2}}{F_{CR1}}F_{CR1} \tag{7.1.13}$$

and the total length of the deformed tubular as

$$\frac{L}{D} = \left(\frac{L_{B0}}{D} + \frac{L_{B1}}{D} + \frac{L_{B2}}{D} + \frac{L_{B3}}{D} + \bullet\bullet\bullet + \frac{L_{BN}}{D} \right) \tag{7.1.14}$$

The total length L when the tubular becomes fully locked will obtain when the total force F reaches F_{MAX}, the maximum force available.

The above analysis indicates that the penetration depends on the initial value of L_{B0} , F_{MAX} and the following dimensionless parameters:

$$\frac{m_L g d^3}{EI} \tag{7.1.15}$$

$$\mu \tag{7.1.16}$$

$$\frac{d}{D} \tag{7.1.17}$$

The first dimensionless group, $m_L g d^3/EI$, depends only on the geometry and the material properties of the tubular. The second dimensionless parameter, μ, is the friction factor between the tubular and the walls of the containing pipe. The last dimensionless group depends on the geometry of the system.

In order to calculate the penetration of the tubular, the three dimensionless groups, and L_{B0}/D and F_{MAX} must be specified. The three dimensionless groups are discussed above. The maximum force is determined primarily by the capacity of the pushing system, but also depends on the initial vertical drop of the oil well. The maximum penetration will then depend on the assumed initial value of L_{B0}/D.

The above results, including the reaction forces, are used to calculate recurrently $F_{CRN}/F_{CR(N-1)}$ and L_{BN}/D. Equations (7.1.13) and (7.1.14) are then used to determine the total force and the total penetration.

It can be shown that the length of penetration exhibits a minimum for a certain value of L_{B0} (and hence L_{B0}/D). It is possible to minimise the length of the whole penetration with respect to L_{B0}/D, but this is closely related to the minimum length of the first two half-cycles L_{01}. This is given from equations (7.1.4) and (7.1.14) as

$$\frac{L_{01}}{D} = \frac{L_{B0}}{D} + \left(\frac{kEI}{m_l g \mu D^3} \frac{D}{L_{B0}} \right)^{1/2} \tag{7.1.18}$$

which, differentiated with respect to L_{B0}/D, gives the minimum value for L_{B0}/D as

$$\frac{L_{B0}}{D} = \left(\frac{1}{2} \right)^{2/3} \left(\frac{\mu}{k} \frac{m_l g d^3}{EI} \right)^{-1/3} \frac{d}{D} \tag{7.1.19}$$

A comparison with experimental results suggests that it is the minimisation of the total penetration which gives the appropriate value of L_{B0}/D. It also shows that the appropriate value of L_{B0}/D is also a function of the three dimensionless groups discussed above.

The scoping model shows that the dimensionless penetration L/D depends on three dimensionless parameters $m_L g d^3/EI$, μ and d/D, as well as the initial value L_{B0}/D and the maximum axial force available F_{MAX}. Furthermore, the analysis shows that the penetration exhibits a broad minimum, which is not particularly sensitive to the choice of L_{B0}/D in the vicinity of L_{B0}/D given by equation (7.1.19). The minimum penetrations obtained from the scoping model are in reasonable agreement with the experimental data. This indicates that only the minimum penetration is probably achievable in practice. The most likely reason is that the rod is not straight when being inserted and that the initial rod deformations do not allow penetrations beyond the minimum, but further work is required.

Since the initial value of L_{B0}/D for the minimum deformation depends only on $m_L g d^3/EI$, μ and d/D, it can be concluded that the actual penetrations obtained depend only on these three dimensionless parameters, and the maximum axial force available F_{MAX}, which can be expressed in a dimensionless form as $F_{MAX}/(kEI/D^2)$. The parameter $m_L g d^3/EI$ is related to the flexural rigidity of the tubular, and the penetration will increase as the flexural rigidity

increases. Similarly, as the friction decreases the penetration will increase. The effect of the ratio *d/D* is complex. Further systematic work on the influence of all three dimensionless parameters is required.

The major limitation of the theoretical analysis is that, as discussed above, it does not consider the transition to helical buckling and that simple buckling analysis is used for large deformations. However, there are at least two reasons why this may not significantly affect the validity of the model. First, as pointed out above, the region of the deformed rod which exhibits helical buckling is relatively small. Second, the incorporation of the normal wall reaction forces in the development of the model does provide a mechanism which, similarly to the development of the helical buckling, increases considerably the force required for further insertion of the rod into the tube just before lock up is established.

7.2 New Model

7.2.1 Qualitative considerations

By simple visual observation of the phenomena being investigated it was possible to arrive at a qualitative description of what was occurring which is given below.

As the rod is inserted into the tube, there is initially a straight section, with increasing inserted length the rod starts to deflect into sine shaped wave forms, initially with low amplitude and long pitch lengths. With further insertion the amplitude of the waves increases and the pitch length decreases towards the insertion end.

The observed asymmetric buckling phenomenon occurs because the force which causes buckling arises from the friction between the rod and the tube and therefore increases as the inserted length increases. The larger force at the insertion end of the tube is able to cause the larger lateral amplitude and shorter pitch length which had been observed. This friction force in the sinusoidal buckling zone is the product of mass per unit length, inserted length, friction coefficient and gravity.

As the inserted length continues to increase the sine wave amplitude increases and pitch length decreases until the rod moves up the inner surface of the tube above half way and flips over into a partially formed helix. Further insertion increases the force developed and results in the rod being forced upwards to contact the top surface of the tube and form a fully developed helix. This transformation to fully developed helical buckling occurs over several cycles. When full helical buckling has been developed the insertion force rises dramatically and further insertion is not possible.

From observation of the buckling phenomena it was clear that the analysis of the problem would be made easier by breaking down buckling behaviour into the following parts.

i) Define the three distinct types of buckling

a) Sinusoidal

b) Transition to helical

c) Fully developed helical buckling

ii) Consider three steps for sinusoidal buckling to calculate lengths.

d) The first buckled shape where buckling is initiated by friction forces alone, no end force on this first section: L_1

e) Next sinusoidal buckled shape where buckling is initiated by friction forces, and an end force coming from the previous buckled shape: L_2

f) All further buckled shapes where buckling is initiated by friction forces and an end force, coming from the previous buckled shape: L_3, L_4, L_5, etc.

iii) Determine criteria for start of transition to helical buckling.

iv) Determine transition length to for fully developed helical buckling.

v) Determine force to produce lock up.

vi) Determine length of helical buckling.

7.2.2 Initial deformation fixed-free is 'equivalent' to a vertical column subject to deformation under its own weight

If one considers the end fixings of the rod in the tube at the first mode of buckling it is clear that for analytical purposes, the inserted end of the rod is free, and the position at the end of first mode buckling which is attached to the rest of the rod can be considered as fixed.

To begin the analysis process a method was needed to calculate the initial length of the first buckled shape.

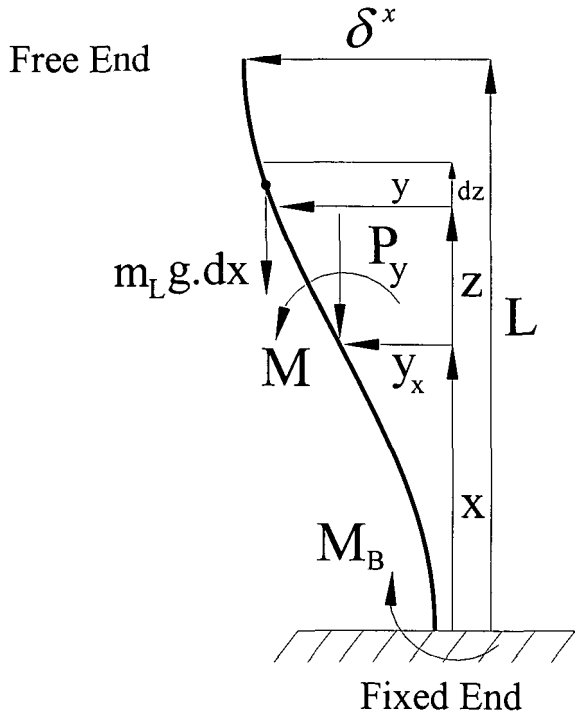

Figure 7.2.1 Vertical column fixed-free with own weight

An existing theoretical model (Timoshenko & Gere, 1961) which consisted of a free standing vertical column fixed at its lower end and free at its other end as shown in figure 7.2.1., was considered. A full analysis of this theoretical model is given in Appendix D. The deflection analysis and resulting moments were considered to be caused solely by the self mass of the rod. By considering the moments at a point x from the fixed end the differential equation below was obtained.

$$EI\frac{d^2y}{dx^2} + m_L g\, y(L-x) - m_L g \int_x^L y\,dz = 0 \qquad (7.2.1)$$

To eliminate dimensions let

$$\nu = \frac{y}{L} \qquad \therefore y = \nu L \tag{7.2.2}$$

$$\xi = \frac{x}{L} \qquad \therefore x = \xi L \tag{7.2.3}$$

$$\varphi = \frac{z}{L} \qquad \therefore z = \varphi L \tag{7.2.4}$$

By substituting these terms into equation (7.2.1) the following equation was obtained

$$\frac{d^2\nu}{d\xi^2} + \frac{m_L g \nu L^3}{EI}\nu(1-\xi) - \frac{m_L g L^3}{EI}\int_{\xi}^{1}\nu d\varphi = 0 \tag{7.2.5}$$

The above equation contains the non dimensional group

$$\frac{m_L g L^3}{EI} \tag{7.2.6}$$

This group contains the mass per unit length m_L, the length of the buckled section L, the elastic modulus E, the second moment of area I and the gravitational constant g.

Putting

$$K = \frac{m_L g L^3}{EI} \tag{7.2.7}$$

into equation (7.2.5) the following equation is obtained

$$\frac{d^2\nu}{d\xi^2} + K\nu(1-\xi) - K\int_{\xi}^{1}\nu d\varphi = 0 \tag{7.2.8}$$

Equation (7.2.8) is solved numerically to obtain the eigenvalues using a finite difference forward second order approximation within an Excel spreadsheet. For a twenty one step approximation $K = 7.83$, which was close to the theoretical case of $K = 7.836$ (Timoshenko & Gere, 1961).

Using the relationship in (7.2.7) the first mode buckled length L_1 can be solved as follows,

$$L_1 = K^{1/3}\left[\frac{EI}{m_L g}\right]^{1/3} = 1.99\left[\frac{EI}{m_L g}\right]^{1/3} \tag{7.2.9}$$

Similarly for second mode buckling

$$K_2 = \frac{m_L g(L_1 + L_2)^3}{EI} = 55.8 \qquad (7.2.10)$$

$$\therefore L_1 + L_2 = K^{1/3}\left[\frac{EI}{m_L g}\right]^{1/3} \qquad (7.2.11)$$

Hence

$$L_2 = 1.84\left[\frac{EI}{m_L g}\right]^{1/3} \qquad (7.2.12)$$

Complete solutions for L_1, L_2, are shown in Appendix E.

7.2.3 Investigation of fixed-free using axial force and own weight

The analysis below (figure 7.2.2) was used to give confidence in the analysis method used in the previous section. It confirms that when the end force is zero $K = 7.836$ and that when no self weight is considered the value for $B = \frac{PL^2}{EI} = \pi^2 / 4$ which is the same as that arrived at by other analysis methods (Madhukar, 2002).

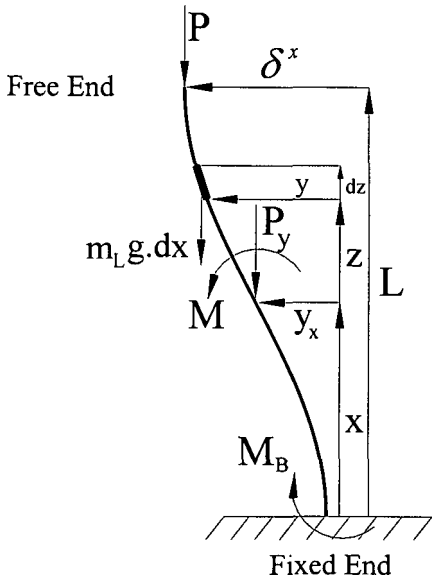

Figure 7.2.2 Vertical column fixed-free, own weight and axial force.

In the previous section the first mode buckling length was obtained. For the second mode buckling an axial force as well as self weight must be included in the analysis. The model used in the first mode was used again but in this case an axial force was applied at the free end. A full analysis of this theoretical model is given in Appendix F.

By considering the moments as in previous section for the vertical rod the differential equation below was obtained.

$$EI\frac{d^2y}{dx^2}+Py+m_Lg(L-x)y-P\delta^x-m_Lg\int_x^L ydx=0 \qquad (7.2.13)$$

This equation was non dimensionalised as in the previous section and the following obtained

$$\frac{d^2v}{d\xi^2}+\frac{PL^2}{EI}v+\frac{L^3m_Lg}{EI}v(1-\xi)-\frac{PL^2}{EI}\delta-\frac{L^3m_Lg}{EI}\int_\xi^1 vd\xi=0 \qquad (7.2.14)$$

The above equation contains two non dimensional groups

Putting $$K=\frac{m_LgL^3}{EI} \qquad (7.2.15)$$

and $$B=\frac{PL^2}{EI} \qquad (7.2.16)$$

gives

$$\frac{d^2v}{d\xi^2}+Bv+Kv(1-\xi)-B\delta-K\int_x^L vd\xi=0 \qquad (7.2.17)$$

Equation (7.2.17) is solved numerically to obtain the eigenvalues using a finite difference forward second order approximation within an Excel spreadsheet.

The dimensionless constant

$$K=\frac{m_LgL^3}{EI} \qquad (7.2.18)$$

is a measure of self weight

and $$B = \frac{PL^2}{EI} \tag{7.2.19}$$

is a measure of axial end force

With the constant B set to zero (zero axial force) it is then possible within the Excel spread sheet to use a goal seeking tool to set the determinant of the array to zero by selecting the appropriate value of K. This gave a result of $K = 7.832$ using a twenty one step approximation, which corresponds with a value of $K = 7.836$ derived by analytical means (Timoshenko and Gere, 1961).

By setting K to zero (effectively zero self weight) and using the goal seeking tool to set the determinant of the array to zero by selecting the appropriate value of B, gave a result of $B = 2.465$, which corresponds to the value of $\pi^2/4$ or 2.467 derived by analytical means (Madhukar, 2002).

7.2.4 Reaction forces during plane sinusoidal buckling

Consider figure 7.2.3, which shows the arrangements.

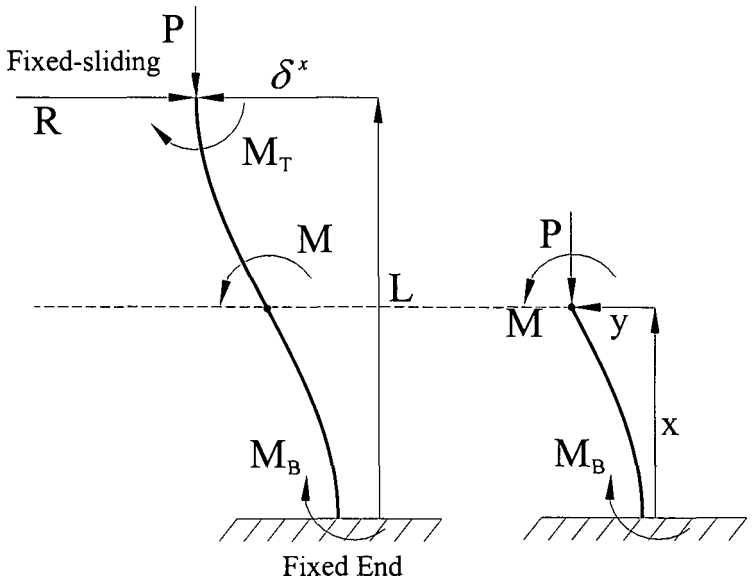

Figure 7.2.3 Vertical column with axial force and reaction force.

A full analysis of this section is given in Appendix G.

The governing equation is

$$EI\frac{d^2y}{dx^2} = M \tag{7.2.20}$$

The bending moment is given by

$$M = -Py + P\delta^* - R(L-x) - M_T \tag{7.2.21}$$

Hence after substituting equation (7.2.21) into equation (7.2.20) and further simplification results in

$$\frac{d^2y}{dx^2} + k_2 y = \frac{P}{EI}\delta^* - \frac{R}{EI}(L-x) - \frac{M_T}{EI} \tag{7.2.22}$$

where

$$k^2 = \frac{P}{EI} \tag{7.2.23}$$

The general solution of equation (7.2.22) is

$$y = y_H + y_P \tag{7.2.24}$$

Where y is the sum of the homogeneous solution y_H and the particular solution y_P

Substitute equation (7.2.24) into equation (7.2.22) as shown in Appendix G

$$y_H = C_1 \sin kx + C_2 \cos kx \tag{7.2.25}$$

and

$$y_P = \delta^* - \frac{R}{P}(L-x) - \frac{M_T}{P} \tag{7.2.26}$$

Hence

$$y = C_1 \sin(kx) + C_2 \cos(kx) + \delta^* - \frac{R}{P}(L-x) - \frac{M_T}{P} \tag{7.2.27}$$

and

$$\frac{dy}{dx} = C_1 k \cos(kx) - C_2 k \sin(kx) + \frac{R}{P} \tag{7.2.28}$$

Equation (7.2.27) contains four unknowns, C_1, C_2, R and M_T, and hence we need four boundary conditions. These are:

$$x = 0 \qquad y = 0 \tag{7.2.29}$$

$$x = 0 \qquad \frac{dy}{dx} = 0 \tag{7.2.30}$$

$$x = L \qquad y = \delta^* \tag{7.2.31}$$

$$x = L \qquad \frac{dy}{dx} = 0 \tag{7.2.32}$$

The four unknowns are calculated as shown in Appendix G as

$$C_1 = -\frac{R}{kP} \tag{7.2.33}$$

$$C_2 = \frac{R}{kP}\frac{1-\cos(kL)}{\sin(kL)} \tag{7.2.34}$$

$$\frac{M_T}{P} = \delta^* + \frac{R}{kP}\left(\frac{1-\cos(kL)}{\sin(kL)} - kl\right) \tag{7.2.35}$$

$$\frac{R}{P} = \frac{kL\sin(kL)}{2[\cos(kL)-1] + kL\sin(kL)}\frac{\delta^*}{L} \tag{7.2.36}$$

which can be re-written as

$$\frac{R}{P}\frac{L}{\delta^*} = \frac{kL\sin(kL)}{2[\cos(kL)-1]+kL\sin(kL)} \tag{7.2.37}$$

and the variation of $RL/P\delta^x$ as the function of kL can be obtained

Furthermore, it can be shown that the buckling occurs for

$$kL = \pi \tag{7.2.38}$$

and since

$$\sin\pi = 0 \tag{7.2.39}$$

equation (7.2.37) shows that when buckling occurs

$$R = 0 \tag{7.2.40}$$

Hence when buckling occurs, reaction R equals zero.

7.2.5 Use of the vertical buckling model in the horizontal penetration model

The vertical models described above for first and second mode buckling accurately define buckling for both of these modes. Simple modification of these models will allow their use in describing the behaviour of the rod in a horizontal position.

In the case of the vertical model the force causing buckling is gravitational acceleration and the mass of the rod: (mass per unit length * length) $m_L Lg$.

In the horizontal case the force which causes buckling is the friction force arising from movement of the rod in the tube. This is the product of the mass per unit length of the rod, friction coefficient between the rod and tube and the length of the buckled shape: $m_L L \mu g$.

Substituting the force arising from gravity g which causes the buckling in the vertical model with μg in the horizontal model will reflect the rod behaviour in the horizontal tube.

By using the extrapolation of the model defined in section 7.2.4 the number of cycles in the sinusoidal zone can be calculated as follows.

i) For the first cycle L_1, equation 7.2.9 from section 7.2.2.can be used.

ii) The same equation can be used for calculating the second cycle L_2.

7.2.6 Plane sinusoidal buckling development

Although the rod is being constrained in a cylinder the analysis is considering only plane sinusoidal buckling. i.e. buckling in two dimensions not three dimensions.

As there are no reaction forces which was proved in section 7.2.4, a model which describes third and higher modes of buckling is given by using a vertical column which has fixed – sliding, fixed ends with self weight and an axial force. This model describes accurately what is happening at the points between successive buckled cycles.

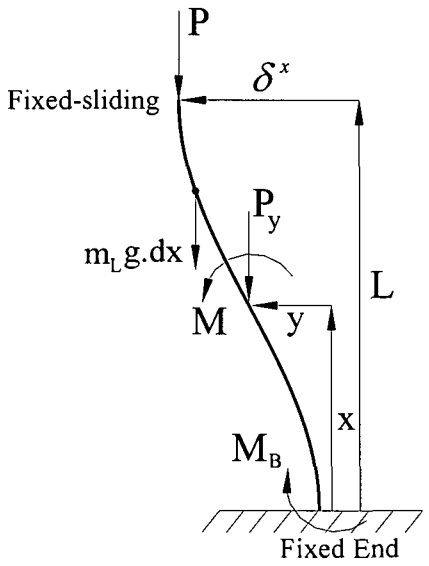

Figure 7.2.4 Vertical column fixed-fixed, sliding with own weight and axial force.

A full analysis of this theoretical model (figure 7.2.4) is given in Appendix H. By considering the moment at a distance x from the fixed end of the vertical rod the differential equation below was obtained.

$$EI\frac{d^2y}{dx^2} + Py + m_L g(L-x)y - P\delta^x - m_L g\int_x^L y\,dz + M_T = 0 \quad (7.2.41)$$

Convert M_T to dimensionless group by multiplying by $\frac{L}{EI}$, which gives

$$A = \frac{M_T L}{EI} \quad (7.2.42)$$

$$\frac{d^2v}{d\xi^2} + \frac{PL^2}{EI}v + \frac{L^3}{EI}m_L g v(1-\xi) - \frac{PL^2}{EI}\delta - \frac{L^3}{EI}m_L g\int_\xi^1 v\,d\xi + A = 0 \quad (7.2.43)$$

Non dimensionalise the other two groups as in section 7.2.3 gives

$$\frac{d^2v}{d\xi^2} + Bv + Kv(1-\xi) - B\delta - K\int_x^L v\,d\xi + A = 0 \quad (7.2.44)$$

$$\frac{d^2v}{d\xi^2} + Bv - B\delta + Kv(1-\xi) - K\int_x^L v\,d\xi + A = 0 \qquad (7.2.45)$$

This equation was solved numerically.

The dimensionless constants above represent the following

$$K = \frac{m_L g L^3}{EI} \qquad (7.2.46)$$

is a measure the self weight

$$B = \frac{PL^2}{EI} \qquad (7.2.47)$$

is a measure of the axial end force

$$A = \frac{M_T L}{EI} \qquad (7.2.48)$$

is a measure of the moment at the fixed-sliding end

By setting B to zero (effectively zero axial force) and using the goal seek tool to set the determinant of the array to zero by selecting the appropriate value of K gave a result of $K = 18.95$. This is corresponds to the value derived by analytical means. By setting K to zero (effectively zero self weight) and using goal seek tool setting the determinant of the array to zero by selecting the appropriate value of B gave a result of $B = 9.85$. This corresponds to the value of π^2 or 9.87 derived by analytical means for a column with the same defined end conditions (Madhukar, 2002).

The above numerical solution confirmed the validity of the analysis.

Algebraic manipulation of the dimensionless groups representing K and B, resulted in the following two relationships.

$$B = \frac{PL^2}{EI} \qquad (7.2.49)$$

$$\frac{B^3}{K^2} = \frac{P^3}{(m_L g)^2 EI} \tag{7.2.50}$$

If a graph of B versus B^3/K^2 is plotted, L can be obtained as shown in figure 7.2.5.

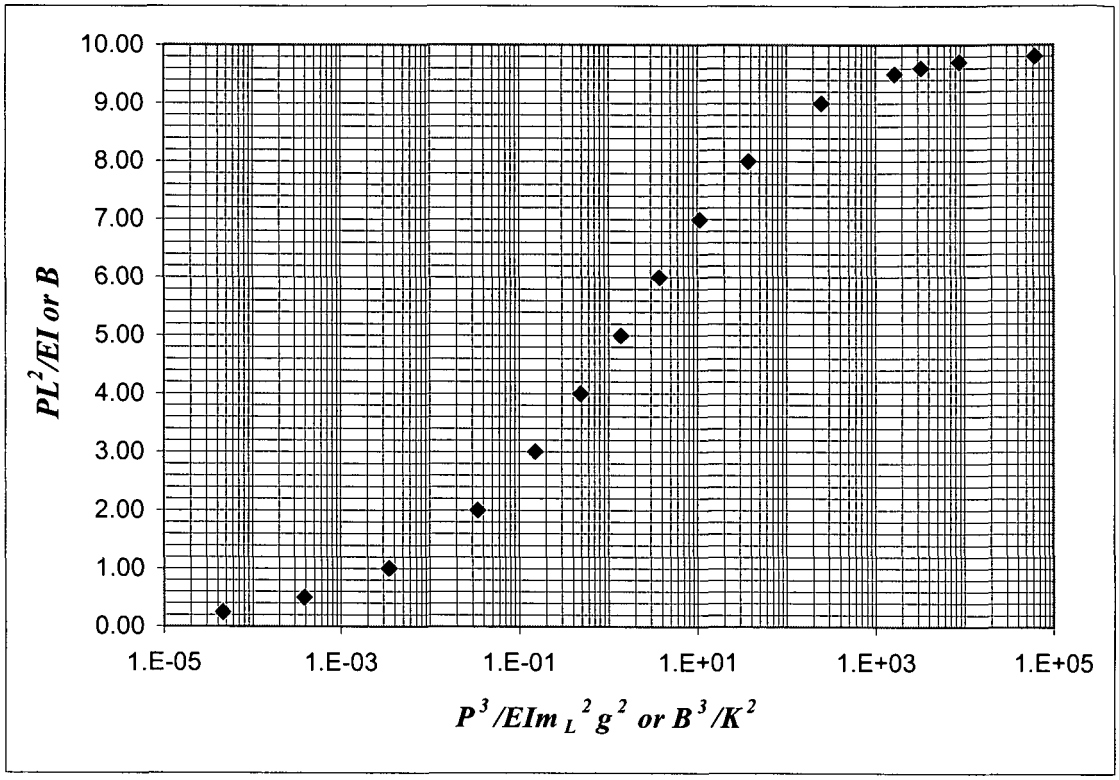

Figure 7.2.5: $\frac{PL^2}{EI}$ versus $\frac{P^3}{EI(m_L^2 g^2)}$ for all values.

Hence for a given $\frac{P^3}{EI(m_L g^2)}$, L can be calculated.

If one considers that the first buckled form is due to its own weight only, this results in

$$\frac{m_L g L_1^2}{EI} = 7.83 \tag{7.2.51}$$

as shown previously, hence the equivalent axial force on the first fixed-sliding member can be shown by further algebraic manipulation to be.

$$P = m_L g L_1 \Rightarrow \qquad P^3 = m_L^3 g^3 L_1^3 \Rightarrow$$

$$\frac{P^3}{m_L{}^2 g^2} = m_L g L_1{}^3 \Rightarrow \frac{P^3}{m_L{}^2 g^2 EI} = \frac{m_L g L_1{}^3}{EI} = 7.83 \tag{7.2.52}$$

The axial force on the subsequent members will be greater

$$\frac{P^3}{EI\left(m_L^2 g^2\right)} \geq 7.83 \tag{7.2.53}$$

But

$$\frac{B^3}{K^2} = \frac{P^3}{EI\left(m_L^2 g^2\right)} \tag{7.2.54}$$

$$\therefore \frac{B^3}{K^2} \geq 7.83 \tag{7.2.55}$$

The relationship between $\frac{P^3}{EI\left(m_L^2 g^2\right)}$ and B is shown on the graph in figure 7.2.6.

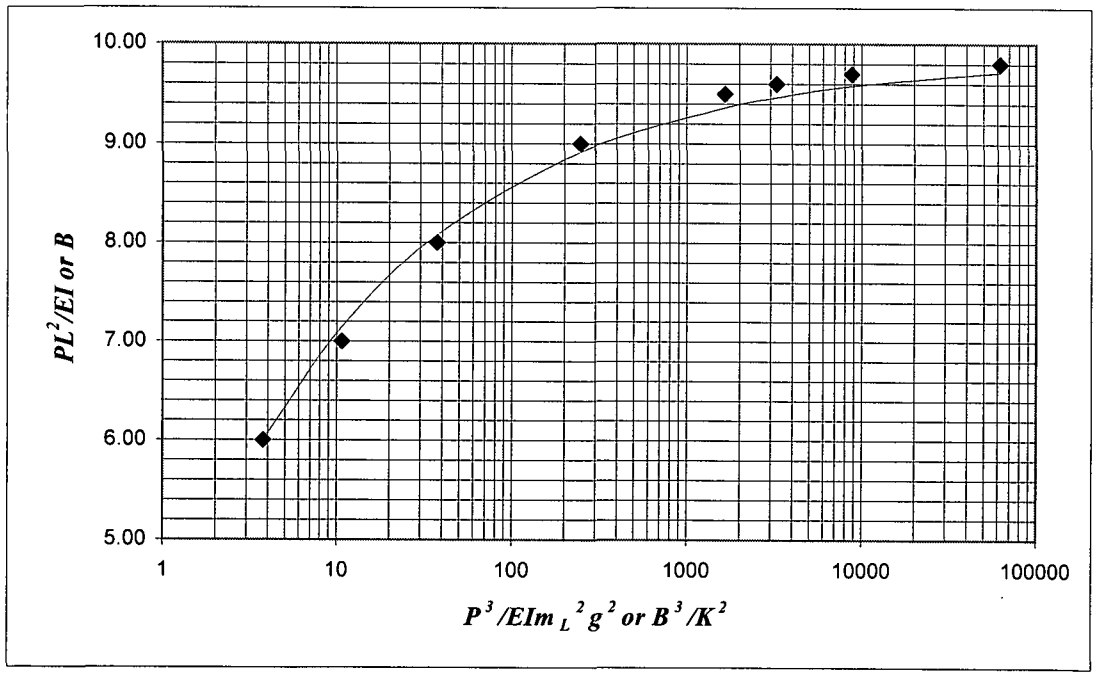

Figure 7.2.6: $\frac{PL^2}{EI}$ versus $\frac{P^3}{EI\left(m_L{}^2 g^2\right)}$ for values $\geq$ 7.83

For $\frac{P^3}{EI\left(m_L g^2\right)} \geq 7.83$ this can be approximated by using a standard curve fit technique with an error less than 2% as

$$\frac{PL^2}{EI} = \pi^2 - 6\left[\frac{EI\left(m_L g\right)^2}{P^3}\right]^{\left(\frac{1}{3}\right)} \tag{7.2.56}$$

This is demonstrated by the solid line in figure 7.2.6.

Hence $$L = \pi\left(\frac{EI}{P}\right)^{1/2}\left[1 - \frac{6}{\pi^2}\left[\frac{EI\left(m_L g\right)^2}{P^3}\right]^{1/3}\right]^{1/6} \tag{7.2.57}$$

Similarly for the second form

$$\frac{m_L g L_1^{\,3}}{EI} = 55.83 \tag{7.2.58}$$

$$P^3 = m_L^{\,3} g^3 L_1^{\,3} \tag{7.2.59}$$

$$\frac{P^3}{\left(m_L g\right)^2 EI} \Rightarrow \frac{P^3}{m_L^{\,2} g^2 EI} \geq 55.83 \tag{7.2.60}$$

$$\frac{P^3}{m_L^{\,2} g^2 EI} = \frac{m_L g L_1^{\,3}}{EI} = 55.83\,\frac{B^3}{K^2} \geq 55.83 \tag{7.2.61}$$

Similarly for the third form $$\frac{P^3}{m_L^{\,2} g^2 EI} \geq 147.39 \tag{7.2.62}$$

Hence the lengths of successive buckling cycles can be calculated along with the forces to that point.

As proven previously in section 7.2.4 there are no reaction forces present during sinusoidal buckling, therefore the force required to cause sinusoidal buckling is given by:

$$P_S = m_L \mu g L \tag{7.2.63}$$

7.2.7 Critical force for the inception of helical buckling

The investigation being carried out looked at what happens throughout the complete cycle of events from initial insertion of the rod through sinusoidal buckling to helical buckling and lock up. For the analysis to proceed, a criterion was necessary to establish when buckling changed from sinusoidal to helical buckling. Work carried out by (Chen *et al*, 1990) had looked at buckling of tubulars in horizontal oil wells and had by analytical methods, derived the equation below which gives the critical force for the onset of helical buckling.

$$P_{cr} = 2^{1.5}\left(\frac{EIgm_L}{0.5(D-d)}\right)^{1/2} \tag{7.2.64}$$

This equation was in agreement with published work of (Lubinski, 1962). (Chen *et al*, 1990) also confirmed this analytical work experimentally by means of a 3 mm diameter aluminium rod locked in a transparent cylinder 2.4 metres long.

The forces which cause the onset of helical buckling are the summation of forces arising from all the sinusoidal buckled shapes. These forces are caused by friction only, no reaction forces are present.

7.2.8 Helical deformation

The axial force seen by the rod as it is inserted into the tube force is generated predominately by the normal reaction forces between the rod and the tube.

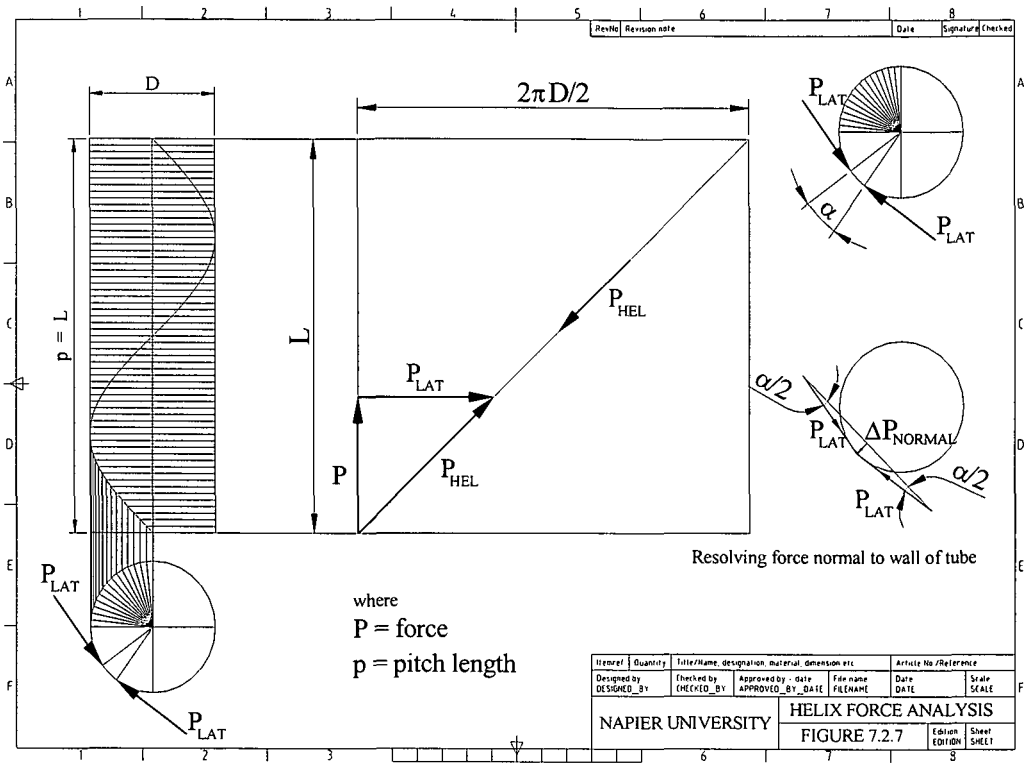

Figure 7.2.7 Helix force analysis

From analysis of the forces shown in figure 7.2.7 it can be shown that the total radial force on the inside surface of the tube is

$$P_{NORMAL} = 2\pi^2 \frac{D}{p} P \qquad (7.2.65)$$

A full analysis is given in Appendix I.

However perfect helical buckled shapes will not happen instantaneously. It must be assumed that several cycles will be required for the rod being deformed from start of transition to a fully formed helical shape as defined below, although other assumptions could be made.

1st transition cycle

$$P_{NORMAL} = 2\frac{D}{p} P \qquad (7.2.66)$$

2nd transition cycle $$P_{NORMAL} = 5\frac{D}{p}P \quad (7.2.67)$$

3rd transition cycle $$P_{NORMAL} = 10\frac{D}{p}P \quad (7.2.68)$$

Subsequent helical cycles $$P_{NORMAL} = 2\pi^2\frac{D}{p}P \quad (7.2.69)$$

7.2.9 Incorporation of sinusoidal and helical buckling into the model

The total inserted length is made up from the sum of the sinusoidally buckled section, the transition section where buckling is changing from sinusoidal to helical and the section where fully developed helical buckling occurs. Sinusoidal buckling section is broken into first mode buckling L_1, second mode buckling L_2 and subsequent buckling modes $L_3, L_4 etc$. The lengths and forces in this sinusoidal zone are calculated by methods shown in section 7.2.1 for L_1 and L_2, and section 7.2.6 for L_3, L_4 etc. Transition from sinusoidal to fully developed helical buckling is observed in the model to take place over approximately four cycles. This change is reflected by the almost parabolic section of the force/distance graph between the linear sinusoidal part and the almost exponential helical part.

In fully developed helical buckling, the rod is forced against the inner surface of the tube and large reaction forces are developed. These reaction forces, combined with friction, generate large axial forces which quickly cause lock up of the rod in the tube.

The lengths and forces in the transition to helical and fully developed helical buckling zones are calculated by methods shown in section 7.2.8.

7.2.10 Development of the Excel model

The object of this investigation is to calculate the inserted length of the rod into the tube and the forces generated whilst this taking place. The process is described briefly below.

As the rod is inserted buckling starts as sinusoidal and when a minimum force is reached it begins to change to helical buckling. The transition to fully developed helical buckling takes place over several cycles. After helical buckling occurs the force rises rapidly and the rod locks up in the tube with no further insertion possible.

Taking account of this, the model calculates the first and second buckled lengths as defined in section 7.2.1. All further sinusoidal buckled lengths are calculated as defined in section 7.2.6. In sinusoidal buckling there are no reaction forces present, therefore the insertion forces are calculated based on inserted length and friction.

The process of calculating lengths and forces, and summing them continues until the total force equals that as defined by (Chen *et al*, 1990) as the minimum to cause the onset of helical buckling. The lengths and forces for the transition segment and fully developed helical segment are calculated as defined in section 7.2.8.
In fully developed helical buckling the force rises very steeply and an arbitrary high value is set to ensure that the rod has fully locked up.

Overview of calculation of length of buckled shapes and forces

Sinusoidally buckled zone

Length of buckled shapes in this zone are given by

$$L_1 = 1.99\left[\frac{EI}{m_L g}\right]^{1/3} \qquad (7.2.9)$$

$$L_2 = 1.84\left[\frac{EI}{m_L g}\right]^{1/3} \qquad (7.2.12)$$

$$L_{N>2} = \pi\left(\frac{EI}{P}\right)^{1/2}\left[1-\frac{6}{\pi^2}\left[\frac{EI(m_L g)^2}{P^3}\right]^{1/3}\right]^{1/6} \tag{7.2.57}$$

As there are no reaction forces in the sinusoidal buckling zone the forces for each buckled shape in this zone are given by

$$F_S = m_L \mu g L \tag{7.2.63}$$

Transition zone

If the force given by equation 7.2.63 exceeds that given by

$$P_{cr} = 2^{1.5}\left(\frac{EIgm_L}{0.5(D-d)}\right)^{1/2} \tag{7.2.64}$$

the rod has started to transition from sinusoidal to helical buckling. Transition to fully developed helical buckling is estimated to take place over four cycles. The length of the buckled shapes in this zone are given in Appendix J

$$L_N = 2^{1.5}\pi\left(\frac{EI}{P_{N-1}}\right)^{1/2} \tag{J.9}$$

The forces for each of the four buckled shapes in this zone are given by

$$P_N = P_{N-1}\left(1+2\pi^2\frac{1}{2^{4-\min(flag,4)}}\mu\frac{D-d}{L_N}\right) \tag{J.12}$$

Fully developed helical buckled zone

The length of the buckled shapes in this zone are again given by

$$L_N = 2^{1.5}\pi\left(\frac{EI}{P_{N-1}}\right)^{1/2} \tag{J.9}$$

The forces for each buckled shape in this zone are given by

$$P_N = P_{N-1}\left(1+2\pi^2\mu\frac{D-d}{L_N}\right) \tag{A.J.12}$$

7.2.11 Demonstration of the Excel model

The model is demonstrated for a typical configuration ($d = 3$ mm, $D = 13$ mm and $\mu = 0.8$) in Figure 7.2.8.

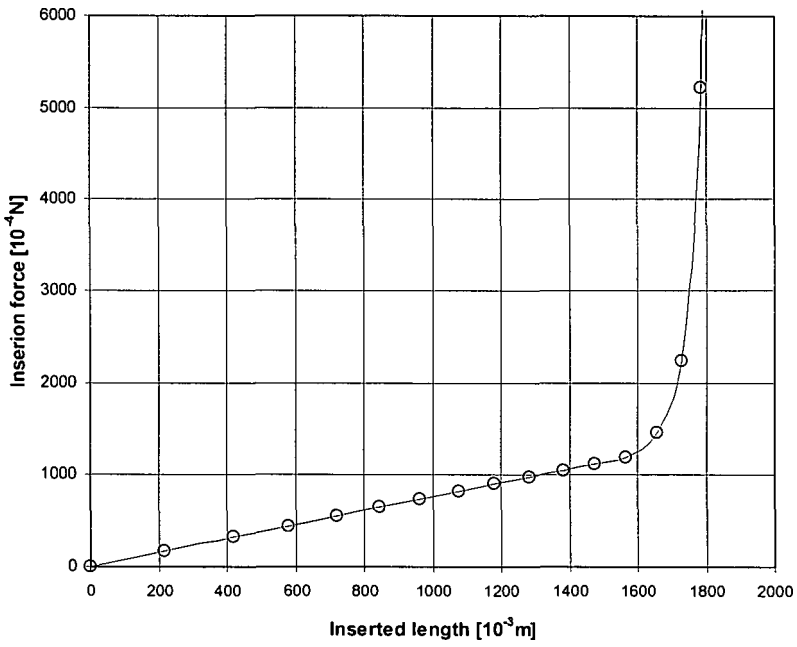

Figure 7.2.8 Theoretical results for the insertion force versus the inserted length for $d = 3$ mm, $D = 13$ mm and $\mu = 0.8$

The figure demonstrates the following features:

- transition to helical starts at about 1600 mm
- insertion force a linear function of inserted length before transition
- rapid increase of insertion force after transition
- maximum insertion about 1850 mm
- circles denote the length of individual buckled shapes
- the length of the first buckled shape (at the leading edge) about 220 mm
- the length of the second buckled shape about 200 mm
- the length of the third buckled shape about 160 mm

8. Comparison of Theoretical Results with Experimental Data

8.1 Comparison of theoretical result with experimental data for the rod deformation

The theoretical results obtained from the model developed in this work are compared with a sample of the experimental results presented in Table 6.3.1. The theoretical results were obtained using the model with the friction factor chosen in such a way so that the theoretically calculated maximum inserted length equal to the experimentally obtained maximum inserted length. The comparison is shown in Table 8.1.1.

rod diameter d [mm]	tube diameter D [mm]	maximum inserted length [mm]	number of sinusoidal cycles		number of helical cycles	
			experimental	theoretical	experimental	theoretical
3	15	1600	~10	10 to 11	~2	2 to 3
3	22.8	1000	~7	5 to 6	~2	2 to 3
3	33.4	950	~5	4 to 5	~1	2 to 3

Figure 8.1.1 Table giving description of rod deformation.

8.2 Comparison of Theoretical Result with Experimental Data for Insertion Tests

The theoretical results obtained from the model developed in this work are compared with the experimental data presented in Section 6.4. The experimental results are shown in grey and the theoretical results in black. Each figure contains at least two sets of theoretical results, which are obtained for different values of the friction factor.

The comparison for $D = 8.6$ mm and $d = 3$ mm is shown in Figure 8.2.1. The comparisons for $D = 13$ mm, and $d = 3$ mm and $d = 6$ mm are shown in Figures 8.2.2 and 8.2.3 respectively. The comparisons for $D = 15$ mm, and $d = 3$ mm, $d = 4$ mm, $d = 5$ mm and $d = 6$ mm are shown in Figures 8.2.4, 8.2.5, 8.2.6 and 8.2.7 respectively. The comparisons for $D = 19$ mm, and $d = 3$ mm, $d = 4$ mm, $d = 5$ mm and $d = 6$ mm are shown in Figures 8.2.8, 8.2.9, 8.2.10

and 8.2.11 respectively. The comparisons for D = 22.8 mm, and d = 3 mm, d = 5 mm and d = 6 mm are shown in Figures 8.2.12, 8.2.13 and 8.2.14 respectively. The comparisons for D = 28.6 mm, and d = 3 mm and d = 6 mm are shown in Figures 8.2.15 and 8.2.16 respectively. The comparisons for D = 33.4 mm, and d = 3 mm, d = 5 mm and d = 6 mm are shown in Figures 8.2.17, 8.2.18 and 8.2.19 respectively.

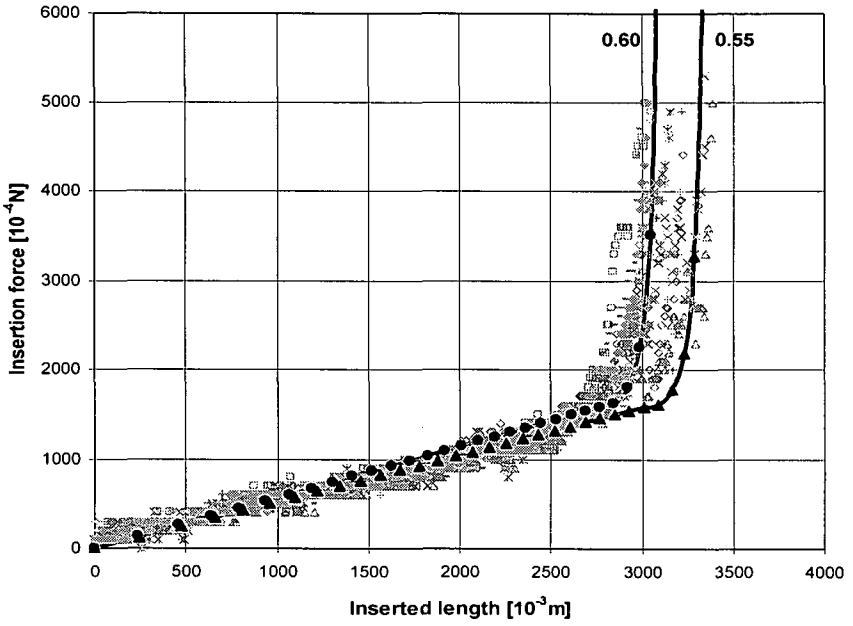

Figure 8.2.1 A comparison of the theoretical results for μ = 0.6 (●) and μ = 0.55 (▲) with the experimental data (grey symbols) for d = 3 mm and D = 8.6 mm.

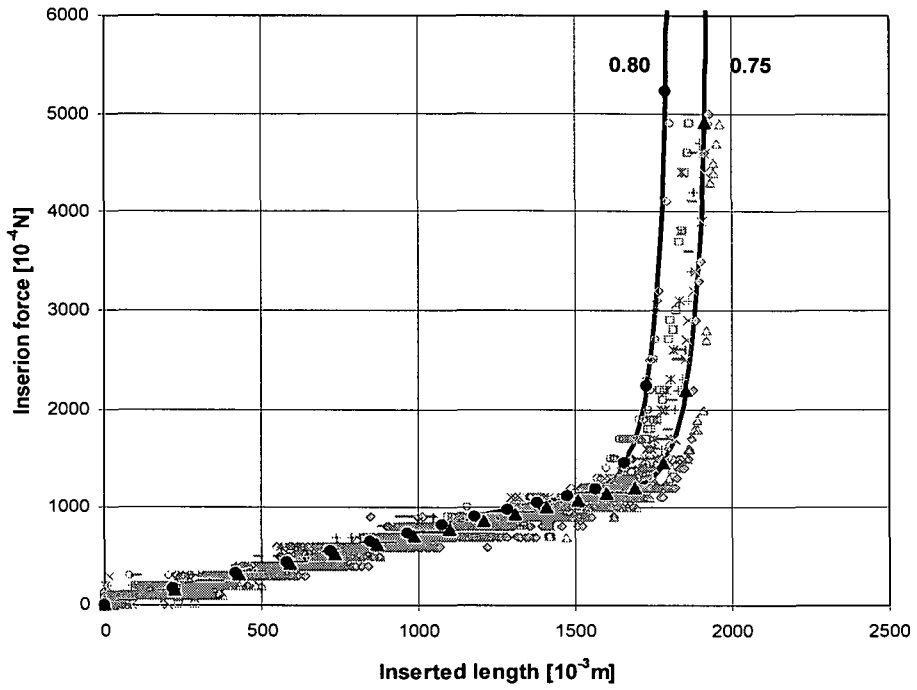

Figure 8.2.2 A comparison of the theoretical results for μ = 0.80 (●) and μ = 0.75 (▲) with the experimental data (grey symbols) for d = 3 mm and D = 13 mm

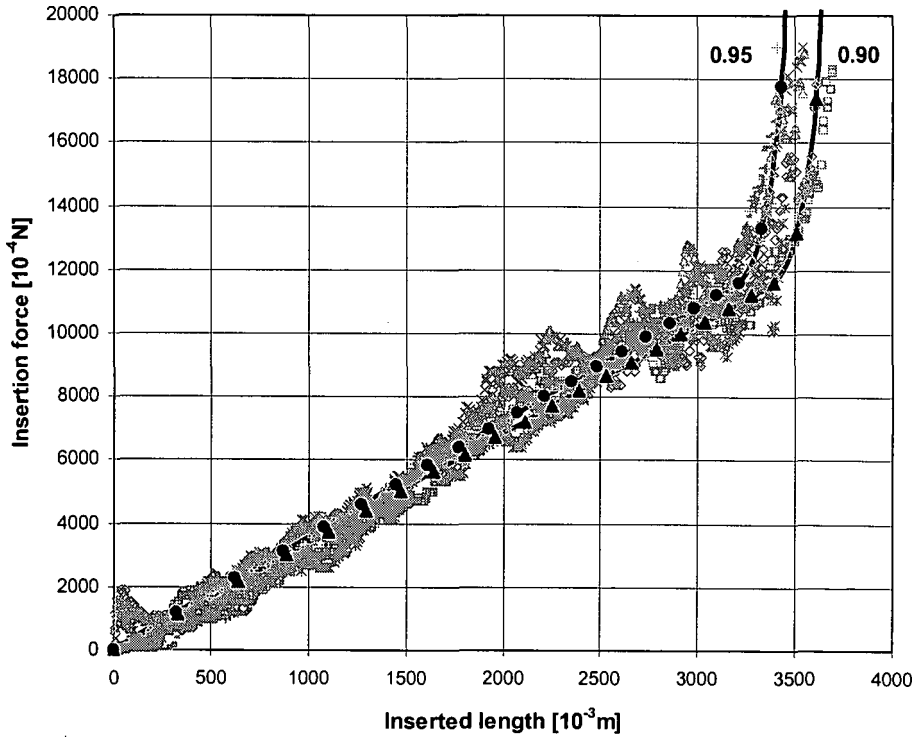

Figure 8.2.3 A comparison of the theoretical results for μ = 0.95 (●) and μ = 0.90 (▲) with the experimental data (grey symbols) for d = 6 mm and D = 13 mm.

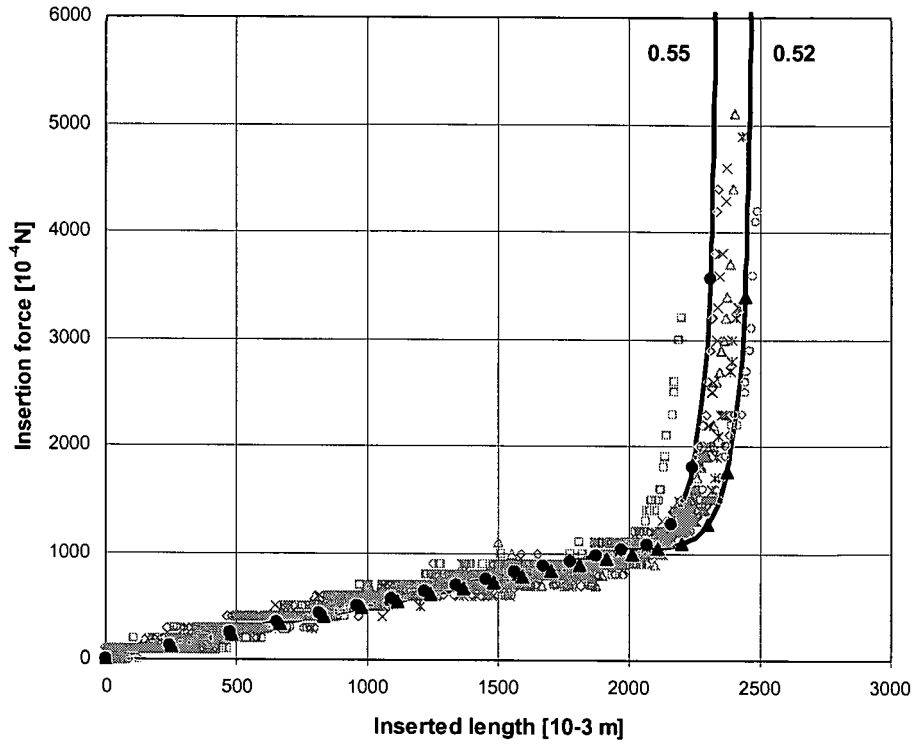

Figure 8.2.4 A comparison of the theoretical results for $\mu = 0.55$ (●) and $\mu = 0.52$ (▲) with the experimental data (grey symbols) for $d = 3$ mm and $D = 15$ mm.

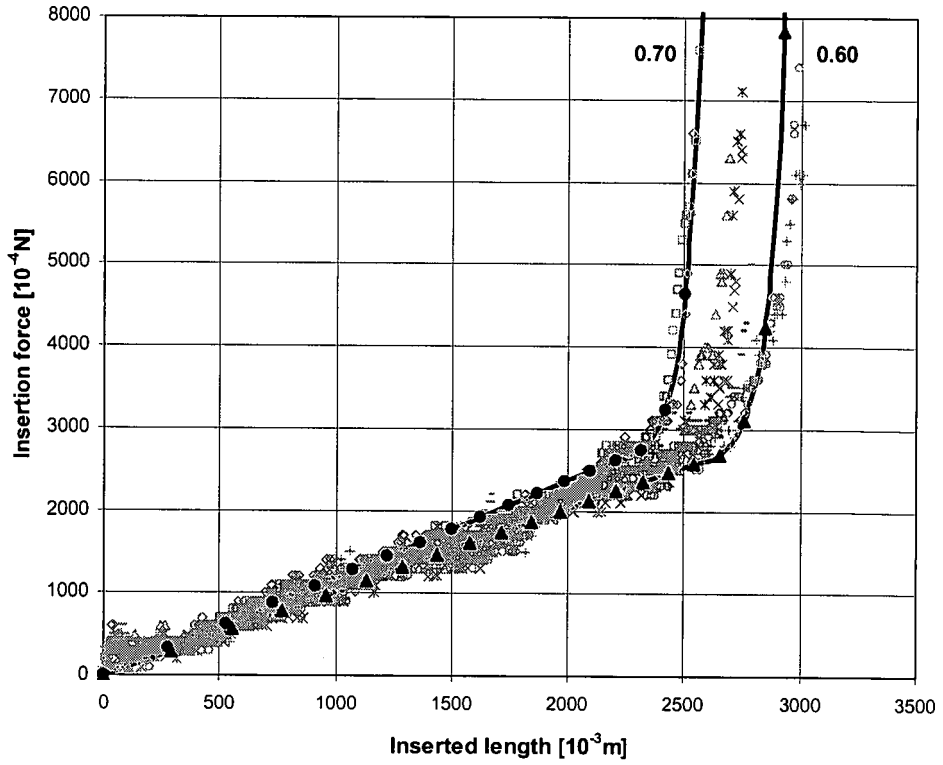

Figure 8.2.5 A comparison of the theoretical results for $\mu = 0.70$ (●) and $\mu = 0.60$ (▲) with the experimental data (grey symbols) for $d = 4$ mm and $D = 15$ mm.

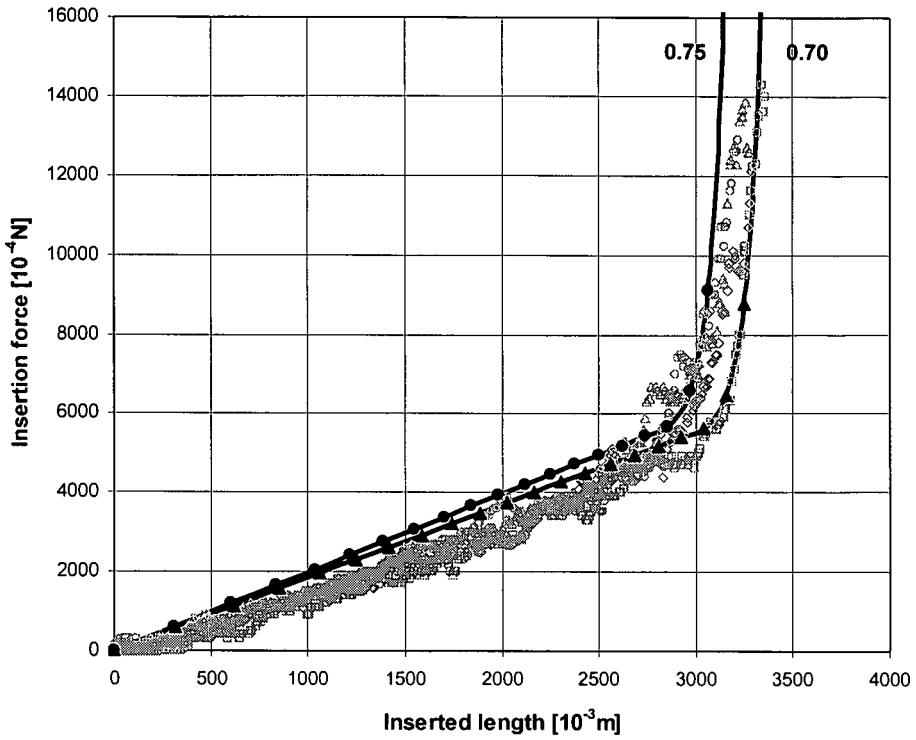

Figure 8.2.6 A comparison of the theoretical results for $\mu = 0.75$ (●) and $\mu = 0.70$ (▲) with the experimental data (grey symbols) for $d = 5$ mm and $D = 15$ mm.

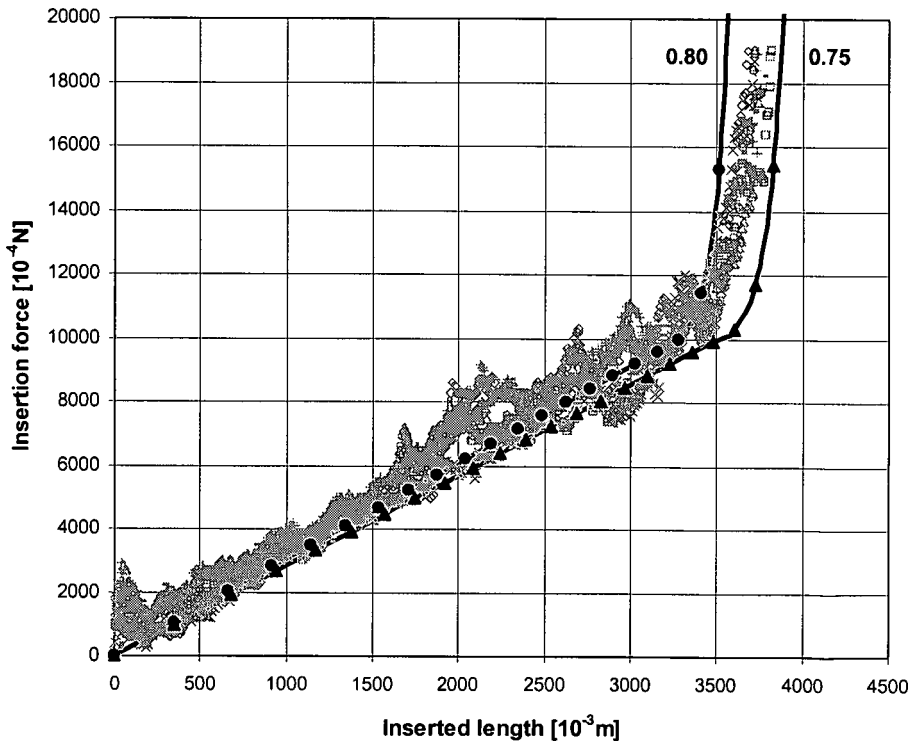

Figure 8.2.7 A comparison of the theoretical results for $\mu = 0.80$ (●) and $\mu = 0.75$ (▲) with the experimental data (grey symbols) for $d = 6$ mm and $D = 15$ mm.

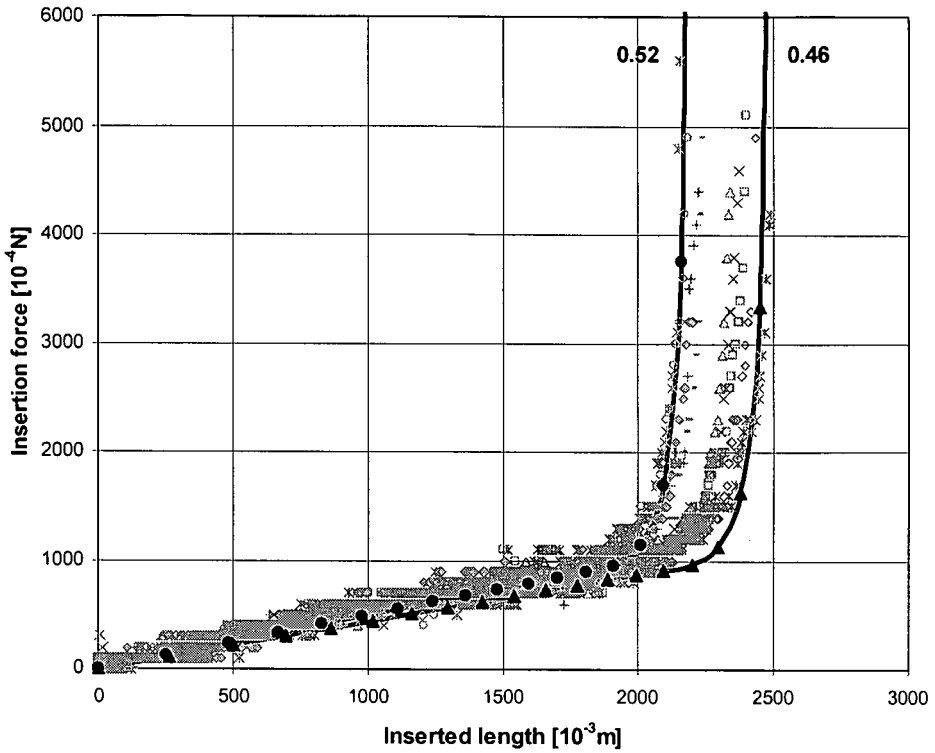

Figure 8.2.8: A comparison of the theoretical results for $\mu = 0.52$ (●) and $\mu = 0.46$ (▲) with the experimental data (grey symbols) for $d = 3$ mm and $D = 19$ mm.

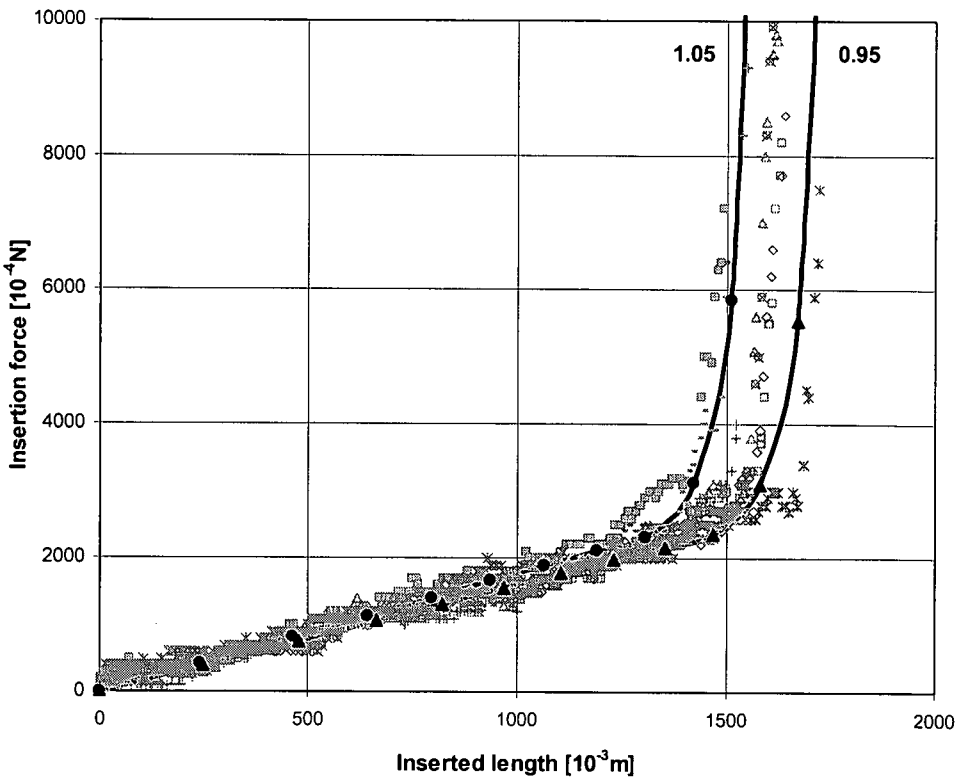

Figure 8.2.9 A comparison of the theoretical results for $\mu = 1.05$ (●) and $\mu = 0.95$ (▲) with the experimental data (grey symbols) for $d = 4$ mm and $D = 19$ mm.

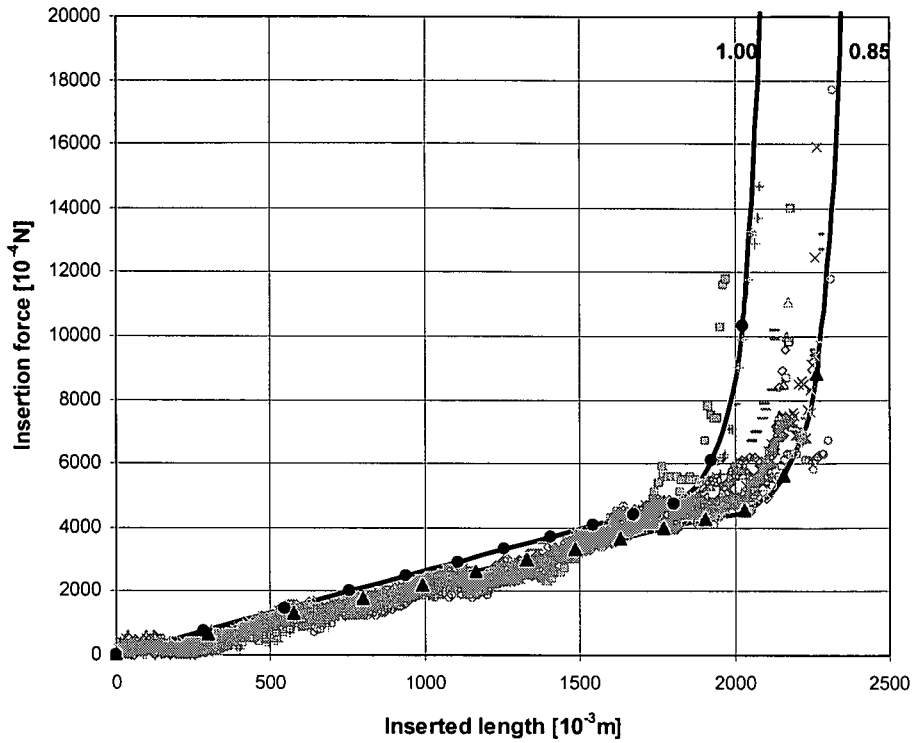

Figure 8.2.10 A comparison of the theoretical results for $\mu = 1.00$ (●) and $\mu = 0.85$ (▲) with the experimental data (grey symbols) for $d = 5$ mm and $D = 19$ mm.

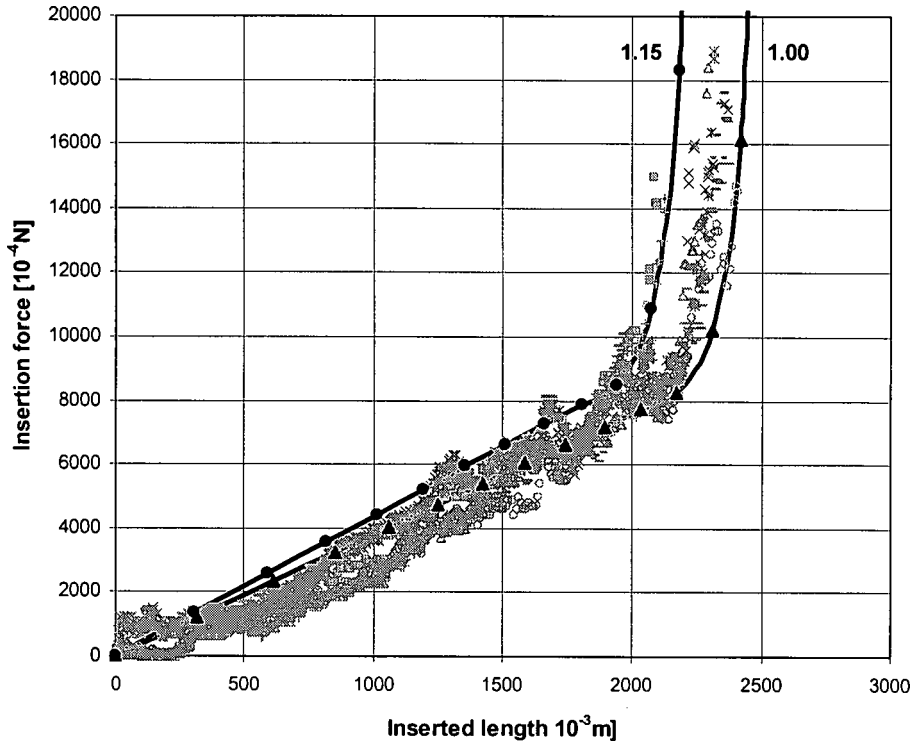

Figure 8.2.11 A comparison of the theoretical results for $\mu = 1.15$ (●) and $\mu = 1.00$ (▲) with the experimental data (grey symbols) for $d = 6$ mm and $D = 19$ mm.

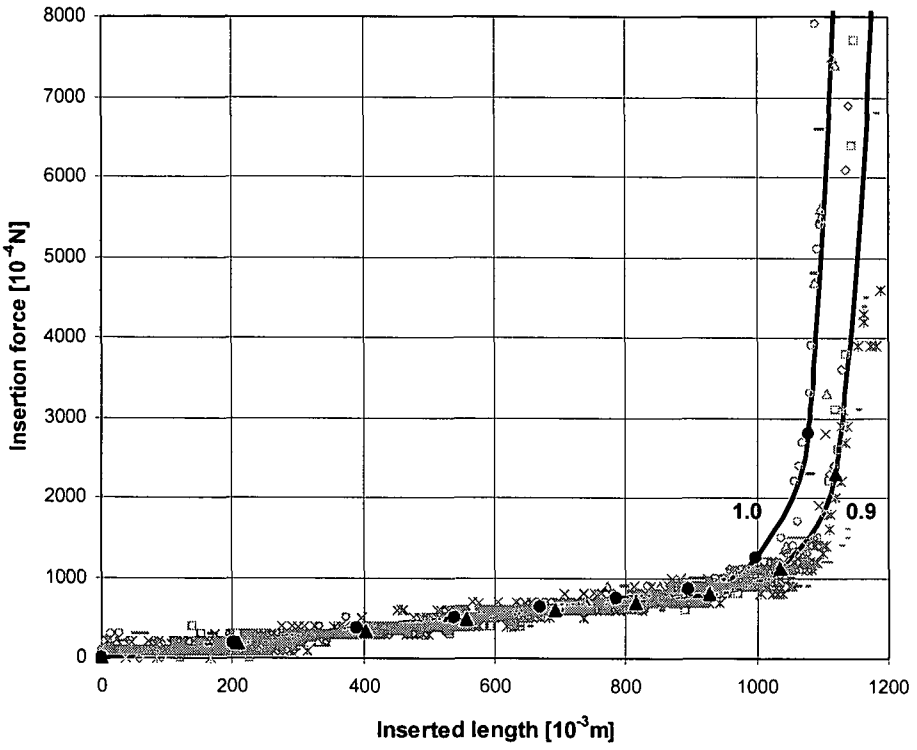

Figure 8.2.12 A comparison of the theoretical results for $\mu = 1.00$ (●) and $\mu = 0.90$ (▲) with the experimental data (grey symbols) for $d = 3$ mm and $D = 22.8$ mm.

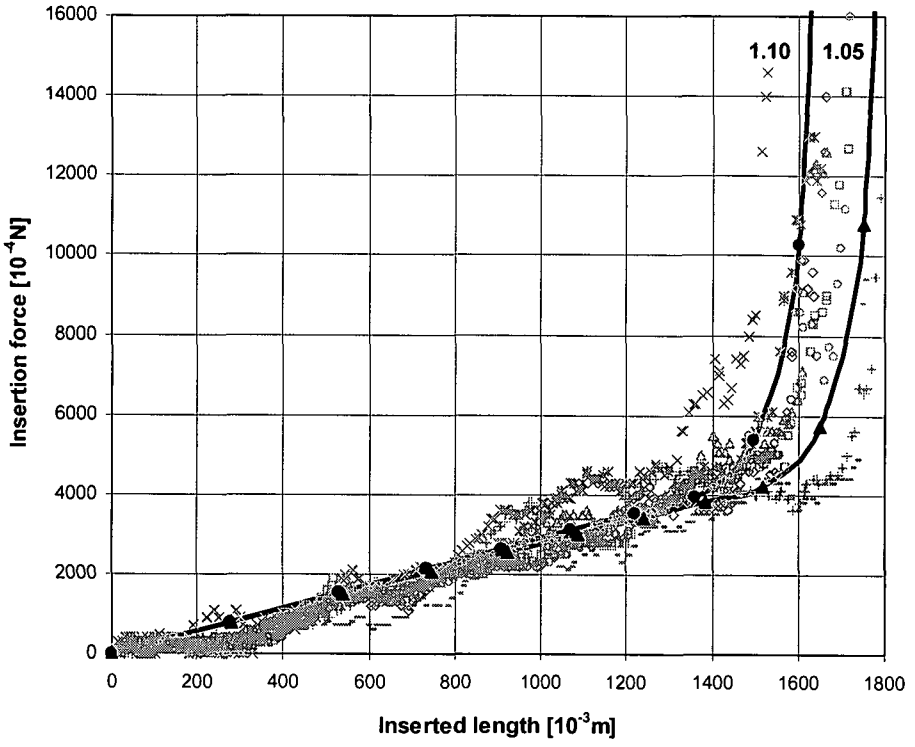

Figure 8.2.13 A comparison of the theoretical results for $\mu = 1.10$ (●) and $\mu = 1.05$ (▲) with the experimental data (grey symbols) for $d = 5$ mm and $D = 22.8$ mm.

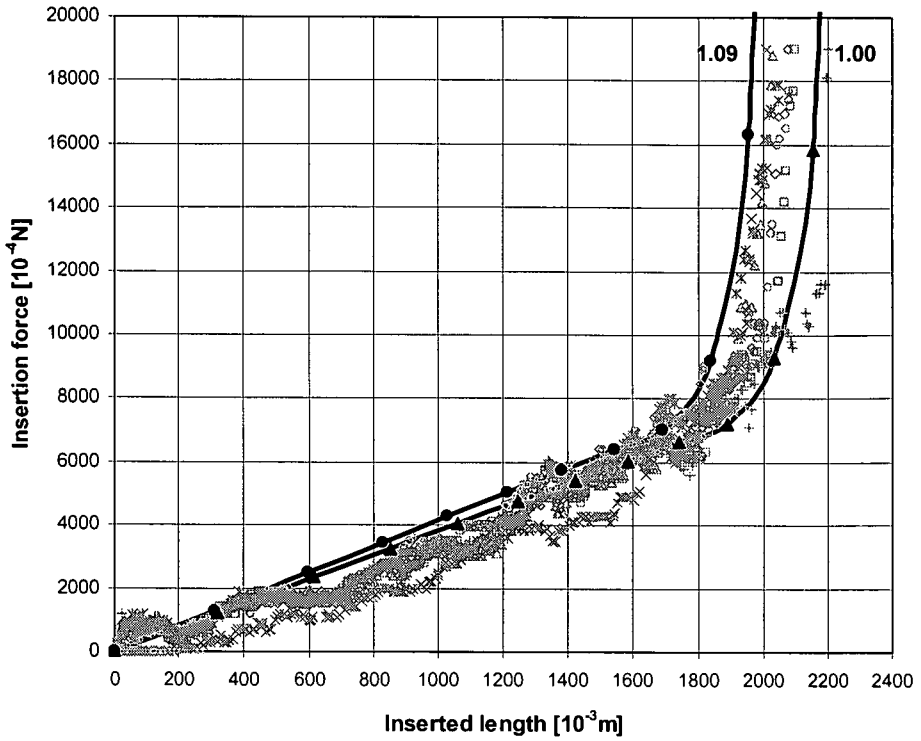

Figure 8.2.14 A comparison of the theoretical results for $\mu = 1.09$ (●) and $\mu = 1.00$ (▲) with the experimental data (grey symbols) for $d = 6$ mm and $D = 22.8$ mm.

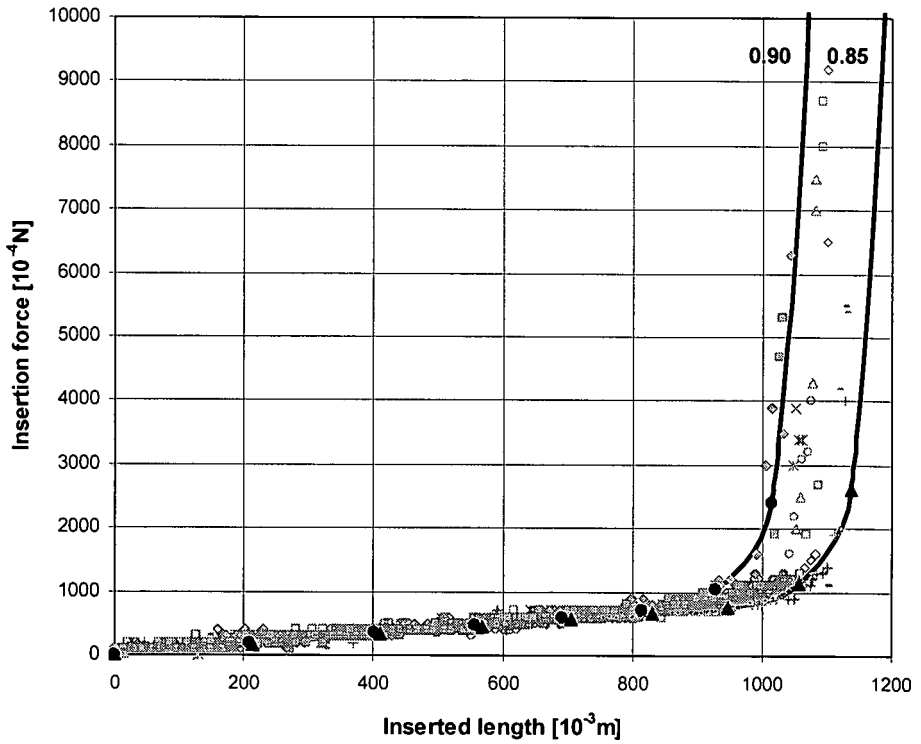

Figure 8.2.15 A comparison of the theoretical results for $\mu = 0.90$ (●) and $\mu = 0.85$ (▲) with the experimental data (grey symbols) for $d = 3$ mm and $D = 28.6$ mm.

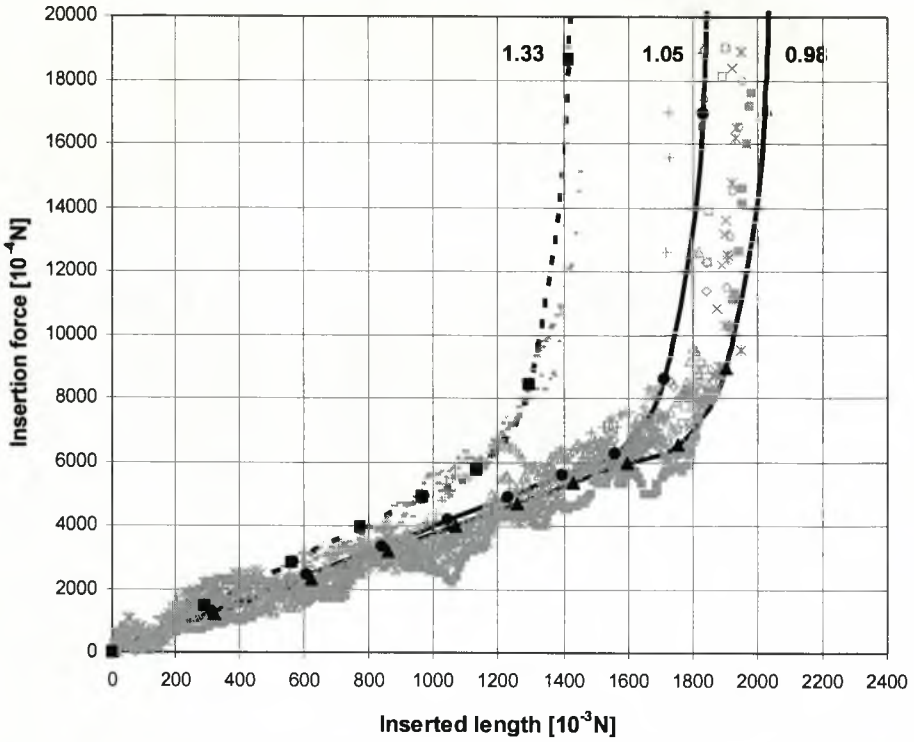

Figure 8.2.16 A comparison of the theoretical results for $\mu = 1.33$ (■), $\mu = 1.05$ (●) and $\mu = 0.98$ (▲) with the experimental data (grey symbols) for $d = 6$ mm and $D = 28.6$ mm.

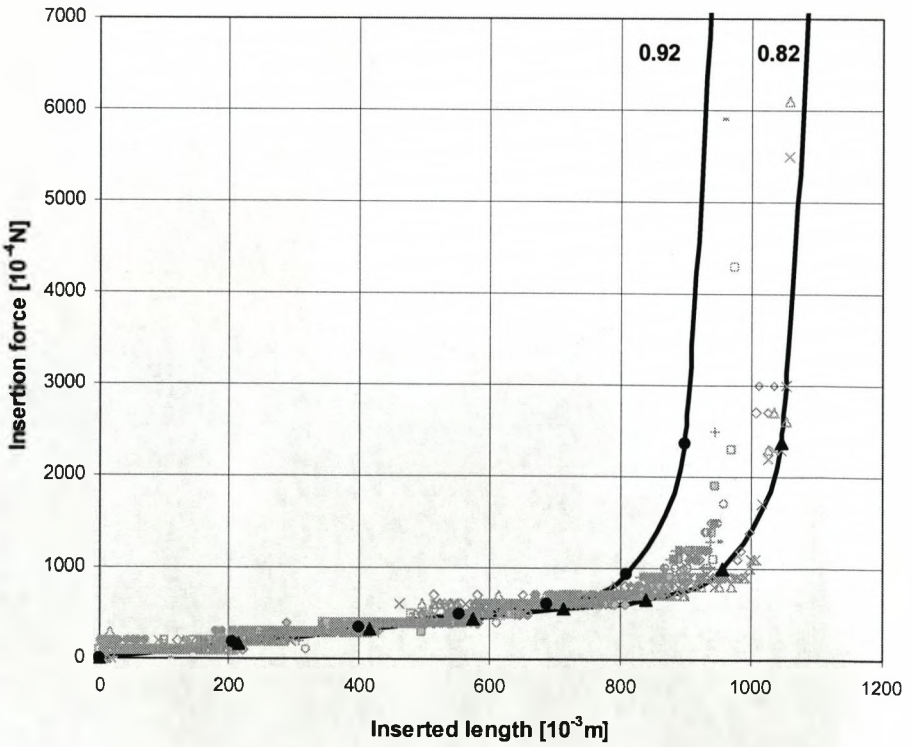

Figure 8.2.17 A comparison of the theoretical results for $\mu = 0.92$ (●) and $\mu = 0.82$ (▲) with the experimental data (grey symbols) for $d = 3$ mm and $D = 33.4$ mm.

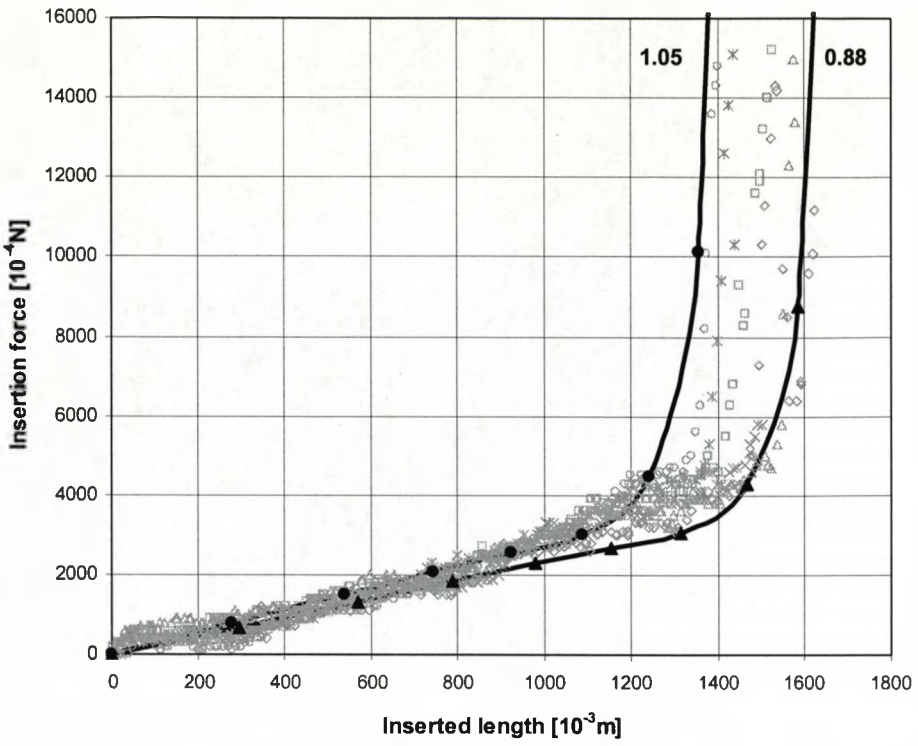

Figure 8.2.18 A comparison of the theoretical results for $\mu = 1.05$ (●) and $\mu = 0.88$ (▲) with the experimental data (grey symbols) for $d = 5$ mm and $D = 33.4$ mm.

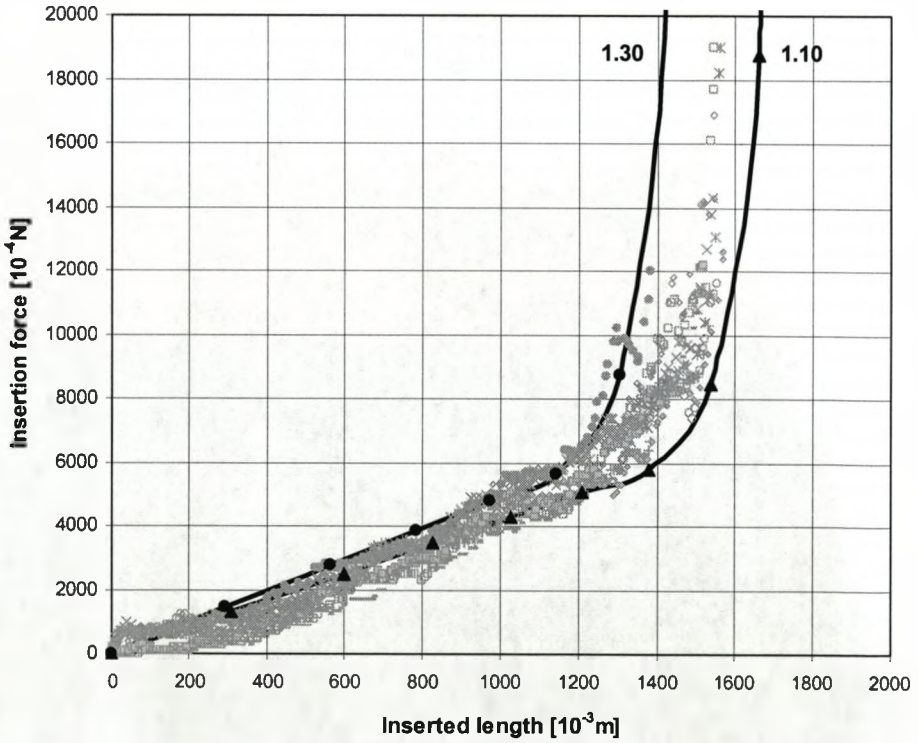

Figure 8.2.19 A comparison of the theoretical results for $\mu = 1.30$ (●) and $\mu = 1.10$ (▲) with the experimental data (grey symbols) for $d = 6$ mm and $D = 33.4$ mm.

9. Discussion

9.1 Comparison of Theoretical Results with Experimental Work

9.1.1 Rod deformations

Section 8.1, which compares the theoretical results of the present model with the experimental data, shows that there is a reasonable agreement between the theoretical results and the experimental data for the number of total rod deformations. However, the results are less satisfactory when the total number of deformations is split between sinusoidal deformations and helical deformations. The most likely reason is that it was found difficult to differentiate between sinusoidal and helical deformations in the transitional region. Nevertheless the results confirm the validity of the theoretical model developed in this work.

9.1.2 Insertion tests

Section 8.2, which compares the theoretical results of the present model with the experimental data, shows that the model provides an excellent description of the relationship between the insertion force and the inserted length. The theoretical model also gives the initial linear relationship between the insertion force and the inserted length and then, once a critical penetration length is reached, a rapid increase in the insertion force.

The scatter in the experimental data is accommodated by the appropriate choice of the coefficient of friction between the rod and the wall of the containing cylinder, with the choice of the appropriate friction coefficient determined by the initial slope of the linear graph of the variation of the friction force with the inserted length. It can be seen from the graphs of the experimental results presented in Sections 6.4 and 8.2 that the initial slopes of nominally identical tests can differ appreciably. It can be also seen from the results in Section 8.2 that a spread in the coefficient of friction of about 10% to 20% is required to describe all nominally identical results.

Furthermore, the values of the coefficient of friction appear to vary from test to test, from about 0.5 for the smallest diameter rod to about 1.0 for the largest rod. This seems to suggest that in the case of dynamic conditions the coefficient of friction depends not only on the material properties of the two surfaces, but is also sensitive to contaminants and localised imperfections.

Nevertheless, provided the initial slope of the variation of the insertion force with the inserted length is known, the appropriate coefficient of friction can be determined for each condition with acceptable accuracy.

9.2 Sinusoidal and Helical Buckling

9.2.1 Sinusoidal buckling

As shown in section 7.2.7, the transition to helical buckling commences for the following conditions

$$P_{cr} = 2^{1.5}\left(\frac{EIgm_L}{0.5(D-d)}\right)^{0.5} \tag{9.2.1}$$

It should be further noted that before the transition to helical buckling the only forces acting on the rod are the frictional forces between the rod and the inner walls of the containing cylinder. If we then denote the inserted length at transition as L_{cr}, the critical force is also given as

$$P_{cr} = \mu m_L g L_{cr} \tag{9.2.2}$$

Equating equation (9.2.1) and equation (9.2.2) we then obtain

$$L_{cr} = \frac{4d}{\mu}\left(\frac{EI}{m_L g d^3}\right)^{1/2}\left(\frac{1}{D/d-1}\right)^{1/2} \tag{9.2.3}$$

which can be re-written as

$$\frac{L_{cr}}{d} = 4\frac{1}{\mu}\left(\frac{EI}{m_L g d^3}\right)^{1/2}\left(\frac{1}{D/d-1}\right)^{1/2} \qquad (9.2.4)$$

Hence the dimensionless length of the transition to helical buckling is a function of three dimensionless groups: (i) the coefficient of friction μ, (ii) the parameter $EI/m_L g d^3$, which combines the relevant material properties of the rod, and (iii) the geometry parameter D/d. The dimensionless length of the transition to helical buckling decreases with the first parameter and the third parameter, and increases with the second parameter.

9.2.2 Helical buckling

Experimental work indicates that there is a transitional region between sinusoidal buckling and fully established helical buckling. A particular transition regime is assumed in this work, but the effect of any reasonable choice of the transition regime is relatively small.

As demonstrated by experimental work and the theoretical model developed in this work, the required insertion force increases rapidly after the transition to helical buckling. This, as discussed above, ensures that the length of the individual buckled elements decreases rapidly after the transition to helical buckling. The decrease is so rapid that there is an asymptotic limit on the maximum insertion. This is discussed further in the next section.

9.3 Maximum Insertion

Theoretical results for the insertion force as a function of the inserted length for a rubber rod in glass (d = 5 mm, D = 15 mm and μ = 0.7) are presented in Figure 9.3.1.

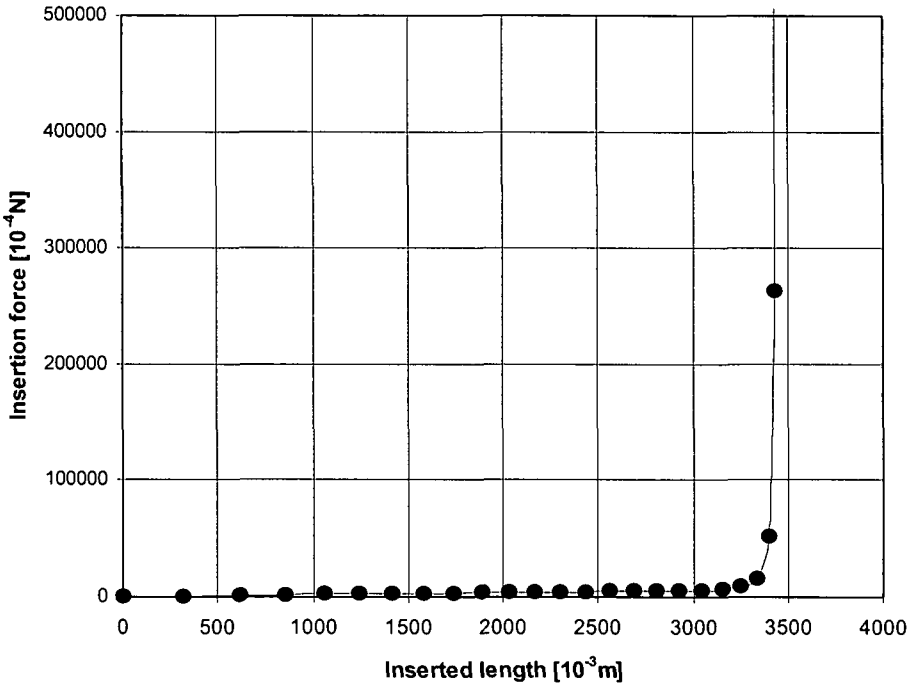

Figure 9.3.1 Theoretical results for the insertion force as a function of the inserted length for a rubber rod in glass (d = 5 mm, D = 15 mm and μ = 0.7).

The theoretical results also show that the region of sinusoidal deformation extends to L_{cr} = 3077 mm, and that the total theoretical insertion is L_{tot} = 3450 mm. This implies that the maximum theoretical extent of helical deformations is 373 mm, or about 11% of the total theoretical insertion.

This result is typical for all cases investigated in this work, with the typical maximum theoretical extent of helical deformation of about 12% of the total theoretical insertion, and the maximum theoretical extent of helical deformation up to about 22% of the total theoretical insertion.

It should be pointed out that the maximum theoretical insertion is only achievable if the available insertion force is infinitely high and if the rod feed conditions are such that the

insertion system can accommodate very small deformation without tripping. For example, the insertion force typically used in the present series of experiment was of the order of 2 N, which would limit the maximum insertion to about 3350 mm. Hence the extent of helical deformations would be about 273 mm or about 9% of the maximum deformation.

The maximum deformation would thus depend on the available insertion force. The theoretical model developed here can then be used to determine the maximum insertion. However, because of the rapid increase of the required insertion force after transition to helical buckling, the maximum penetration would be, typically, about 10% above the critical length L_{cr} given by equation 9.2.3.

9.4 Influence of Design Parameters

The influence of the design parameters will be discussed with reference to equation (9.2.3). The influence of the coefficient of friction μ is straightforward. The maximum insertion increases indirectly with the coefficient of friction. This is also demonstrated in figure 9.4.1.

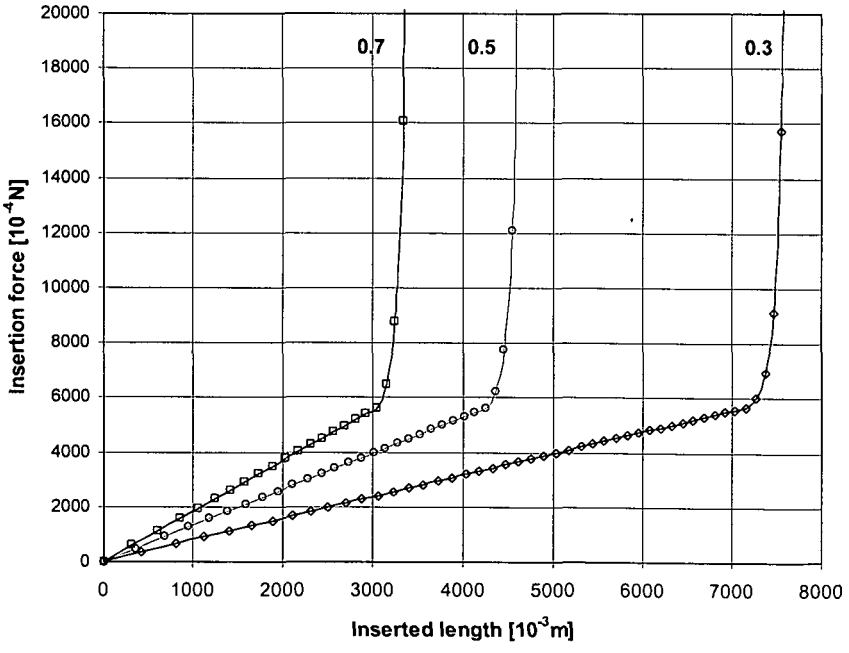

Figure 9.4.1 Influence of the coefficient of friction on the theoretical results for the insertion force as a function of the inserted length for a rubber rod in glass (d = 5 mm, D = 15 mm, and μ = 0.7 (□), μ = 0.5 (○) and μ = 0.3 (◇)).

Equation 9.2.3 also demonstrates that the maximum insertion increases with the square root of the elastic modulus ($E^{0.5}$), and, since mass per unit length m_L is proportional to the material density ρ, the maximum insertion decreases with the square root of the material density ($\rho^{-0.5}$).

The influence of the rod diameter in the present case can be also determined from equation (9.2.3). Since the second moment of area I increases with d^4, the mass per unit length with d^2 and the last term of equation (9.2.3) is approximately proportional to $d^{0.5}$, the maximum insertion increases approximately with the rod diameter d. This is also demonstrated in Figure 9.4.2. This is confirmed by the experimental results shown in figures 6.4.20, 6.4.21, 6.4.22 and 6.4.23.

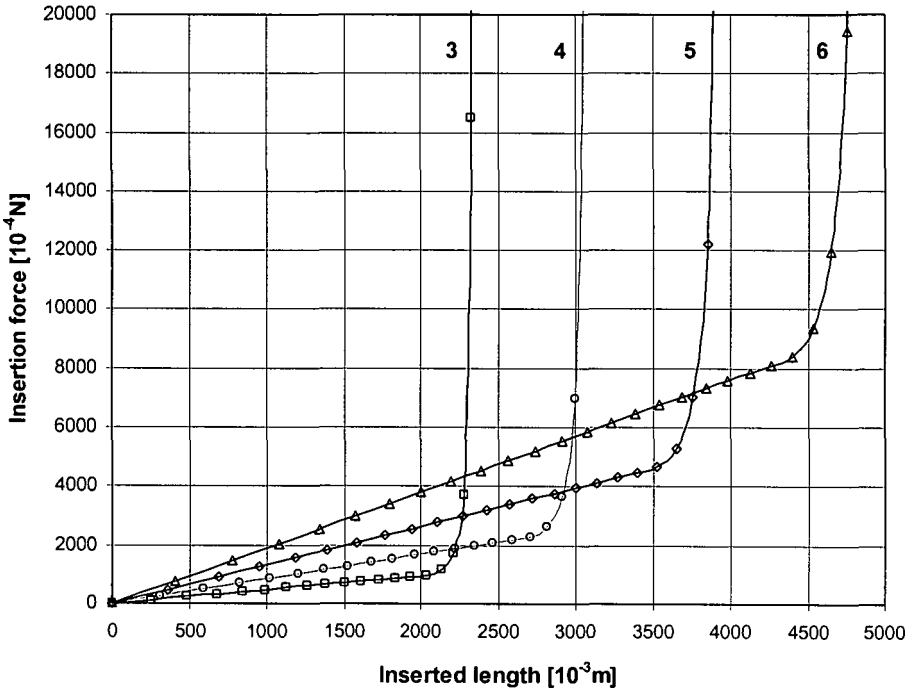

Figure 9.4.2 Influence of the rod diameter on the theoretical results for the insertion force as a function of the inserted length for a rubber rod in glass (D = 15 mm, μ = 0.7, and d = 3 mm (□), d = 4 mm (○), d = 5 mm (◇) and d = 6 mm(Δ)) .

The influence of the diameter of the containing cylinder D can also be determined from equation (9.2.3). This shows that, for a given rod diameter d, and constant material properties and the coefficient of friction, the maximum insertion increases with decreasing diameter D. This is also demonstrated in figure 9.4.3. This, perhaps surprising results is also confirmed by the experimental results in figures 6.4.24 and 6.4.25.

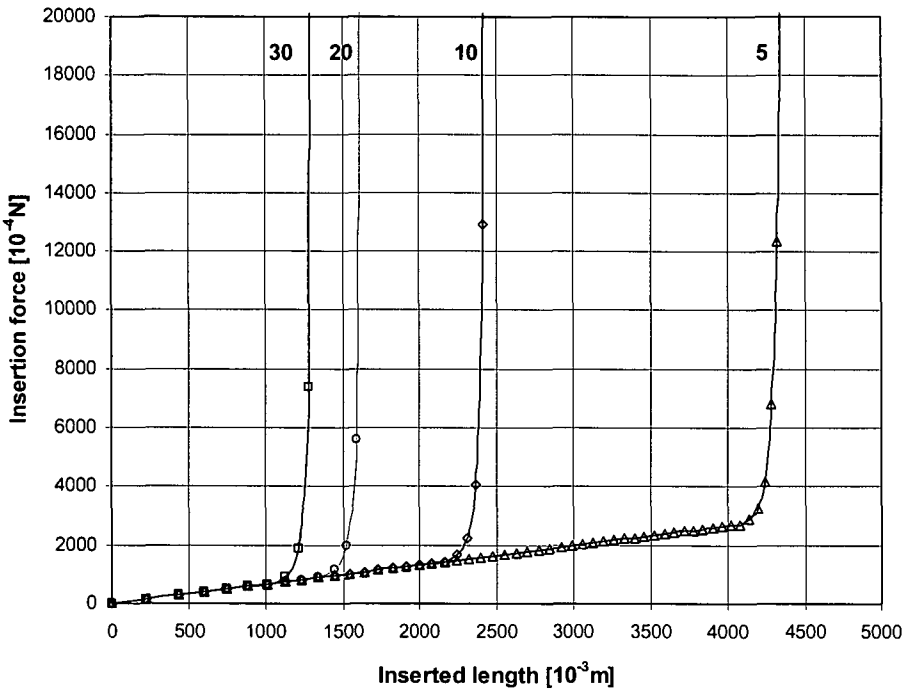

Figure 9.4.3 Influence of the diameter of the containing cylinder on the theoretical results for the insertion force as a function of the inserted length for a rubber rod in glass (d = 3 mm, μ = 0.7, and D = 30 mm (□), D = 20 mm (○), D = 10 mm (◇) and D = 5 mm(Δ)).

9.5 Extrapolation to Coiled Tubing

The model developed in the present work is extrapolated to typical field situations using coil tubing. The base scenario assumes coiled steel tubing of outside diameter d = 38 mm and wall thickness t = 3 mm, and the following material properties: $E = 2.1 \times 10^{11}$ Nm^{-2} and ρ = 7900 kgm^{-3}, being inserted into horizontal casing with D = 100 mm. The variation of the insertion force with the inserted length for three different values of the coefficient of friction (μ = 0.1, 0.2 and 0.3) is shown in figure 9.5.1.

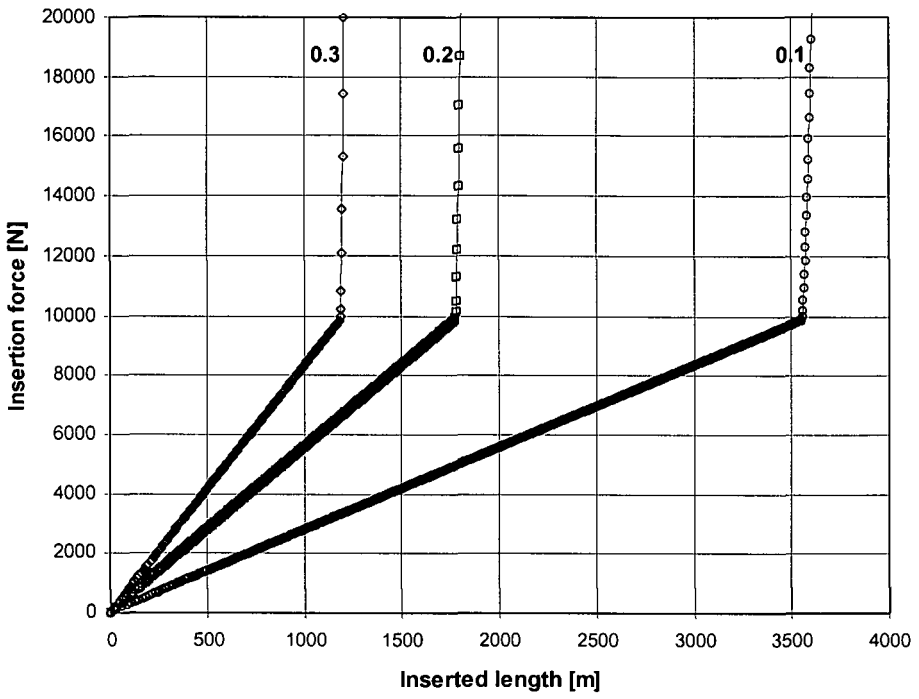

Figure 9.5.1 Influence of the coefficient of friction on the theoretical results for the insertion force as a function of the inserted length for steel coiled tubing (d = 38 mm, D = 100 mm, and μ = 0.3 (◇), μ = 0.2 (□) and μ = 0.1 (○)).

The critical lengths for the transition to helical buckling are 1180 m, 1780 and 3560 m for μ = 0.3, 0.2 and 0.1 respectively, with the maximum insertion about 3% above the critical lengths for the transition to helical buckling.

The figure clearly demonstrates the importance of the lowest possible coefficient of friction in order to maximise the maximum insertion.

The effect of increasing the diameter of the coiled tubing is demonstrated for D = 100 mm, t = 3 mm, μ = 0.2 and three different values of the diameter (d = 48 mm, d = 38 mm and d = 28 mm) in figure 9.5.2.

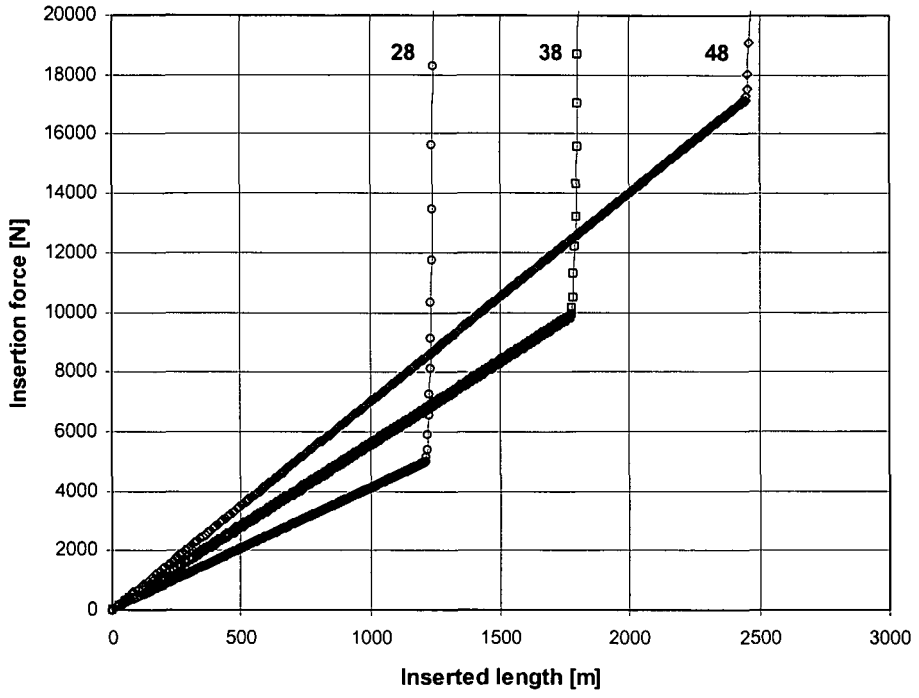

Figure 9.5.2: Influence of the external diameter of coiled tubing on the theoretical results for the insertion force as a function of the inserted length for steel coiled tubing (D = 100 mm, μ = 0.2, and d = 28 mm (○), d = 38 mm (□) and d = 48 mm (◇)) .

The figure demonstrates, once again, that increasing the diameter d increases the maximum insertion length.

As discussed above the maximum insertion length can be increased by increasing the elastic modulus of the coiled tubing material and by decreasing the density of the coiled tubing material. It should be noted, however, that increasing the wall thickness of the coiled tubing has no effect. The reason is that both the second moment of area and the mass per unit length are approximately proportional to the wall thickness, and hence, as shown by equation 9.2.3, the effect on the maximum insertion length is negligible.

Finally, the effect of the diameter of the horizontal casing D is demonstrated for d = 38 mm, d = 3 mm, μ = 0.2 and three different values of the diameter (D = 125 mm, D = 100 mm and D = 75 mm) in figure 9.5.3. The figure shows, once again, that the maximum insertion length increases with the decreasing diameter of the horizontal casing.

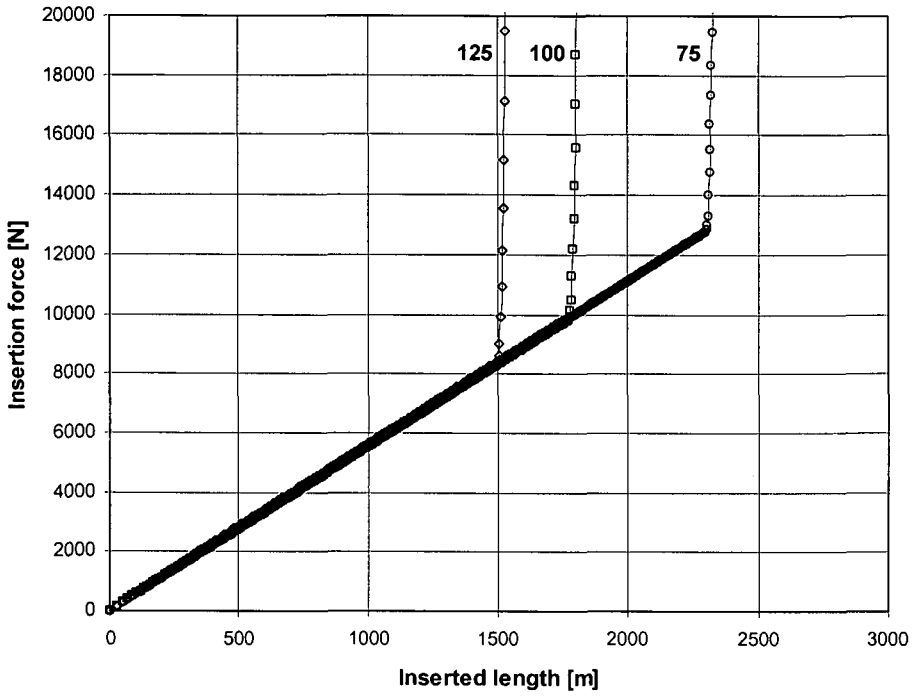

Figure 9.5.3 Influence of the diameter of the horizontal casing on the theoretical results for the insertion force as a function of the inserted length for steel coiled tubing (d = 38 mm, μ = 0.2, and D = 75 mm (○), D = 100 mm (□) and D = 125 mm (◇)).

10. Conclusions

The research programme investigated the limits on the maximum penetration of coiled tubing in horizontal oil wells. These limits are due to buckling, in particular helical buckling, during which the required insertion forces increase exponentially.

Previous investigations have been reviewed; these investigations can be divided into two areas:

(i) The theoretical approach backed by laboratory experiments in which the end of the containing tube is obstructed, so as to allow buckling to develop.

(ii) Full scale tests that meet with the practical problems but do not provide as much information, and difficulties of scale can also extend the time required to complete satisfactory tests.

The laboratory tests have demonstrated the buckling phenomenon but have not re-created the conditions existing in a well.

During the course of this research a completely new approach to the investigation of this important problem has been developed. A novel experimental apparatus was developed, which uses tubular members of very low flexural rigidity and high value of friction between the tubular and a transparent containing cylinder. This apparatus allows limits on penetration of the tubulars to be observed in under 5 m of insertion.

The experimental apparatus enables the simultaneous measurement of the insertion forces and the inserted length, using a suitable designed control and data acquisition system.

All of the experimental results demonstrate similar qualitative behavior in that the shape of the rod being inserted into the tube consists of three regions:

(i) The initial, apparently straight section.

(ii) The subsequent section with sinusoidal deformations.

(iii) The final section with helical deformations.

The region with the fully developed helical deformations is relatively small, and is confined to about the last 10% to 20% of the inserted rod.

All the graphs for the variation of the insertion force with the inserted length indicate a clear trend:

(i) The insertion force initially increases linearly with the inserted length.

(ii) A critical length is reached, at which the insertion force increases very rapidly. Even though all figures demonstrate some scatter and uncertainty, the critical length is reasonably well defined for all combinations of the rod and the containing cylinder diameter investigated in this work.

(iii) The graphs also indicate that for a constant diameter of the containing cylinder the critical insertion length increases with the diameter of the rod, and that for a constant diameter of the rod, the critical insertion length decreases with the diameter of the containing cylinder.

A theoretical model of penetration has been developed, which is in excellent agreement with the experimental data. This model can be used to determine the importance of various design parameters on the maximum penetration of tubulars in horizontal wells.

The model shows that the dimensionless length of the transition to helical buckling is a function of three dimensionless groups:

(i) the coefficient of friction μ,

(ii) the parameter $EI/m_L g d^3$, which combines the relevant material properties of the rod.

(iii) the geometry parameter D/d.

The dimensionless length of the transition to helical buckling decreases with the first parameter and the third parameter, and increases with the second parameter.

The theoretical model also shows that for a constant diameter of the containing cylinder the critical insertion length increases with the diameter of the rod and that for a constant diameter of the rod the critical insertion length decreases with the diameter of the containing cylinder.

Finally, the model suggests that in order to maximise the penetration of coiled tubing in horizontal oil wells the friction factor should be as small as possible, the modulus of elasticity should be as large as possible, the diameter of the tubing should be as large as possible and the diameter of the well should be as small as possible. It is also shown that the wall thickness has a negligible influence on the maximum penetration.

11. Further Work

Future research work could look at the critical areas which were identified during the course of this study and include the following :

(i) Examination of the influence of the friction coefficient and how to manage its behaviour.

(ii) Investigation of non-straight, non-horizontal tubes.

(iii) Application of the mathematical model to full operational conditions and development of an algorithm to optimise the penetration of coiled tubing in field conditions.

12. References

Bhalla, K., 1996, Achieving extended reach, *Society of Petroleum Engineers*, Publication No. 96023, February 1996.

Cheatham, J.B., Pattillo, P.D. 1984, Helical post buckling configuration of a weightless column under the action of an axial load, *Society of Petroleum Engineers*, Publication No. 10854, August 1984, 467-472.

Chen,Yu-Che., Lin, Yu-Hsu., Cheatham, J.B. 1990, Tubing and casing buckling in horizontal wells, *Society of Petroleum Engineers*, Publication No. 19176, February 1990, 140-142.

Chen,Yu-Che., Lin, Yu-Hsu., Cheatham, J.B., 1990, Author's reply to :- Tubing and casing buckling in horizontal wells, *Society of Petroleum Engineers*, Publication No. 19176, August 1990.

Dawson, R., Paslay, P.R., 1884, Drill pipe buckling in inclined holes, *Society of Petroleum Engineers*, Publication, April 1984.

Den Hartog, J.P., 1977, *Strength of Materials*, Dover Publications, 1977. SBN 0-486-60755-0

Malaysian Rubber Producers Association, 1974, *Engineering Design with Natural Rubber*, (M.R.P.A.), 4th Edition (Reprinted 1978).

Gere, J.M., Timoshenko, S.P., 1961, *Theory of Elastic Stability*, McGraw Hill, 1961

He, Xiaojun., Killingstad, Age., 1993, Helical buckling and lock-up conditions for coiled tubing in curved wells, *Society of Petroleum Engineers*, Publication No. 25370, February 1993, 10-15.

Hishada, H., Higuchi, K., Hatakeyama,T., 1996, Prediction of helical/sinusoidal buckling, *Society of Petroleum Engineers*, Publication No. 36384, September 1996, 175-184.

Kwon,Y.W., 1986, A precise solution for helical buckling, *Society of Petroleum Engineers*, Publication No. 14729, February 1986, 91-98.

Love, A.E.H., 1927, *A Treatise on The Mathematical Theory of Elasticity*, Cambridge University Press, 4th edition 1927 (reprinted 1952).

Lubinski, A., Althouse, W.S., Logan J.L., 1962, Helical buckling of tubing sealed in packers. *Society of Petroleum Engineers*, Publication No. 178, June 1962, 655-670.

Madhukar,Vable, 2002, *Mechanics of Materials*, First Edition, Oxford University Press, 2002, ISBN 0-19-513337-4.

Mitchell, R.F., 1980, Buckling behavior of well tubing, the packer effect, *Society of Petroleum Engineers*, Publication No. 9264, September, 1980, 1-9.

Mitchell, R.F., 1986a, Simple frictional analysis of helical buckling of tubing, *Society of*

Petroleum Engineers, Publication No. 13064, January 1986, 457-465.

Mitchell, R.F., 1986b, Numerical analysis of helical buckling, *Society of Petroleum Engineers*, Publication No. 14981, April 1986, 1-8.

Mitchell, R.F., 1986c, New concepts in helical buckling, *Society of Petroleum Engineers*, Publication No. 15470, October 1986, 1-11.

Rabia, H., 1985, *Oil Well Drilling Engineering, Principles and Practice*, Graham & Trotman 1985, ISBN 0-8610-661-6.

Tailby, R.J., Cobb, D.O., Riva, M.C.,Jones, C., 1993, A joint industry research project to investigate coiled tubing buckling, *Society of Petroleum Engineers*, Publication No. 26713, September 1993, 341-350.

Qui, Weiyong., Miska, S., Volk, L., 1998, Effect of coiled tubing initial configuration in a hole of constant curvature, *Society of Petroleum Engineers*, Publication No. 46009, April 1998, 51-59.

13. Appendices

Appendix A

This appendix contains the paper " Penetration of tubulars in horizontal oil wells" published by the Institution of Mechanical Engineers.

Appendix	Content
Appendix A	" Penetration of tubulars in horizontal oil wells"

Appendix B

This appendix contains the paper " Design of a flexible small scale drive" published by the Czech Technical University, Prague, 3rd International Conference on Advanced Engineering Design 2003.

Appendix	Content
Appendix B	"Design of a flexible small scale drive"

PUBLISHED PAPER(S)
NOT INCLUDED WITH THESIS

Appendix C

This appendix contains the procedure used to determine the elastic modulus.

Appendix	Content
Appendix C	Procedure used to determine the elastic modulus

Appendix C

This appendix contains the procedure used to determine the elastic modulus.

a. Test set up as that shown in Figure 4.2.1.

b. Samples must be kept clean and not come into contact with solvents, oils or any fluids or materials which could alter their material properties in any way.

c. The test area with all samples to be tested must be kept at a constant temperature for at least two hours prior to the test commencing.

d. All samples under test must be the same one metre length.

e. Install a test sample e.g. 3 mm diameter specimen to the rig with no weight except that of the weight carrier.

f. Zero the dial gauge on datum surface at top of clamp attached to test sample to give minimum length before extension commences.

g. Add a 10-gram weight to carrier and bring down pointer to contact datum surface and record extension. Time taken from applying load to recording extension is kept to 30 seconds for all loads applied up to the maximum.

h. After the maximum load has been applied, all loads must be removed and test sample length measured to ensure sample returns to its original length.

i. Carry out a minimum of 5 tests per sample.

k. Repeat above for rod sizes 2 mm to 6 mm diameter

Appendix D

This appendix contains the buckling analysis, fixed-free with own weight

Appendix	Content
Appendix D	Buckling analysis, fixed-free with own weight

Appendix D
Buckling Analysis
Fixed-Free
Buckling with own Weight

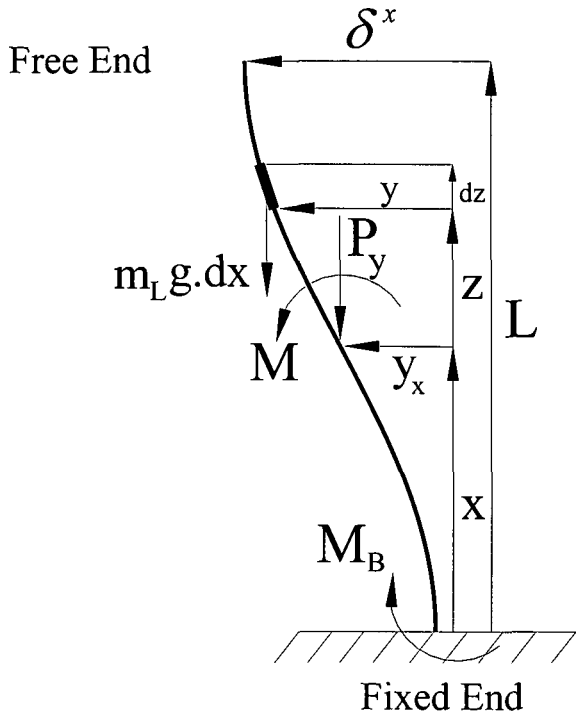

Figure Appendix D.1

The basic bending equation is $$EI\frac{d^2y}{dx^2} = M \qquad \text{(D1)}$$

Consider the bending moment at a point x from the fixed end. Initially the bending moment dM will be calculated for a small element dx situated at a distance $(z+x)$ from the fixed end. The total moment M, at x, will be obtained by integrating dM between x and L

Mass of element $$dm = m_L dz \qquad \text{(D2)}$$

Force is $$dF = dmg = m_L g dz \qquad \text{(D3)}$$

Elemental bending moment $$dM = dF(y - y_x) \qquad \text{(D4)}$$

i.e. $$dM = m_L g.dz[y - y_x] \qquad \text{(D5)}$$

Total moment $$M = \int_x^L m_L g[y - y_x]dz \qquad \text{(D6)}$$

At this time y_x can be considered as constant hence

$$M = m_L g \int_x^L y dz - m_L g \int_x^L y_x dz \tag{D7}$$

$$M = m_L g \int_x^L y dz - m_L g y_x [z]_x^L \tag{D8}$$

$$M = m_L g \int_x^L y dz - m_L g y_x (L - x) \tag{D9}$$

Equation (D9) gives the moment acting on the beam at a distance x from the fixed end. To consider the general equation for bending, the deflection y_x should now be considered as a general deflection y at any point x.

i.e. $$y_x \equiv y \tag{D10}$$

Therefore the general bending moment is:

$$M = m_L g \int_x^L y dz - m_L g y (L - x) \tag{D11}$$

Substituting equation (D11) into equation (D1)

$$EI \frac{d^2 y}{dx^2} = m_L g \int_x^L y dz - m_L g y (L - x) \tag{D12}$$

$$\therefore EI \frac{d^2 y}{dx^2} + m_L g y (L - x) - m_L g \int_x^L y dz = 0 \tag{D13}$$

To eliminate dimensions let

$$\nu = \frac{y}{L} \qquad \therefore y = \nu L \tag{D14}$$

$$\xi = \frac{x}{L} \qquad \therefore x = \xi L \tag{D15}$$

$$\varphi = \frac{z}{L} \qquad \therefore z = \varphi L \tag{D16}$$

Substitute into (D13)

$$EI \frac{d^2 \nu L}{d(\xi^2 L^2)} + m_L g \nu L (L - \xi L) - m_L g \int_{\frac{x}{L}}^{\frac{L}{L}} \nu L L d\varphi = 0 \tag{D17}$$

$$\frac{EIL}{L^2} \frac{d^2 \nu}{d\xi^2} + m_L g \nu L L (1 - \xi) - m_L g L^2 \int_{\xi}^{1} \nu d\varphi = 0 \tag{D18}$$

$$\frac{EI}{L}\frac{d^2v}{d\xi^2} + m_L g v L^2(1-\xi) - m_L g L^2 \int_{\xi}^{1} v\,d\varphi = 0 \qquad \text{(D19)}$$

Multiply by $\frac{L}{EI}$

$$\frac{d^2v}{d\xi^2} + \frac{m_L g v L^2 L}{EI} v(1-\xi) - \frac{m_L g L^2 L}{EI} \int_{\xi}^{1} v\,d\varphi = 0 \qquad \text{(D20)}$$

$$\frac{d^2v}{d\xi^2} + \frac{m_L g v L^3}{EI} v(1-\xi) - \frac{m_L g L^3}{EI} \int_{\xi}^{1} v\,d\varphi = 0 \qquad \text{(D21)}$$

$$\text{Let} \quad K = \frac{m_L g L^3}{EI} \qquad \text{(D22)}$$

Hence $$\frac{d^2v}{d\xi^2} + Kv(1-\xi) - K\int_{\xi}^{1} v\,d\varphi = 0 \qquad \text{(D23)}$$

Boundary condition (a)

at $x = 0$ $y = 0$ (D24)

$x = 0$ $\frac{dy}{dx} = 0$ (D25)

Hence $\xi = 0$ $v = 0$ (D26)

$\xi = 0$ $\frac{dv}{d\xi} = 0$ (D27

Boundary condition (b)

at $x = L$ $y = y_L = \delta^x$ (D28)

hence $\xi = 1$ $v = \frac{y_L}{L} = v_L$ (D29)

Equation *D23* cannot be solved analytically and a numerical solution had to be found. The method adopted was to subdivide the rod into a number of steps and using the finite difference approach and the trapezoidal rule to create equations for each point to form a determinant which could be evaluated to give the eigenvalues for *K*. An Excel spreadsheet was used with the determinant evaluation and goal seek tools.

Formulation of equations to obtain eigenvalues

The general finite difference analysis is demonstrated on a six point, five interval system, shown below:

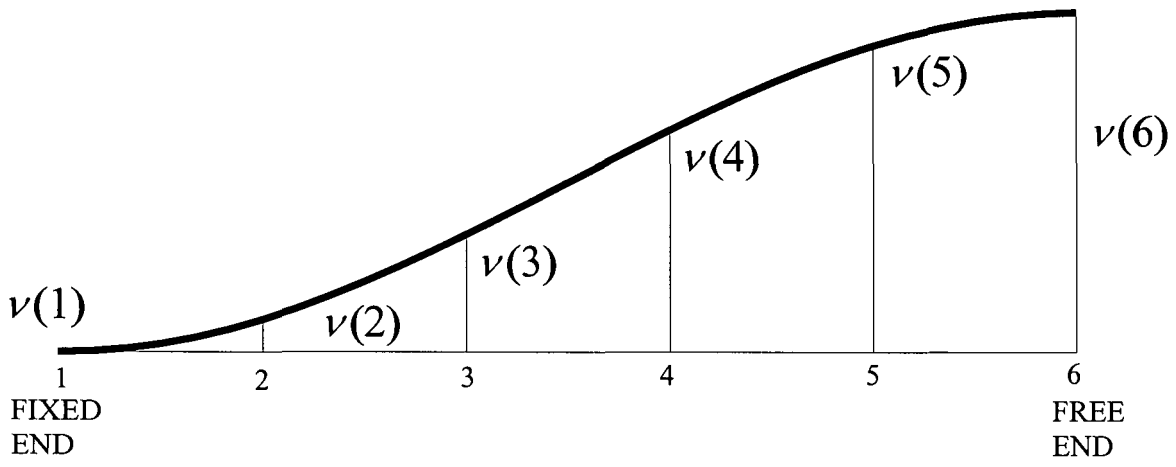

Equations are developed below for points 2, 3, 4 and 5 in terms of the 5 non zero displacements using equation (D23). As there will be 5 unknowns, a further equation is required. This equation is obtained from consideration of the fixing condition where the first 3 deflections are assumed to be parabolic in terms of x.

Development of the first equation (Using a forward second order approximation)

As the first 3 points are considered to conform to a parabola, the deflections can be expressed in terms of the interval lengths, applying the end conditions

$$\nu(1) = 0 \qquad \text{(D30)}$$

$$\frac{d\nu}{d\xi} = 0 \text{ at } x = 0 \qquad \text{(D31)}$$

produces

$$4\nu(2) - \nu(3) = 0 \qquad \text{(D32)}$$

To develop equations for points 2, 3, 4, and 5 $\frac{d^2\nu}{d\xi^2}$ has to be expressed in finite difference form and the integral is approximated using the trapezoidal rule.

i.e.
$$\frac{d^2\nu}{d\xi^3} = \frac{\nu(n-1) - 2\nu(n) + \nu(n+1)}{(\Delta\xi)^2} \tag{D33}$$

POINT 2 can be written as

$$\frac{\nu(1) - 2\nu(2) + \nu(3)}{(\Delta\xi)^2} + K\nu(2)[1 - \Delta\xi]$$
$$- K\Delta\xi\left[\tfrac{1}{2}\nu(2) + \nu(3) + \nu(4) + \nu(5) + \tfrac{1}{2}\nu(6)\right] = 0 \tag{D34}$$

and noting that, as shown above $\nu(1) = 0$ this simplifies to

$$-2\nu(2) + \nu(3) + K(\Delta\xi)^2\nu(2)[1 - \Delta\xi]$$
$$- K(\Delta\xi)^3\left[\tfrac{1}{2}\nu(2) + \nu(3) + \nu(4) + \nu(5) + \tfrac{1}{2}\nu(6)\right] = 0 \tag{D35}$$

which can be further re-arranged as

$$\nu(2)\left[K(\Delta\xi)^2(1 - \Delta\xi) - 2 - \tfrac{1}{2}K(\Delta\xi)^3\right]$$
$$+ \nu(3)\left[1 - K(\Delta\xi)^3\right]$$
$$+ \nu(4)\left[-K(\Delta\xi)^3\right]$$
$$+ \nu(5)\left[-K(\Delta\xi)^3\right]$$
$$+ \nu(6)\left[-\tfrac{1}{2}K(\Delta\xi)^3\right] = 0 \tag{D36}$$

POINT 3 can be written

$$\frac{\nu(2)-2\nu(3)+\nu(4)}{(\Delta\xi)^2}+K\nu(3)[1-2\Delta\xi]$$
$$-K\Delta\xi\left[\tfrac{1}{2}\nu(3)+\nu(4)+\nu(5)+\tfrac{1}{2}\nu(6)\right]=0 \qquad \text{(D37)}$$

$$\nu(2)+\nu(3)+\left[K(\Delta\xi)^2(1-2\Delta\xi)-2-\tfrac{1}{2}K(\Delta\xi)^3\right]$$
$$+\nu(4)\left[1-K(\Delta\xi)^3\right]+\nu(5)\left[-K(\Delta\xi)^3\right]$$
$$+\nu(6)\left[-\tfrac{1}{2}K(\Delta\xi)^3\right]=0 \qquad \text{(D38)}$$

POINT 4 can be written

$$\frac{\nu(3)-2\nu(4)+\nu(5)}{(\Delta\xi)^2}+K\nu(4)[1-3\Delta\xi]$$
$$-K\Delta\xi\left[\tfrac{1}{2}\nu(4)+\nu(5)+\tfrac{1}{2}\nu(6)\right]=0 \qquad \text{(D39)}$$

$$\nu(3)+\nu(4)+\left[K(\Delta\xi)^2(1-3\Delta\xi)-2-\tfrac{1}{2}K(\Delta\xi)^3\right]$$
$$+\nu(5)\left[1-K(\Delta\xi)^3\right]$$
$$+\nu(6)\left[-\tfrac{1}{2}K(\Delta\xi)^3\right]=0 \qquad \text{(D40)}$$

POINT 5 can be written

$$\frac{\nu(4)-2\nu(5)+\nu(6)}{(\Delta\xi)^2}+K\nu(5)[1-4\Delta\xi]$$
$$-K(\Delta\xi)\left[\tfrac{1}{2}\nu(5)+\tfrac{1}{2}\nu(6)\right]=0 \qquad \text{(D41)}$$

$$\nu(4)+\nu(5)\left[K(\Delta\xi)^2(1-4(\Delta\xi))-2-\tfrac{1}{2}K(\Delta\xi)^3\right]$$
$$+\nu(6)\left[1-\tfrac{1}{2}K(\Delta\xi)^3\right]=0 \qquad \text{(D42)}$$

Determination of eigenvalues $\nu(1)$, $\nu(2)$, $\nu(3)$, $\nu(4)$, $\nu(5)$ and $\nu(6)$ the coefficients are shown below

The analysis shown generates 5 unknowns and 5 equations

	ν(2)	ν(3)	ν(4)	ν(5)	ν(6)
	4	-1	0	0	0
2	$K(\Delta\xi)^2(1-\Delta\xi)$ $-2-\frac{1}{2}K(\Delta\xi)^3$	$1-K(\Delta\xi)^3$	$-K(\Delta\xi)^3$	$-K(\Delta\xi)^3$	$-\frac{1}{2}K(\Delta\xi)^3$
3	1	$K(\Delta\xi)^2(1-2\Delta\xi)$ $-2-\frac{1}{2}K(\Delta\xi)^3$	$1-K(\Delta\xi)^3$	$-K(\Delta\xi)^3$	$-\frac{1}{2}K(\Delta\xi)^3$
4	0	1	$K(\Delta\xi)^2(1-3\Delta\xi)$ $-2-\frac{1}{2}K(\Delta\xi)^3$	$1-K(\Delta\xi)^3$	$-\frac{1}{2}K(\Delta\xi)^3$
5	0	0	1	$K(\Delta\xi)^2(1-4\Delta\xi)$ $-2-\frac{1}{2}K(\Delta\xi)^3$	$1-\frac{1}{2}K(\Delta\xi)^3$

Using the eigenvalue approach with increasing number of steps gives the following:

The solution for six steps i.e. n = 6 is $K_{(n=6)} = 7.98$

The solution for six steps i.e. n = 21 is $K_{(n=21)} = 7.83$

$$K_1 = \frac{m_L g L_1^3}{EI} = 7.83 \qquad \text{(D43)}$$

From equation (D42) we obtain

$$L_1 = 1.99\left[\frac{EI}{m_L g}\right]^{1/3} \qquad \text{(D44)}$$

which is the length of the first buckled shape

To determine the second mode buckling, the next eigenvalue was determined as $K_2 = 55.8$

i.e. $$K_2 = \frac{m_L g(L_1 + L_2)^3}{EI} = 55.8 \qquad \text{(D45)}$$

$$\therefore (L_1 + L_2) = 55.8^{1/3}\left[\frac{EI}{m_L g}\right]^{1/3} = 3.82\left[\frac{EI}{m_L g}\right]^{1/3} \quad \text{(D46)}$$

$$\therefore L_2 = 3.82 - 1.99\left[\frac{EI}{m_L g}\right]^{1/3} = 1.84\left[\frac{EI}{m_L g}\right]^{1/3} \quad \text{(D47)}$$

Appendix E

This appendix contains solutions for lengths of individual buckled shapes (sinusoidal)

Appendix	Content
Appendix E	Calculation of lengths of buckled shapes L_1, L_2 & $L_{N>2}$ (sinusoidal)

Appendix E

Calculation of length of Buckled shapes L_1, L_2, & $L_{N>2}$. Buckling due to Own Weight

Following the analysis in appendix D the lengths of the buckled shapes are calculated below

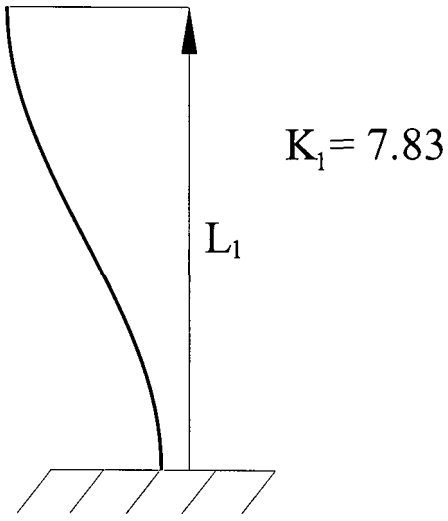

Figure Appendix E.1 First buckled shape

The first eigenvalue from Appendix D gave a value of $K_1 = 7.83$

$$\text{i.e}\frac{m_L g L_1^3}{EI} = 7.83 = K_1 \tag{E1}$$

$$L_1^3 = 7.83\frac{EI}{m_L g} \tag{E2}$$

$$L_1 = K_1^{\frac{1}{3}}\left[\frac{EI}{m_L g}\right]^{\frac{1}{3}} \tag{E3}$$

$$L_1 = 1.99\left[\frac{EI}{m_L g}\right]^{\frac{1}{3}} \tag{E4}$$

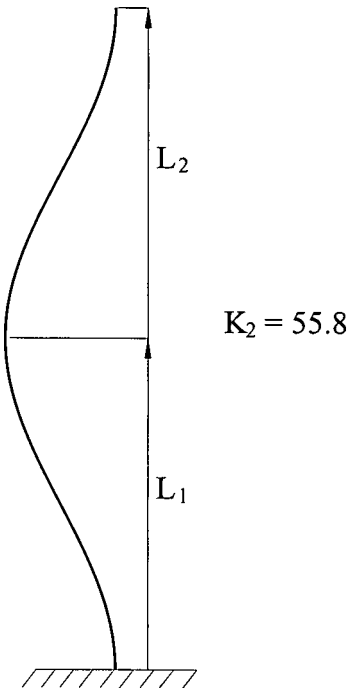

Figure Appendix E.2 First and second buckled shapes

Using the second eigenvalue of $K_2 = 55.8$

gives

$$\frac{m_L g(L_1 + L_2)}{EI} = 55.8 = K_2 \tag{E5}$$

$$(L_1 + L_2)^3 = K_2 \frac{EI}{m_L g} \tag{E6}$$

$$(L_1 + L_2) = K_2^{\frac{1}{3}} \left[\frac{EI}{m_L g}\right]^{\frac{1}{3}} \tag{E7}$$

$$\therefore L_2 = K_2^{\frac{1}{3}} \left[\frac{EI}{m_L g}\right]^{\frac{1}{3}} - L_1 \tag{E8}$$

$$L_2 = \left(K_2^{\frac{1}{3}} - K_1^{\frac{1}{3}}\right) \left[\frac{EI}{m_L g}\right]^{\frac{1}{3}} \tag{E9}$$

$$L_2 = 1.84 \left[\frac{EI}{m_L g}\right]^{\frac{1}{3}} \tag{E10}$$

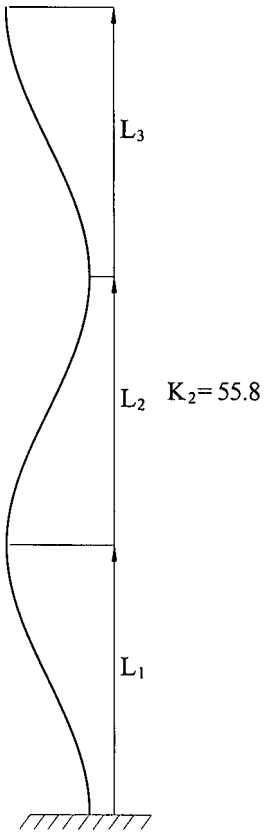

figure appendix E.3 First, second and third buckled shapes

Using the third eigenvalue of $K_2 = 147.4$

gives

$$\frac{m_L g(L_1 + L_2 + L_3)}{EI} = 147.4 = K_3 \tag{E11}$$

$$L_1 + L_2 + L_3 = K_3^{\frac{1}{3}}\left[\frac{EI}{m_L g}\right]^{\frac{1}{3}} \tag{E12}$$

$$L_3 = K_3^{\frac{1}{3}} - \left(K_2^{\frac{1}{3}} - K_1^{\frac{1}{3}}\right) - K_1^{\frac{1}{3}}\left[\frac{EI}{m_L g}\right]^{\frac{1}{3}} \tag{E13}$$

$$L_3 = \left(K_3^{\frac{1}{3}} - K_2^{\frac{1}{3}}\right)\left[\frac{EI}{m_L g}\right]^{\frac{1}{3}} \tag{E14}$$

$$L_3 = 1.46\left[\frac{EI}{m_L g}\right]^{\frac{1}{3}} \tag{E15}$$

Similarly $$K_4 = 281 \tag{E16}$$

hence $$L_4 = \left(K_4^{\frac{1}{3}} - K_3^{\frac{1}{3}}\right)\left[\frac{EI}{m_L g}\right]^{\frac{1}{3}} \tag{E17}$$

$$L_4 = 1.27\left[\frac{EI}{m_L g}\right]^{\frac{1}{3}} \tag{E18}$$

Appendix F

This appendix contains the buckling analysis, fixed-free with own weight and axial force

Appendix	Content
Appendix F	Buckling analysis, fixed-free with own weight and axial force

Appendix F
Buckling Analysis
Fixed-Free
Buckling with own Weight & Axial Force

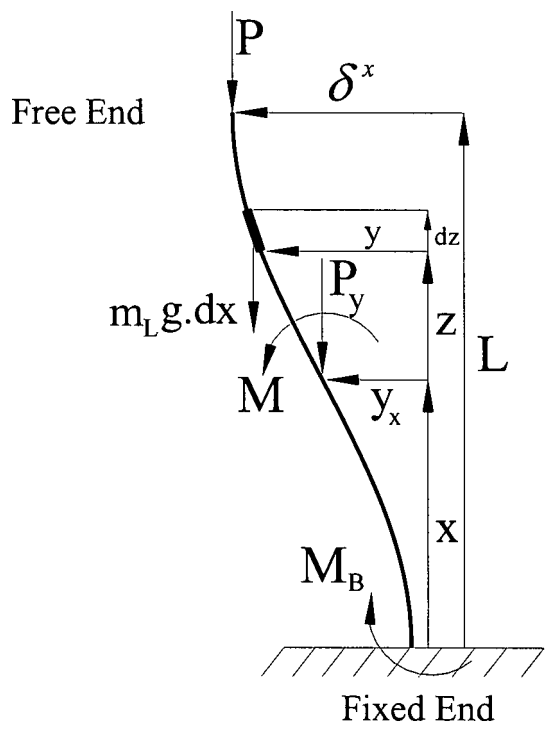

Figure Appendix F.1

The analysis here follows the basic approach as developed in appendix D, in this case the axial force *P* is considered. This will introduce an additional term for the bending moment.

For equilibrium the algebraic sum of forces and moments must be equal to zero.

$$\sum F = 0 \qquad \sum M = 0$$

$$M_B - P\delta^x - \int_x^L m_L g\, y dx = 0 \tag{F1}$$

$$M_B = P\delta^x + \int_x^L m_L g\, y dx \tag{F2}$$

Define axial forces

$$P_y = P + \left[m_L g(L - x)\right] \tag{F3}$$

$$M + P_y y - M_B = 0 \tag{F4}$$

$$M = -P_y y + M_B \tag{F5}$$

Substitute for M_B and P_y

$$M = -Py - [m_L g(L-x)]y + P\delta^x + \int_x^L m_L g\, y dx \tag{F6}$$

$$EI\frac{d^2y}{dx^2} + Py + m_L g(L-x)y - P\delta^x - m_L g\int_x^L y dx = 0 \tag{F7}$$

Alternatively

$$M = M_{end.force} + M_{self.weight} \tag{F8}$$

$$M_{end.force} = P(\delta^x - y) \tag{F9}$$

$$M_{self.weight} = m_L g\int_x^L y dz - m_L g\, y(L-x) \tag{F10}$$

$$M = P(\delta^x - y) + M_{self.weight} \tag{F11}$$

$$EI\frac{d^2y}{dx^2} = P(\delta^x - y) + M_{self.weight} \tag{F12}$$

$$EI\frac{d^2y}{dx^2} + Py - P\delta^x + m_L g\, y(L-x) - m_L g\int_x^L y dx = 0 \tag{F13}$$

$$EI\frac{d^2y}{dx^2} + Py + m_L g(L-x)y - P\delta^x - m_L g\int_x^L y dx = 0 \tag{F14}$$

To eliminate dimensions let

$$\xi = \frac{x}{L} \qquad x = L\xi \tag{F15}$$

$$\delta = \frac{\delta^x}{L} \qquad \therefore \delta^x = L\delta \tag{F16}$$

$$\nu = \frac{y}{L} \qquad \therefore y = L\nu \tag{F17}$$

Substitution for x, y, and δ^x gives

$$EI\frac{d^2L\nu}{L^2d\xi^2} + PL\nu + m_L g(L^2\nu - L^2\nu\xi) - PL\delta - m_L g\int_\xi^1 L^2\nu d\xi = 0 \tag{F18}$$

$$EI\frac{d^2\nu}{Ld\xi^2} + PL\nu + m_L g(L^2\nu - L^2\nu\xi) - PL\delta - m_L g\int_\xi^1 L^2\nu d\xi = 0 \tag{F19}$$

To arrive at first term being simple second order differential term multiply by $\frac{L}{EI}$

$$\frac{d^2v}{d\xi^2}+\frac{L}{EI}PLv+\frac{L}{EI}m_Lg\left(L^2v-L^2v\xi\right)-\frac{L}{EI}PL\delta-\frac{L}{EI}m_Lg\int_{\xi}^{1}L^2vd\xi=0 \quad \text{(F20)}$$

Simplify

$$\frac{d^2v}{d\xi^2}+\frac{L}{EI}PLv+\frac{L}{EI}m_LgL^2v(1-\xi)-\frac{L}{EI}PL\delta-\frac{L}{EI}m_LgL^2\int_{\xi}^{1}vd\xi=0 \quad \text{(F21)}$$

$$\frac{d^2v}{d\xi^2}+\frac{PL^2}{EI}v+\frac{L^3}{EI}m_Lgv(1-\xi)-\frac{PL^2}{EI}\delta-\frac{L^3}{EI}m_Lg\int_{\xi}^{1}vd\xi=0 \quad \text{(F22)}$$

$$\frac{d^2v}{d\xi^2}+\frac{PL^2}{EI}v+\frac{L^3m_Lg}{EI}v(1-\xi)-\frac{PL^2}{EI}\delta-\frac{L^3m_Lg}{EI}\int_{\xi}^{1}vd\xi=0 \quad \text{(F23)}$$

Putting

$$K=\frac{m_LgL^3}{EI} \quad \text{(F24)}$$

$$B=\frac{PL^3}{EI} \quad \text{(F25)}$$

Gives

$$\frac{d^2v}{d\xi^2}+Bv+Kv(1-\xi)-B\delta-K\int_{x}^{L}vd\xi=0 \quad \text{(F26)}$$

$$\frac{d^2v}{d\xi^2}+Bv-B\delta+Kv(1-\xi)-K\int_{x}^{L}vd\xi=0 \quad \text{(F27)}$$

Boundary conditions

$$\xi=0 \qquad v=0 \quad \text{(F28)}$$

$$\xi=0 \qquad \frac{dv}{d\xi}=0 \quad \text{(F29)}$$

Formulation of equations to obtain eigenvalues

The general finite difference analysis is demonstrated on a six point, five interval system, shown below:

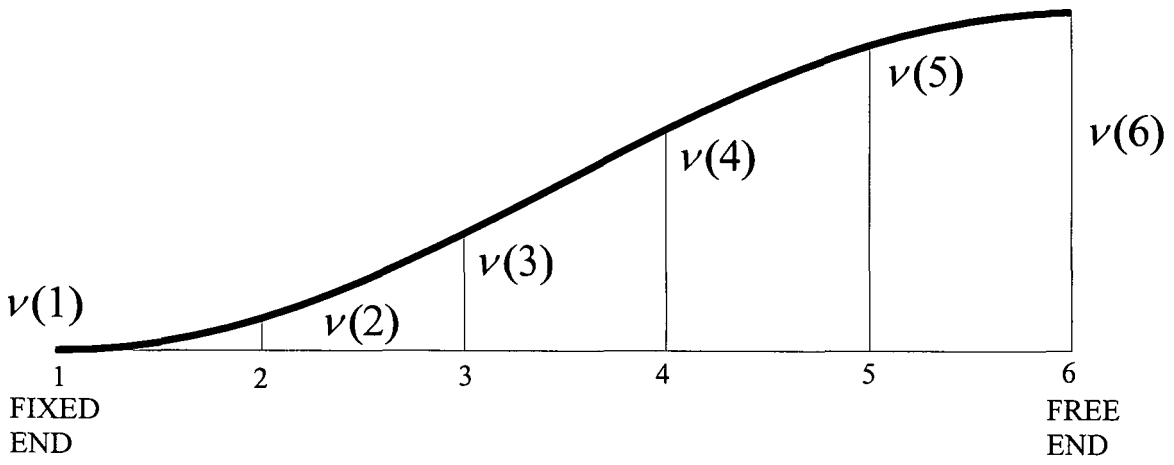

Development of the first equation (Using a forward second order approximation)

As the first 3 points are considered to conform to a parabola, the deflections can be expressed in terms of the interval lengths, applying the end conditions

$$\nu(1) = 0 \qquad \text{(F30)}$$

$$\frac{d\nu}{d\xi} = 0 \quad \text{at} \quad \xi = 0 \qquad \text{(F31)}$$

produces $$4\nu(2) - \nu(3) = 0 \qquad \text{(F32)}$$

$m =$ any point — in the above case $m = 6$

$n =$ number of segments — where in the above case $(n) = 5$

$\therefore (n+1) = 6$, which is the end point

POINT 2 can be written as

$$\frac{v(m-1)-2v(m)+v(m+1)}{(\Delta\xi)^2}+Bv(m)-Bv(n+1)$$
$$+Kv(m)[1-\xi(m)]$$
$$-K(\Delta\xi)\left[\tfrac{1}{2}v(m)+v(m+1)+.....v(n)+\tfrac{1}{2}v(n+1)\right]=0 \quad \text{(F33)}$$

$$v(m-1)-2v(m)+v(m+1)+B(\Delta\xi)^2v(m)-B(\xi)^2v(n+1)$$
$$+K(\xi)^2[1-\xi(m)]v(m)$$
$$-K(\Delta\xi)^3\left[\tfrac{1}{2}v(m)+v(m+1)+.....v(n)+\tfrac{1}{2}v(n+1)\right]=0 \quad \text{(F34)}$$

The above equation is the general case for any point except 1 (start point)
For point (1) we use the boundary conditions

$\frac{dy}{dx}=0$ at $x=0$

As on page D4, the first equation is :-
$4v(2)-v(3)=0$

POINT 3 can be written as

$m=2$ (remembering that $v(1)=0$)

$$-2v(2)+v(3)B(\Delta\xi)^2v(2)-B(\Delta\xi)^2v(n+1)$$
$$+K(\Delta\xi)^2[1-\xi(2)]v(2)$$
$$-K(\Delta\xi)^3\left[\tfrac{1}{2}v(2)+v(3)+v(2)+....v(n)+\tfrac{1}{2}v(n+1)\right]=0 \quad \text{(F35)}$$

Extract coefficients for $v(2) etc..v(n+1)$

$$v(2)\left[K(\Delta\xi)^2\{1-\Delta\xi\}-2+B(\Delta\xi)^2\,\tfrac{1}{2}K(\Delta\xi)^3\right]$$
$$+v(3)\left[1-K(\Delta\xi)^3\right]$$
$$+v(4)\left[-K(\Delta\xi)^3\right]$$

.
.
.

$$+v(n)\left[-K(\Delta\xi)^3\right]$$

$$v(n+1)\left[-B(\Delta\xi)^2 - \tfrac{1}{2}K(\Delta\xi)^3\right] = 0 \qquad \text{(F36)}$$

POINT 4 can be written as

$2 < m < n$

$$v(m-1)[1]$$

$$v(m)\left[K(\Delta\xi)^2\{1-(m-1)\Delta\xi\} + B(\Delta\xi)^2 - 2 - \tfrac{1}{2}K(\Delta\xi)^3\right]$$
$$+ v(m+1)\left[1 - K(\Delta\xi)^2\right]$$
$$+ v(m+2)\left[-K(\Delta\xi)^2\right]$$

.
.
.

$$+ v(n)\left[-K(\Delta\xi)^2\right]$$
$$v(n+1)\left[-B(\Delta\xi)^2 - \tfrac{1}{2}K(\Delta\xi)^3\right] = 0 \qquad \text{(F37)}$$

POINT 5 can be written as

$m = n$

$$v(n-1)[1]$$
$$v(n)\left[K(\Delta\xi)^2\{1-(n-1)\Delta\xi\} + B(\Delta\xi)^2 - 2 - \tfrac{1}{2}K(\Delta\xi)^3\right]$$
$$v(n+1)\left[1 - B(\Delta\xi)^2 - \tfrac{1}{2}K(\Delta\xi)^3\right] = 0 \qquad \text{(F38)}$$

We have 5 unknowns and 5 equations

	ν(2)	ν(3)	ν(4)	ν(5)	ν(6)
	4	-1	0	0	0
2	$K(\Delta\xi)^2(1-\Delta\xi)$ $-2+B(\Delta\xi)^2-\frac{1}{2}K(\Delta\xi)^3$	$1-K(\Delta\xi)^3$	$-K(\Delta\xi)^3$	$-K(\Delta\xi)^3$	$B(\Delta\xi)^2-\frac{1}{2}K(\Delta\xi)^3$
3	1	$K(\Delta\xi)^2(1-2\Delta\xi)$ $-2+B(\Delta\xi)^2-\frac{1}{2}K(\Delta\xi)^3$	$1-K(\Delta\xi)^3$	$-K(\Delta\xi)^3$	$-\frac{1}{2}K(\Delta\xi)^3$
4	0	1	$K(\Delta\xi)^2(1-3\Delta\xi)$ $-2+B(\Delta\xi)^2-\frac{1}{2}K(\Delta\xi)^3$	$1-K(\Delta\xi)^3$	$-\frac{1}{2}K(\Delta\xi)^3$
5	0	0	1	$K(\Delta\xi)^2(1-4\Delta\xi)$ $-2+B(\Delta\xi)^2-\frac{1}{2}K(\Delta\xi)^3$	$1-\frac{1}{2}K(\Delta\xi)^3$

An array has been set up on Excel spread sheet fixed/free = own weight + axial force where $n = 21$.

The dimensionless constants

$$K = \frac{m_L g L^3}{EI} \tag{F30}$$

is a measure self weight

and

$$B = \frac{PL^2}{EI} \tag{F31}$$

is a measure of axial end force

By setting B to zero (effectively zero end force) and using goal seek tool setting the determinant of the array to zero by selecting the appropriate value of K gave a result of K= 7.832. This is corresponds to the value derived by analytical means.

By setting K to zero (effectively zero self weight) and using goal seek tool setting the determinant of the array to zero by selecting the appropriate value of B gave a result of $B = 2.465$. This is corresponds to the value of $\left(\frac{\pi^2}{4}\right)$ derived by analytical means.

Appendix G

This appendix contains reaction forces during sinusoidal buckling

Appendix	Content
Appendix G	Reaction forces during sinusoidal buckling

Appendix G

Reaction Forces during Sinusoidal Buckling

Reaction force in fixed, sliding-fixed arrangement

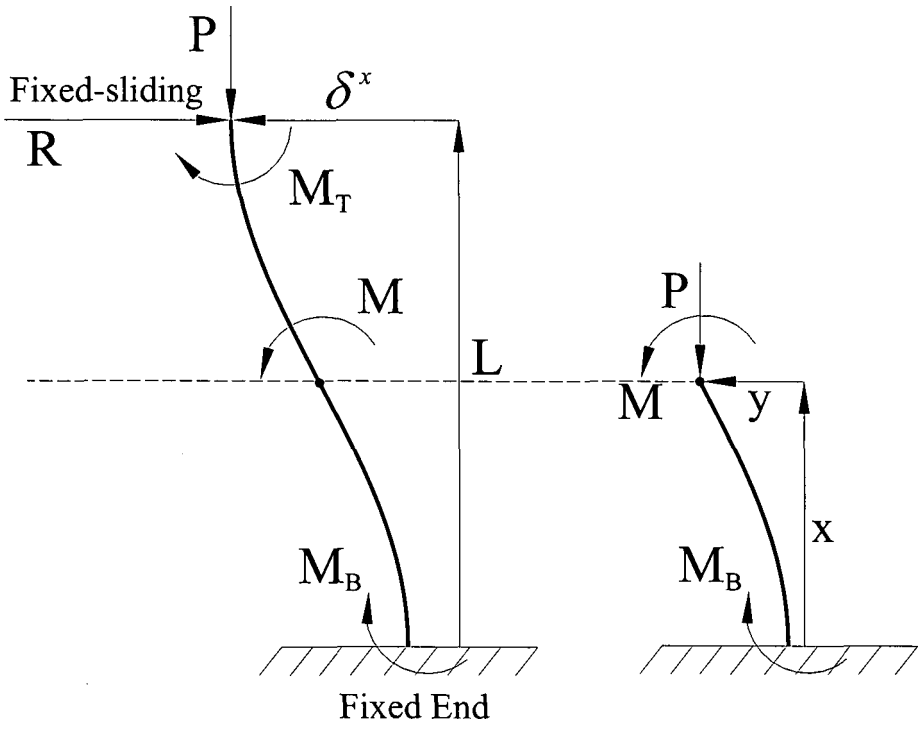

Figure Appendix G.1 Vertical Column with end force and reaction force

The governing equation is

$$EI\frac{d^2y}{dx^2} = M \tag{G1}$$

The bending moment

$$M = P(\delta^x - y) - R(L - x) - M_T \tag{G2}$$

$$M = -Py + P\delta^* - R(L - x) - M_T \tag{G3}$$

Hence

$$EI\frac{d^2y}{dx^2} = -Py + P\delta^* - R(L - x) - M_T \tag{G4}$$

Which can be simplified by dividing by $\dfrac{1}{EI}$

$$\frac{d^2y}{dx^2} + = -\frac{Py}{EI} + \frac{P}{EI}\delta^* - \frac{R}{EI}(L-x) - \frac{M_T}{EI} \tag{G5}$$

$$\frac{d^2y}{dx^2} + k^2 y = \frac{P}{EI}\delta^* - \frac{R}{EI}(L-x) - \frac{M_T}{EI} \tag{G6}$$

For $$k^2 = \frac{P}{EI} \tag{G7}$$

The general solution of equation (G6) is

$$y = y_H + y_P \tag{G8}$$

where in (G8) the solution of differential equation, *y*, is equal to the sum of homogeneous solution y_H and particular solution y_P, with y_H being the solution of

$$\frac{d^2y_H}{dx^2} + k^2 y_H = 0 \tag{G9}$$

where

$$y_H = C_1 \sin kx + C_2 \cos kx \tag{G10}$$

Substitute (G8) into (G6)

$$\frac{d^2(y_H + y_P)}{dx^2} + k^2(y_H + y_P) = \frac{P}{EI}\delta^* - \frac{R}{EI}(L-x) - \frac{M_T}{EI} \tag{G11}$$

and using equation (G9) we obtain the equation for the particular solution y_P

$$\frac{d^2y_p}{dx^2} + k^2 y_p = \frac{P}{EI}\delta^* - \frac{R}{EI}(L-x) - \frac{M_T}{EI} \tag{G12}$$

Since the right hand side of equation (G12) is a polynomial of the first order

$$y_P = A + Bx \tag{G13}$$

$$\frac{dy_P}{dx} = B \tag{G14}$$

$$\frac{d^2y_P}{dx^2} = 0 \tag{G15}$$

Therefore from equation (G12) we have

$$k^2 y_P = \frac{P}{EI}\delta^* - \frac{R}{EI}(l-x) - \frac{M_T}{EI} \tag{G16}$$

and where y_P is the particular solution, which after division by $k^2 = \frac{P}{EI}$ is given by

$$y_P = \delta^* - \frac{R}{P}(L-x) - \frac{M_T}{P} \tag{G17}$$

Hence

$$y = C_1 \sin(kx) + C_2 \cos(kx) + \delta^* - \frac{R}{P}(L-x) - \frac{M_T}{P} \tag{G18}$$

and

$$\frac{dy}{dx} = C_1 k \cos(kx) - C_2 k \sin(kx) + \frac{R}{P} \tag{G19}$$

Equation (G18) contains four unknowns, C_1, C_2, R and M_T, and hence we need four boundary conditions. These are:

$$x = 0 \qquad y = 0 \tag{G20}$$

$$x = 0 \qquad \frac{dy}{dx} = 0 \tag{G21}$$

$$x = L \qquad y = \delta^* \tag{G22}$$

$$x = L \qquad \frac{dy}{dx} = 0 \tag{G23}$$

Boundary conditions in equations (G20-G23) can be re-written respectively as

$$B + \delta^* - \frac{R}{P}L - \frac{M_T}{P} = 0 \tag{G24}$$

$$Ak + \frac{R}{P} = 0 \tag{G25}$$

$$C_1 \sin(kL) + C_2 \cos(kL) - \frac{M_T}{P} = 0 \tag{G26}$$

$$C_1 k\cos(kL) - C_2 k\sin(kL) + \frac{R}{P} = 0 \qquad \text{(G27)}$$

From equation (G25)

$$C_1 = -\frac{R}{kP} \qquad \text{(G28)}$$

Substituting equation (G28) into equation (G27) we get

$$-\frac{R}{kP} k\cos(kL) - C_2 k\sin(kL) + \frac{R}{P} = 0 \qquad \text{(G29)}$$

and hence

$$C_2 = \frac{R}{kP}\frac{1-\cos(kL)}{\sin(kL)} \qquad \text{(G30)}$$

Substituting equations (G28) into equation (G24) we get

$$\frac{R}{kP}\frac{1-\cos(kL)}{\sin(kL)} + \delta^* - \frac{R}{P}L - \frac{M_T}{P} = 0 \qquad \text{(G31)}$$

and hence

$$\frac{M_T}{P} = \delta^* + \frac{R}{kP}\left(\frac{1-\cos(kL)}{\sin(kL)} - kl\right) \qquad \text{(G32)}$$

Substituting equations (G28), (G30) and (G32) into equation (G26) we get

$$-\frac{R}{kP}\sin(kL) + \frac{R}{kP}\frac{1-\cos(kL)}{\sin(kL)}\cos(kL) - \delta^* - \frac{R}{kP}\left(\frac{1-\cos(kL)}{\sin(kL)} - kL\right) = 0 \qquad \text{(G33)}$$

and hence

$$\frac{R}{P} = \frac{kL\sin(kL)}{2[\cos(kL)-1] + kl\sin(kL)}\frac{\delta^*}{L} \qquad \text{(G34)}$$

which can be re-written as

$$\frac{R}{P}\frac{l}{\delta^*} = \frac{kl\sin(kL)}{2[\cos(kL)-1]+kl\sin(kL)} \tag{G35}$$

and the variation of $RL/P\delta^x$ as the function of kL can be obtained.

Furthermore, it can be shown that the buckling occurs for

$$kL = \pi \tag{G36}$$

and since

$$\sin\pi = 0 \tag{G37}$$

equation (35) shows that when buckling occurs

$$R = 0 \tag{G38}$$

Hence when buckling occurs, reaction R equals to zero.

Appendix H

This appendix contains the buckling analysis, fixed, sliding-fixed with own weight and axial force

Appendix	Content
Appendix H	Buckling analysis, fixed, sliding-fixed with own weight and axial force

Appendix H
Buckling Analysis
Fixed, Sliding-Fixed
Buckling with own Weight & Axial End Force

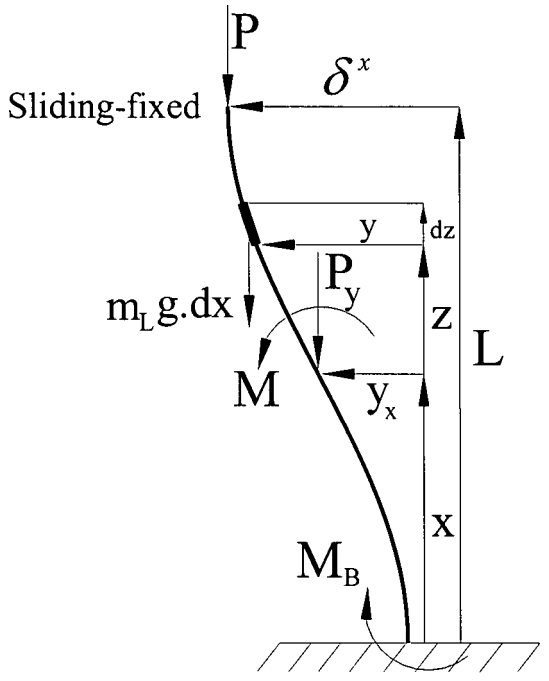

Figure Appendix H.1

The analysis here follows the basic approach as developed in appendix F, except in this case the boundary conditions at $x = L$ have changed, it is now a sliding-fixed condition.

For equilibrium the algebraic sum of forces and moments must be equal to zero.

$$\sum F = 0 \qquad \sum M = 0$$

$$M_B + M_T - P\delta^x \int_x^L m_L g y dx = 0 \tag{H1}$$

$$M_B = P\delta^x + \int_x^L m_L g\, y dx - M_T \tag{H2}$$

Define axial forces

$$P_y = P + \left[m_L g(L - x)\right] \tag{H3}$$

$$M + P_y y - M_B = 0 \Rightarrow M = -P_y y + M_B \tag{H4}$$

Substitute for M_B and P_y

$$M = -Py - [m_L g(L-x)]y + P\delta^x + \int_x^L m_L g\, y dz - M_T \qquad \text{(H5)}$$

$$EI\frac{d^2y}{dx^2} = M \qquad \text{(H6)}$$

$$EI\frac{d^2y}{dx^2} + Py + m_L g(L-x)y - P\delta^x - m_L g\int_x^L y dz + M_T = 0 \qquad \text{(H7)}$$

$$\xi = \frac{x}{L} \qquad x = L\xi \qquad \text{(H8)}$$

$$\delta = \frac{\delta^x}{L} \qquad \therefore \delta^x = L\delta \qquad \text{(H9)}$$

$$\nu = \frac{y}{L} \qquad \therefore y = L\nu \qquad \text{(H10)}$$

To convert M_T to be dimensionless multiply by $\frac{L}{EI}$

$$\therefore A = \frac{M_T L}{EI} \qquad \text{(H11)}$$

Substitution for x, y and δ^x gives

$$EI\frac{d^2L\nu}{d(L\xi)^2} + PL\nu + m_L g(L-L\xi)L\nu - PL\delta - m_L g\int_{L\xi}^L L\nu dL\xi + A = 0 \qquad \text{(H12)}$$

$$EI\frac{d^2L\nu}{L^2 d\xi^2} + PL\nu + m_L g\left(L^2\nu - L^2\nu\xi\right) - PL\delta - m_L g\int_\xi^1 L^2\nu d\xi + A = 0 \qquad \text{(H13)}$$

$$EI\frac{d^2\nu}{Ld\xi^2} + PL\nu + m_L g\left(L^2\nu - L^2\nu\xi\right) - PL\delta - m_L g\int_\xi^1 L^2\nu d\xi + A = 0 \qquad \text{(F14)}$$

To arrive at first term being simple second order differential term multiply by $\frac{L}{EI}$

$$\frac{d^2\nu}{d\xi^2} + \frac{L}{EI}PL\nu + \frac{L}{EI}m_L g\left(L^2\nu - L^2\nu\xi\right) - \frac{L}{EI}PL\delta - \frac{L}{EI}m_L g\int_\xi^1 L^2\nu d\xi + u = 0 \qquad \text{(H15)}$$

Simplify

$$\frac{d^2\nu}{d\xi^2} + \frac{L}{EI}PL\nu + \frac{L}{EI}m_L gL^2\nu(1-\xi) - \frac{L}{EI}PL\delta - \frac{L}{EI}m_L gL^2\int_\xi^1 \nu d\xi + A = 0 \qquad \text{(H16)}$$

$$\frac{d^2v}{d\xi^2}+\frac{PL^2}{EI}v+\frac{L^3}{EI}m_L g v(1-\xi)-\frac{PL^2}{EI}\delta-\frac{L^3}{EI}m_L g\int_{\xi}^{1} v d\xi + A = 0 \qquad \text{(H17)}$$

Putting
$$K=\frac{m_L g L^3}{EI} \qquad \text{(H18)}$$

and
$$B=\frac{PL^2}{EI} \qquad \text{(H19)}$$

$$\frac{d^2v}{d\xi^2}+Bv+Kv(1-\xi)-B\delta-K\int_{x}^{L} v d\xi + A = 0 \qquad \text{(H20)}$$

$$\frac{d^2v}{d\xi^2}+Bv-B\delta+Kv(1-\xi)-K\int_{x}^{L} v d\xi + A = 0 \qquad \text{(H21)}$$

Boundary conditions

$$\xi = 0 \qquad v = 0 \qquad \text{(H22)}$$

$$\frac{dv}{d\xi}=0 \qquad \text{(F23)}$$

$$\xi = 1 \qquad \frac{dv}{d\xi}=0 \qquad \text{(H24)}$$

Formulation of equations to obtain eigenvalues

The general finite difference analysis is demonstrated on a six point, five interval system, shown below:

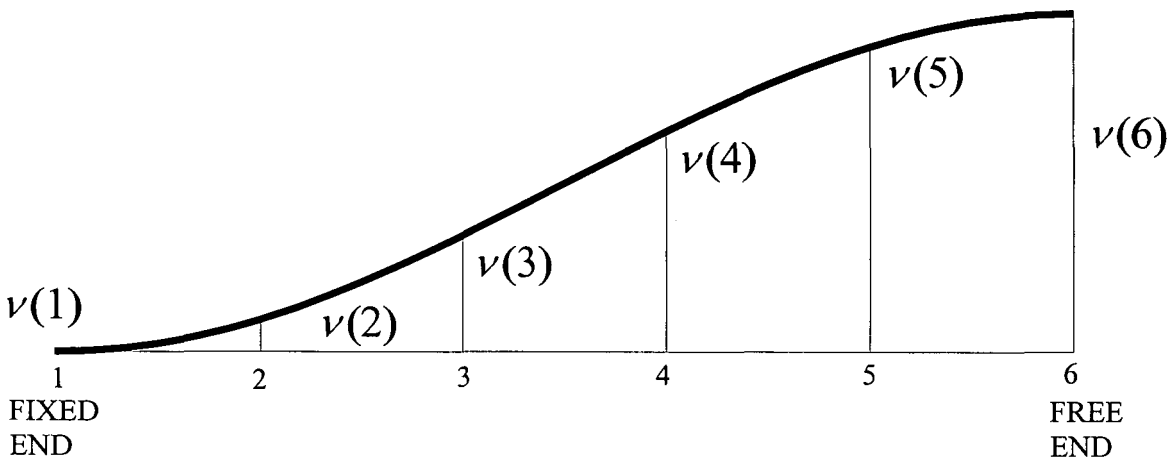

Development of the first equation (Using a forward second order approximation)

As the first 3 points are considered to conform to a parabola, the deflections can be expressed in terms of the interval lengths, applying the end conditions

$$\nu(1) = 0 \tag{H25}$$

$$\frac{d\nu}{d\xi} = 0 \quad \text{at} \quad \xi = 0 \tag{H26}$$

produces for **POINT 1** $$4\nu(2) - \nu(3) = 0 \tag{H27}$$

For any inside point, the finite difference equation can be similarly written as

$$\frac{v(m-1)-2v(m)+v(m+1)}{(\Delta\xi)^2}+Bv(m)-Bv(n+1)$$
$$+Kv(m)[1-\xi(m)]$$
$$-K(\Delta\xi)\left[\tfrac{1}{2}v(m)+v(m+1)+..v(n)+\tfrac{1}{2}v(n+1)\right]+A=0 \quad \text{(H28)}$$

which can be re-arranged as

$$v(m-1)-2v(m)+v(m+1)+B(\Delta\xi)^2v(m)-B(\xi)^2v(n+1)$$
$$+K(\xi)^2[1-\xi(m)]v(m)$$
$$-K(\Delta\xi)^3\left[\tfrac{1}{2}v(m)+v(m+1)+..v(n)+\tfrac{1}{2}v(n+1)\right]+(\Delta\xi)^2A=0$$

(H29)

POINT 2 ($m = 2$) can be obtained from equation (H29) as

$$-2v(2)+v(3)+B(\Delta\xi)^2v(2)-B(\Delta\xi)^2v(6)$$
$$+K(\Delta\xi)^2[1-\xi(2)]v(2)$$
$$-K(\Delta\xi)^3\left[\tfrac{1}{2}v(2)+v(3)+v(4)+v(5)+\tfrac{1}{2}v(6)\right]+(\Delta\xi)^2A=0 \text{ (H30)}$$

Extract coefficients for $v(2)etc$

$$v(2)\left[K(\Delta\xi)^2\{1-\Delta\xi\}-2+B(\Delta\xi)^2\tfrac{1}{2}K(\Delta\xi)^3\right]$$
$$+v(3)\left[1-K(\Delta\xi)^3\right]$$
$$+v(4)\left[-K(\Delta\xi)^3\right]$$
$$+v(5)\left[-K(\Delta\xi)^3\right]$$
$$+v(6)\left[-B(\Delta\xi)^2-\tfrac{1}{2}K(\Delta\xi)^3\right]$$
$$+A\left[(\Delta\xi)^2\right]=0 \quad \text{(H31)}$$

POINTS 3, 4 and **5** can be similarly described

We have 6 unknowns and 6 equations

	ν(2)	ν(3)	ν(4)	ν(5)	ν(6)	A
	4	-1	0	0	0	0
2	$\frac{K(\Delta\xi)^2(1-\Delta\xi)}{-2+B(\Delta\xi)^2-\frac{1}{2}K(\Delta\xi)^3}$	$1-K(\Delta\xi)^3$	$-K(\Delta\xi)^3$	$-K(\Delta\xi)^3$	$-B(\Delta\xi)^2-\frac{1}{2}K(\Delta\xi)^3$	$(\Delta\xi)^2$
3	1	$\frac{K(\Delta\xi)^2(1-2\Delta\xi)}{-2+B(\Delta\xi)^2-\frac{1}{2}K(\Delta\xi)^3}$	$1-K(\Delta\xi)^3$	$-K(\Delta\xi)^3$	$-B(\Delta\xi)^2-\frac{1}{2}K(\Delta\xi)^3$	$(\Delta\xi)^2$
4	0	1	$\frac{K(\Delta\xi)^2(1-3\Delta\xi)}{-2+B(\Delta\xi)^2-\frac{1}{2}K(\Delta\xi)^3}$	$1-K(\Delta\xi)^3$	$-B(\Delta\xi)^2-\frac{1}{2}K(\Delta\xi)^3$	$(\Delta\xi)^2$
5	0	0	1	$\frac{K(\Delta\xi)^2(1-4\Delta\xi)}{-2+B(\Delta\xi)^2-\frac{1}{2}K(\Delta\xi)^3}$	$1-(\Delta\xi)^2-\frac{1}{2}K(\Delta\xi)^3$	$(\Delta\xi)^2$
6	0	0	1	-4	3	0

An array has been set up on Excel spread sheet fixed/free = own weight + axial end force where $n = 21$.

The dimensionless constants

$$K = \frac{m_L g L^3}{EI} \tag{H32}$$

is a measure self weight

$$B = \frac{PL^2}{EI} \tag{H33}$$

is a measure of axial end force

$$A = \frac{M_T L}{EI} \tag{H34}$$

is a measure of moment at fixed sliding part

By setting B to zero (effectively zero end force) and using goal seek tool setting the determinant of the array to zero by selecting the appropriate value of K gave a result of K= 18.95.

By setting K to zero (effectively zero self weight) and using goal seek tool setting the determinant of the array to zero by selecting the appropriate value of B gave a result of B = 9.85. This is corresponds to the value of π^2 derived by analytical means.

However, both K and B contain the length L, which causes some difficulties when trying to determine the length. Hence we need to obtain another parameter, which does not contain the length L. Since the parameter B is proportional to L^2 and the parameter K is proportional to L^3, the ratio B^3/L^2 will not contain the length L

Hence the parameter

$$\frac{B^3}{K^2} = \frac{P^3}{(m_L g)^2 EI} \tag{H35}$$

does not contain the length.

The graph of B versus B^3/K^2 is shown and hence L can be obtained.

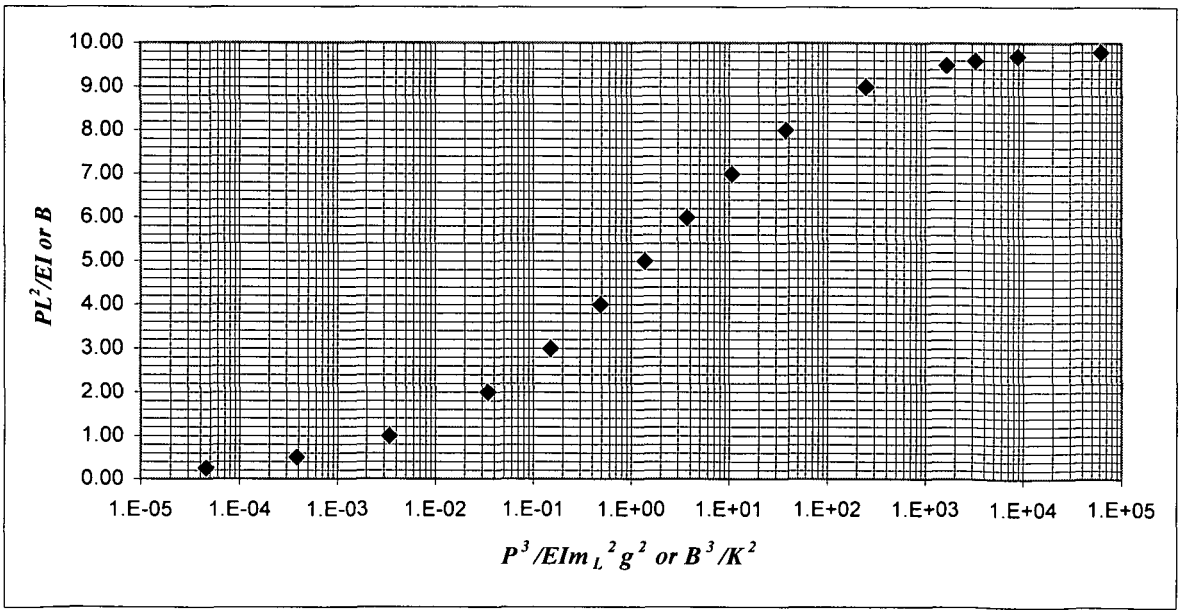

Hence for a given $\dfrac{P^3}{EI\left(m_L g^2\right)}$, L can be calculated.

Further consideration of the relationship between

$$B = \frac{PL^2}{EI\left(m_L g\right)^2} \tag{H36}$$

and

$$\frac{B^3}{K^2} = \frac{P^3}{\left(m_L g\right)^2 EI} \tag{H37}$$

First buckled form is due to its own weight only. Buckling will obtain when the fixed-free configuration buckles, which takes place, as shown above, for

$$\frac{m_L g L_1^{\ 2}}{EI} = 7.83 \tag{H38}$$

Hence the equivalent end force on the first fixed-sliding member will be

$$P = m_L g L_1 \tag{H39}$$

cube both sides

$$P^3 = m_L^{\ 3} g^3 L_1^{\ 3} \tag{H40}$$

Divide by $m_L g^2$

$$\frac{P^3}{m_L^{\ 2} g^2} = m_L g L_1^{\ 3} \tag{H41}$$

Divide by EI

$$\frac{P^3}{m_L^{\ 2} g^2 EI} = \frac{m_L g L_1^{\ 3}}{EI} = 7.83 \tag{H42}$$

and hence

$$\frac{P^3}{EI\left(m_L^2 g^2\right)} \geq 7.83 \tag{H43}$$

The end force on the subsequent members will be greater

$$\therefore \frac{B^3}{K^2} \geq 7.83 \tag{H44}$$

The relationship between $\dfrac{P^3}{EI\left(m_L g^2\right)}$ and B is shown below

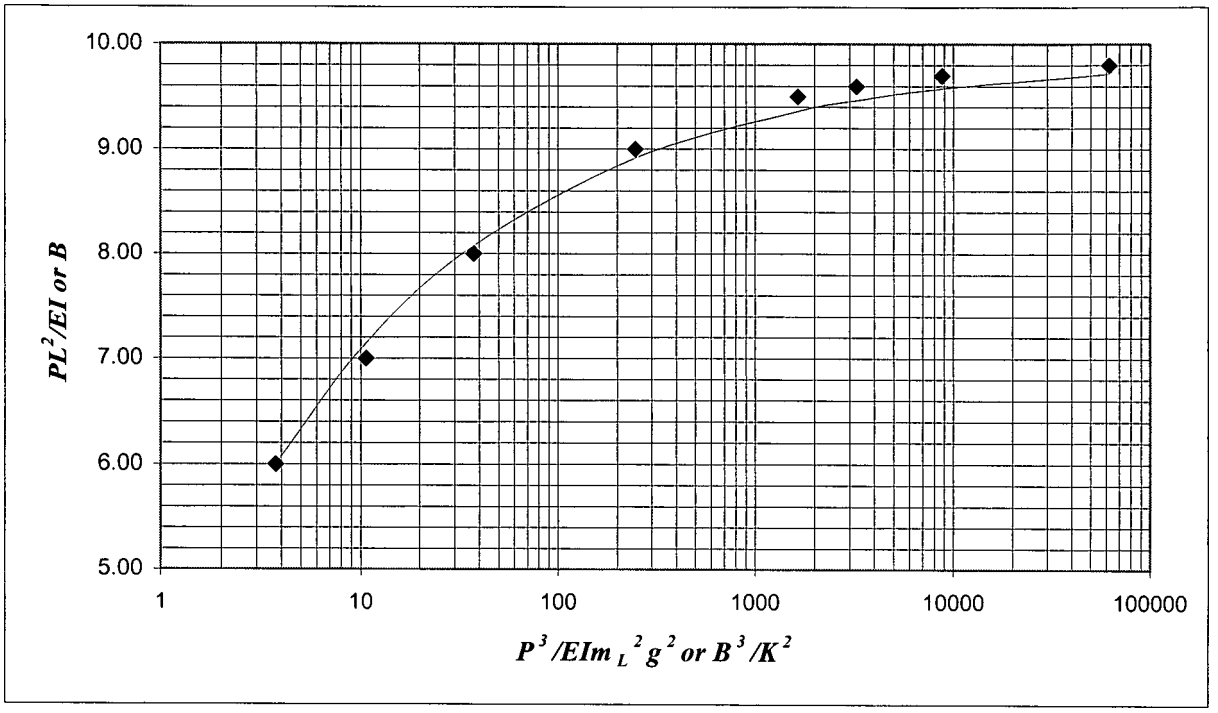

For $\dfrac{P^3}{EI\left(m_L g^2\right)} \geq 7.83$ this can be approximated with an error less than 2% as

$$\frac{PL^2}{EI} = \pi^2 - \left[\frac{EI\left(m_L g\right)^2}{P^3}\right]^{\left(\frac{1}{3}\right)} \tag{H45}$$

which is shown as the solid line in the above figure.

Hence, L can be calculated as follows:

$$L = \pi\left(\frac{EI}{P}\right)^{1/2}\left[1 - \frac{6}{\pi^2}\left[\frac{EI\left(m_L g\right)^2}{P^3}\right]^{1/3}\right]^{1/6} \tag{H46}$$

Appendix I

This appendix contains the helical buckling analysis.

Appendix	Content
Appendix I	Helical buckling analysis

Appendix I

Helical Buckling Analysis

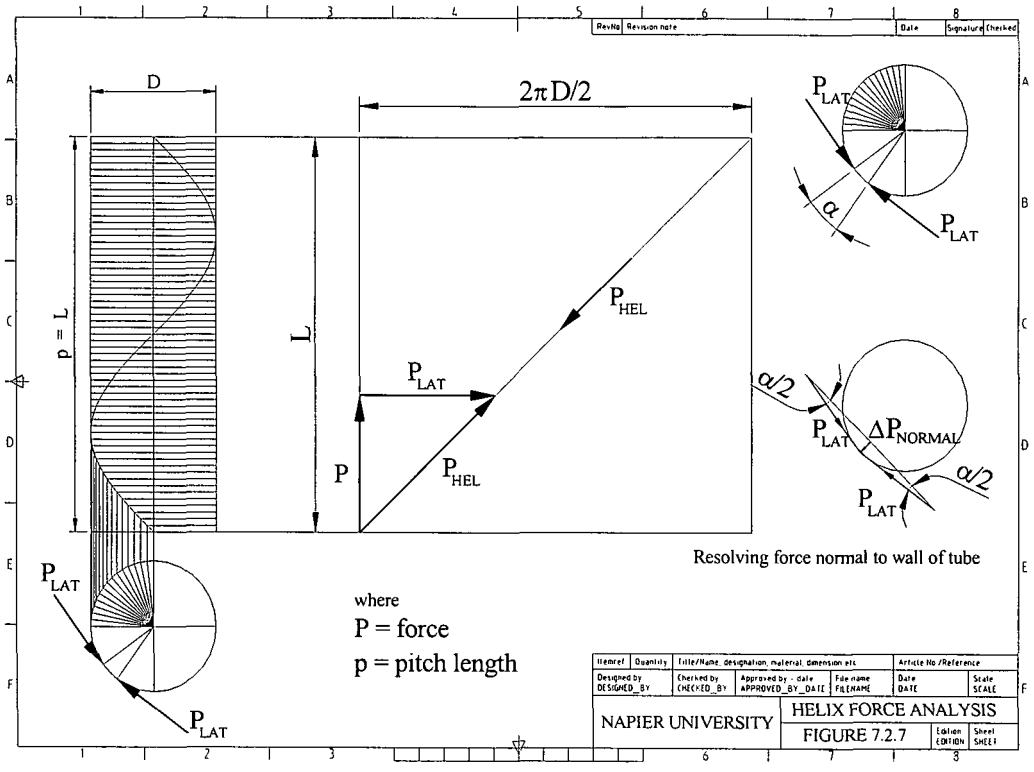

Figure Appendix I.1

From similar triangles

$$\frac{P_H}{P} = \frac{\left[\left(2\pi\frac{D}{2}\right)^2 + L^2\right]^{\frac{1}{2}}}{L} = \left[\left(\frac{2\pi\frac{D}{2}}{L}\right)^2 + 1\right]^{\frac{1}{2}} \qquad \text{(I.1)}$$

if $L = p$ .. pitch

$$\frac{P_H}{P} = \left[\left(\frac{\pi D}{p}\right)^2 + 1\right]^{\frac{1}{2}} \qquad \text{(I.2)}$$

$$\therefore P_H = P\left[\left(\frac{\pi D}{p}\right)^2 + 1\right]^{\frac{1}{2}} \tag{I.3}$$

$$\frac{P_L}{P} = \frac{\pi D}{L} \tag{I.4}$$

$$\therefore P_L = \frac{\pi D}{L} P \tag{I.5}$$

$$P_L = \frac{\pi D}{p} P \tag{I.6}$$

Refer to Figure I.1.

Take a very small angle α and calculate the force normal to the inner wall of the tube

$$\Delta P_N = P_L \sin\frac{\alpha}{2} \tag{I.7}$$

since there are forces from both directions

$$\Delta P_N = 2P_L \sin\frac{\alpha}{2} \tag{I.8}$$

and as $\frac{\alpha}{2}$ is very small

$$\Delta P_N = P_L \alpha \tag{I.9}$$

all of these forces must be added up over 2π

$$\therefore P_N = 2\pi P_L \tag{I.10}$$

Hence the total force is

$$\therefore P_N = 2\pi P_L = 2\pi.\pi \frac{D}{p} P = 2\pi^2 \frac{D}{p} P \tag{I.11}$$

Appendix J

This appendix contains the excel model for predicting insertion length.

Appendix	Content
Appendix J	Excel model – program listing

Appendix J

A detailed description of the actual excel model is given below.

1 Input basic data

shape	rod	eg
material	rubber	
d	m	0.003
D	m	0.013
t	m	n/a
E	N/m^2	2.50E+07
μ	[-]	1
□	kg/m^3	1373
g	m/s^2	9.81

2 Calculate input parameters

m_L	kg/m	0.0097	
I	m^4	3.97E-12	
P_{CR}	N	0.122991	transition force to helical
L_{CR}	mm	1292	transition length to helical
L_{TOT}	mm	1500	total penetration
hel	%	14	fraction of helical penetration

where

$$P_{CR} = 2^{1.5}\left(\frac{EIgm_L}{0.5(D-d)}\right)^{1/2} \tag{J.1}$$

$$L_{CR} = \frac{P_{CR}}{\mu g m_L} \tag{J.2}$$

and to be multiplied by 1000 to convert to mm

3 Enter description line

N L_N [m] L_{Tot} [mm] $P_{N,SIN}$ [N] mode flag P_N [N] P_N [10^{-4}N]

where

N	number of buckled shape
L_N [m]	length of the N-th buckled shape in [m]
L_{Tot} [mm]	total length (up to N-th buckled shape) in [mm]

$P_{N,SIN}$ [N]	total force (up to N-th buckled shape) with friction only (no reaction) in [N]
mode	description of the deformation of N-th buckled shape
flag	flag to be used to determine the development of the helical shape
P_N [N]	total force (up to N-th buckled shape) with reaction, if appropriate, in [N]
P_N [10^{-4}N]	total force (up to N-th buckled shape) with reaction, if appropriate, in [10^{-4}N]

4 Enter all N

Calculate L_1

$$L_1 = K_1^{1/3}\left[\frac{EI}{m_L \mu g}\right]^{1/3} \tag{J.3}$$

$$L_1 = 1.99\left[\frac{EI}{m_L \mu g}\right]^{1/3} \tag{J.4}$$

5 Calculate L_2

$$L_2 = K_2^{1/3} - K_1^{1/3}\left[\frac{EI}{m_L \mu g}\right]^{1/3} \tag{J.5}$$

$$L_2 = 1.84\left[\frac{EI}{m_L \mu g}\right]^{1/3} \tag{J.6}$$

6 Calculate L_N in sinusoidal buckling for N > 2

$$L_N = \pi\left(\frac{EI}{F_{N-1}}\right)^{1/2}\left\{1 - \frac{6}{\pi^2 F_{N-1}}\left[EI\left(m_L \mu g\right)^2\right]^{1/3}\right\}^{1/2} \tag{J.7}$$

Note that the field is different.

7 Calculate L_{Tot} [mm]

Adding L_N and multiplying by 1000.

8 Calculate $P_{N,SIN}$ [N]: only friction, no reaction forces

(as would appear in sinusoidal buckling)

$$P_N = P_{N-1} + m_L \mu g L_N \tag{J.8}$$

9 Mode: determination of mode of buckling

if $L_{Tot} \leq L_{CR}$ *then enter SIN otherwise enter HEL*

10 Flag: flag to be used to determine the development of the helical shape

if SIN then add 0 *otherwise add* 1

The flag determines the number of helical cycles; hence if flag =1 we are in the first cycle, if flag = 2 we are in the second cycle etc.

11 Calculation of pitch p in helical buckling (noting that $p_N = L_N$ when helical buckling is reached)

$$L_N = 2^{1.5} \pi \left(\frac{EI}{F_{N-1}} \right)^{1/2} \tag{J.9}$$

This only applies if the N-1 mode is HEL

12 Calculation of L_N

if mode = SIN then use sinusoidal otherwise use helical

13 Calculate P_N in helical buckling

$$P_N = P_{N-1} \left(1 + 2\pi^2 \mu \frac{D-d}{L_N} \right) \tag{J.10}$$

However, this only applies when we are in the fully developed helical cycle; in the first three cycles we assume that instead of $2\pi^2$ (or about 20) the multiplying constant is 2.5, 5 and 10 respectively.

This is achieved by multiplying $2\pi^2$ by

$$\frac{1}{2^{4-\min(flag,4)}} \tag{J.11}$$

If the flag = 1 then the multiplier is 1/8, if the flag = 2 then the multiplier is ¼, if the flag = 3 then the multiplier is ½ , and if the multiplier is ≥ 4 then the multiplier is 1.

Hence the overall equation for helical buckling is

$$P_N = P_{N-1}\left(1 + 2\pi^2 \frac{1}{2^{4-\min(flag,4)}} \mu \frac{D-d}{L_N}\right) \qquad \text{(J.12)}$$

14 General calculation of P_N [N]

if mode = SIN then use sinusoidal force otherwise use helical force

15 Avoiding numerical problems with the calculation of L_N

In order to avoid numerical problems

$$if\ L_{N-1} < 10^{-10}\ then\ L_N = 10^{-20} \qquad \text{(J.13)}$$

16 Avoiding numerical problems with the calculation of P_N [N]

In order to avoid numerical problems

$$if\ P_{N-1} > 10^{50}\ then\ P_N = 10^{50} \qquad \text{(J.14)}$$

17 The whole process continues

A copy of the above programme is given in the enclosed CD Rom as a file C.T. Model 10108.